

**PHYSICOCHEMICAL INTERACTIONS OF  
ENGINEERED NANOPARTICLES WITH  
MODEL CELL MEMBRANES**

by  
Xitong Liu

A dissertation submitted to Johns Hopkins University in conformity with the  
requirements for the degree of Doctor of Philosophy

Baltimore, Maryland  
June 2017

© 2017 Xitong Liu  
All Rights Reserved

## ABSTRACT

Due to the widespread application of engineered nanoparticles (ENPs) and their potential release into the environment, it is important to assess their potential impacts on human health. Recent studies have shown that both carbon-based and inorganic ENPs can induce cytotoxicity toward human cells. An improved understanding of how ENPs interact with biological membranes will help elucidate the mechanisms for their cytotoxicity. In this dissertation, the physicochemical interactions of both carbon-based and inorganic nanoparticles with model cell membranes were investigated.

The deposition of graphene oxide (GO) on supported lipid bilayers (SLBs) formed on silica surfaces was controlled by electrostatic interactions. Upon attachment of GO to supported lipid vesicles that were encapsulated with fluorescence dye, release of dye was detected, thus demonstrating that the vesicles were disrupted. The dye release was substantially reduced when the exposure of the vesicles to GO suspension was terminated, suggesting that the vesicles have a self-healing ability.

The adsorption of human serum albumin (HSA) on GO was investigated through a combination of batch adsorption experiments and quartz crystal microbalance with dissipation (QCM-D) measurements. An increase in ionic strength under neutral pH conditions resulted in higher adsorption densities as well as more compact HSA layers on GO. The attachment of GO to SLBs was reduced in the presence of protein coronas, and the degree of reduction was influenced by the conformation of the adsorbed protein layers on GO. In a separate study, phosphate ions were shown to adsorb appreciably on alumina and ceria nanoparticles and impart additional negative charge to the particles.

As a result, the attachment of these two nanoparticles to SLBs at neutral pH was considerably reduced in the presence of phosphate.

In the third part of the dissertation, the interactions forces between silver nanoparticles (AgNPs) and SLBs were measured using an atomic force microscope (AFM). The AFM tips were functionalized with AgNPs by sequentially exposing the tips to polydopamine and silver nitrate solutions. The AFM force measurements revealed that AgNPs experience predominantly repulsive forces when approaching SLBs. The presence of HSA resulted in an enhancement in the repulsive interactions between AgNPs and SLBs likely through steric repulsion.

**Advisor:** Kai Loon Chen

**Committee members:** Edward Bouwer, Howard Fairbrother, and Patricia McGuiggan

## ACKNOWLEDGEMENTS

First and foremost, I would like to express my deepest gratitude to my advisor Dr. Kai Loon Chen. Kai Loon has taught me in many aspects, from designing a set of experiments to giving a presentation at a professional conference. Each time I write a draft of a paper, Kai Loon always provides insightful comments which lead me to think deeper into the science behind the experimental results. Kai Loon also maintains high standards for scientific rigor and originality. I greatly appreciate the time and efforts Kai Loon has invested in my development as a researcher.

I would like to thank my committee members, Drs. Edward Bouwer, Howard Fairbrother, and Patricia McGuiggan, for reviewing my dissertation and for their advice and guidance throughout my Ph.D. studies. Dr. Bouwer is not only one of my mentors in science but also a supportive friend of mine who shares common interests in photography and classical music with me. Dr. Fairbrother always asks critical questions in my research presentations from which I benefit enormously. Dr. McGuiggan trained me on the calibration of atomic force microscope probes and patiently helped me when I ran into issues on the AFM.

Sincere thanks, as well, to other professors in our department and other departments at JHU. Dr. Alan Stone always provides insightful feedback when I have questions on aquatic chemistry and beyond. I still vividly remember the question Alan asked me when I walked into his office three years ago: “what is your expertise? What do you want your current research to be remembered?” I am also grateful to Dr. Lynn Roberts for granting me the opportunity to serve as a teaching assistant in one of her lab

classes from which I gained valuable teaching skills. I would like to thank Dr. Bill Ball for providing insightful comments on my research and offering advice on my career development. I am thankful to Dr. Sarah Preheim for encouraging me to think the “big picture” of my research during my DQE exam. Dr. Joelle Frechette taught me fundamental principles of colloidal chemistry and physics and showed me the mighty role of rigorous derivations in science. Dr. Kenneth Livi and Bryan Crawford kindly helped me with scanning electron microscopy imaging. Dr. Kalina Hristova graciously provided me with access to the fluorescence spectrophotometer in her lab. Dr. Kellogg Schwab kindly served as my reference when I applied for the E<sup>2</sup>SHI fellowship. Michael McCaffery helped me greatly with TEM imaging. I would also like to thank John Thornton from Bruker Corporation for training me on the use of atomic force microscope.

I would like to thank current and previous staff members in our department: Huan Luong, Adena Rojas, Michael Lester, Jessica Elroy, Sean Carr, Denise Nowlin, Keith Ritchie, and Vicky Moreira, for taking care of the logistics so that I can focus on my research. Special thanks to Huan Luong who not only helped me enormously with my experiments but also provided caring suggestions on my career path.

I would like to thank my colleagues in Chen’s lab. Peng Yi patiently trained me on instrumentations and has been a confidant when I come across difficulties in my personal life. Chenxu Yan devoted tremendous efforts in performing batch adsorption experiments which are included in this dissertation. Meng Hu, Margaret Fleming, Li Tang, Khanh An Huynh, Xin Liu, Qiaoying Wang, Yiping Feng, Peixian Yang, Mathieu Larronde-Larretche, and Davide Cappelluti all helped me in various aspects in my research.

I am extremely grateful to be a part of the JHU community. Xiaomeng Xia kindly offered me rides to grocery stores when I first arrived in Baltimore. I am thankful to Jessica Lawson, David Goodwin, Mike Rose, Stephanie Lau, Steven Chow, Dano Wilusz, Hannah Gray, Shane Putnam, and Ronald Lankone for having memorable conversations with me and for providing feedback to my presentations. Dr. Beibei Liu helped me greatly when I took the driving tests. Dr. Meng Rowland and her husband Garland Rowland kindly picked me up when I first arrived in U.S. and helped me settle down. I would like to thank my friends at JHU: Fengwei Hung, Qian Zhang, Zhifeng Yan, Jin Yang, Liang Chen, Wanshu Nie, Qingyu Xu, Xiao Yu, Liang Wu, Weichen Liao, Tianqi Liu, Pengcheng Ding, Jiawang Zhou, Nate Dunkin, Sarah Kim, Ning Zhang, Chenyang Wang, Jiwei Chen, Pengwen Xiong, Congyuan Yang, and Li Song for making my Ph.D. study a fun journey. I would also like to express my gratitude to my friends from China: Junfeng Gao, Liping Ma, Jie Liu, Yan Li, and Yanzhen Li.

Throughout my Ph.D studies, my research has been supported by National Science Foundation and Semiconductor Research Corporation. I would like to thank Mr. Gary Anderson for kindly granting me a fellowship during my second year at JHU.

Finally, I owe the deepest gratitude to my family. My father Gengshen Liu has always been a role model for me. His optimism, courage, and perseverance have been motivating me in my everyday life. My mother Xiuling Li has always been providing unconditional love and encouraging me to pursue a career of my interest. I appreciate my sister Jihua Liu for accompanying and helping my parents on a daily basis. I am deeply grateful to Xiaoxue Hou for her love and support and for encouraging me to explore more beauty of life.

# Table of Contents

<b>Chapter 1. Introduction.....</b>	<b>1</b>
<b>1.1 Engineered Nanoparticles.....</b>	<b>2</b>
<b>1.2 Cytotoxicity of Engineered Nanoparticles .....</b>	<b>2</b>
<b>1.3 Model (Artificial) Cell Membranes .....</b>	<b>4</b>
<b>1.4 Interactions between Nanoparticles and Model Cell Membranes .....</b>	<b>5</b>
<b>1.5 Biological Transformation of Nanoparticles.....</b>	<b>7</b>
<b>1.6 Objectives and Scope of Dissertation .....</b>	<b>9</b>
<b>1.7 Dissertation Organization.....</b>	<b>10</b>
<b>1.8 References .....</b>	<b>11</b>
<b>Chapter 2. Interactions of Graphene Oxide with Model Cell Membranes:</b>	
<b>Probing Nanoparticle Attachment and Lipid Bilayer Disruption.....</b>	<b>16</b>
<b>2.1 Introduction.....</b>	<b>17</b>
<b>2.2 Materials and Methods.....</b>	<b>19</b>
2.2.1 Preparation and Characterization of GO Suspensions.....	19
2.2.2 Solution Chemistry .....	20
2.2.3 Preparation of Vesicle Stock Suspensions.....	20
2.2.4 Preparation of Vesicles Encapsulated with Fluorescent Dye .....	21
2.2.5 Electrophoretic Mobility and Dynamic Light Scattering Measurements .....	21
2.2.6 Quartz Crystal Microbalance with Dissipation Monitoring .....	22
2.2.7 Detection of Dye Leakage from Supported Vesicles.....	24
<b>2.3 Results and Discussion.....</b>	<b>25</b>
2.3.1 Electrokinetic properties of GO.....	25

2.3.2	Deposition Kinetics of GO on SLBs .....	26
2.3.3	Reversibility of GO Deposition on DOPC SLBs .....	34
2.3.4	No Significant Rupture of Supported Vesicles when Exposed to GO .....	36
2.3.5	Release of Fluorescent Dye from Supported DOPC Vesicles .....	38
<b>2.4</b>	<b>Conclusions .....</b>	<b>47</b>
<b>2.5</b>	<b>References .....</b>	<b>48</b>

### **Chapter 3. Adsorption of Human Serum Albumin on Graphene Oxide:**

#### **Implications for Protein Corona Conformation and Nanoparticle-Cell Membrane Interactions 54**

<b>3.1</b>	<b>Introduction .....</b>	<b>55</b>
<b>3.2</b>	<b>Materials and Methods .....</b>	<b>57</b>
3.2.1	Preparation and Characterization of GO Suspensions .....	57
3.2.2	Solution Chemistry .....	58
3.2.3	Dynamic Light Scattering (DLS) .....	58
3.2.4	Atomic Force Microscopy (AFM) Imaging of GO Nanosheets .....	59
3.2.5	Electrophoretic mobility (EPM) measurements .....	59
3.2.6	Batch Adsorption Experiments .....	59
3.2.7	Preparation of GO-coated QCM-D Sensors .....	61
3.2.8	Adsorption of HSA on GO-coated Sensors .....	64
3.2.9	Deposition of GO and HSA-modified GO on DOPC SLBs .....	65
<b>3.3</b>	<b>Results and Discussion .....</b>	<b>65</b>
3.3.1	Characterization of GO .....	65
3.3.2	Influence of Ionic Strength on HSA Adsorption on GO .....	67
3.3.3	Influence of Calcium on HSA Adsorption on GO .....	70
3.3.4	Influence of pH on HSA Adsorption on GO .....	71



3.3.5	Evolution of Protein Layer Conformations Over Time during HSA Adsorption.....	74
3.3.6	HSA adsorption Reduced GO attachment to SLBs at pH 7 .....	77
3.3.7	Implications .....	79
<b>3.4</b>	<b>References .....</b>	<b>80</b>
<b>Chapter 4. Aggregation and Interactions of Chemical Mechanical Planarization</b>		
<b>Nanoparticles with Model Biological Membranes: Role of Phosphate Adsorption . 85</b>		
<b>4.1</b>	<b>Introduction .....</b>	<b>86</b>
<b>4.2</b>	<b>Materials and Methods .....</b>	<b>88</b>
4.2.1	CMP NP Suspensions .....	88
4.2.2	Solution Chemistry .....	89
4.2.3	Electrophoretic Mobility Measurements .....	89
4.2.4	Phosphate Adsorption by CMP NPs .....	90
4.2.5	Dynamic Light Scattering .....	92
4.2.6	Preparation of Vesicle Stock Suspensions.....	94
4.2.7	Quartz Crystal Microbalance with Dissipation Monitoring .....	95
4.2.8	Detection of Dye Leakage from Supported Vesicles.....	96
<b>4.3</b>	<b>Results and Discussion .....</b>	<b>97</b>
4.3.1	Electrokinetic Properties of CMP NPs .....	97
4.3.2	Stability of <i>c</i> -SiO <sub>2</sub> and <i>f</i> -SiO <sub>2</sub> NPs at pH 7.4.....	100
4.3.3	Phosphate Adsorption Enhanced the Stability of CeO <sub>2</sub> and Al <sub>2</sub> O <sub>3</sub> NPs.....	104
4.3.4	Deposition of CMP NPs on DOPC SLBs in the Presence of Phosphate .....	106
4.3.5	Comparing Deposition Kinetics of CMP NPs on DOPC SLBs in the Presence and Absence of Phosphate .....	108
4.3.6	No Disruption of Vesicles by CMP NPs Detected .....	110
<b>4.4</b>	<b>Conclusions .....</b>	<b>114</b>

4.5	References .....	115
<b>Chapter 5. Silver Nanoparticles Formed <i>In Situ</i> on AFM Tips for Force</b>		
<b>Measurements with Model Cell Membranes: Influence of Protein Coronas .....</b>		<b>120</b>
5.1	Introduction .....	121
5.2	Materials and Methods .....	122
5.2.1	Preparation and Characterization of AgNP-Modified AFM Probes.....	122
5.2.2	Preparation of Lipid Vesicles .....	123
5.2.3	Formation and AFM Imaging of Lipid Bilayers on Mica .....	123
5.2.4	AFM Force Measurements .....	124
5.3	Results and Discussion .....	125
5.3.1	Formation of AgNPs on AFM Tips .....	125
5.3.2	Lipid Bilayers Formed on Mica for AFM Force Measurements .....	131
5.3.3	Presence of HSA Enhanced the Repulsion between AgNPs and Lipid Bilayers ...	133
5.3.4	Protein Coronas Raised the Forces for AgNPs to Penetrate Lipid Bilayers .....	136
5.3.5	Implications .....	137
5.4	References .....	137
<b>Chapter 6. Conclusions, Engineering Significance, and Future Work .....</b>		
6.1	Conclusions .....	142
6.2	Key Contributions and Engineering Significance .....	145
6.3	Future Work.....	149

## List of Tables

### Chapter 3

Table 3.1. Fitted parameters of Freundlich isotherm for HSA adsorption on GO..... 68

### Chapter 4

Table 4.1. Concentrations of CMP NPs used in electrophoretic mobility measurements 90

Table 4.2. Concentrations of CMP NPs used in dynamic light scattering measurements.93

Table 4.3. Concentrations of CMP NPs used in quartz crystal microbalance experiments.  
..... 96

## List of Figures

### Chapter 2

- Figure 2.1. Effect of GO on the fluorescence intensity of 1  $\mu\text{M}$  CF dye dissolved in HEPES buffer. The concentration of GO was 2.6 mg/L TOC..... 25
- Figure 2.2 EPMs of GO as functions of NaCl and  $\text{CaCl}_2$  concentrations at pH 7.2. Error bars represent standard deviations. The lines are meant to guide the eye. .... 26
- Figure 2.3. Representative frequency (blue) and dissipation (red) shifts during the formation of a DOPC SLB on a silica crystal and the deposition of GO on the SLB. In Stage A, stable baselines were obtained by rinsing the silica crystal with Buffer A. In Stage B, DOPC vesicles were deposited on the silica surface and they ruptured to form a SLB. In Stage C, the system was rinsed with Buffer A to remove unadsorbed vesicles. In Stage D, stable baselines were obtained by rinsing the SLB with a 0.6 mM  $\text{CaCl}_2$  and pH 7.2 solution. In Stage E, GO was deposited on the SLB in the same solution chemistry as used in Stage D..... 27
- Figure 2.4. Deposition rates of GO on DOPC SLBs as functions of (a) NaCl and (b)  $\text{CaCl}_2$  concentrations at pH 7.2. Attachment efficiencies of GO on DOPC SLBs as functions of (c) NaCl and (d)  $\text{CaCl}_2$  concentrations at pH 7.2. Error bars represent standard deviations. The lines are meant to guide the eye..... 29
- Figure 2.5. (a) Aggregation of GO in the presence of NaCl at pH 7.2. (b) Aggregation of GO in the presence of  $\text{CaCl}_2$  at pH 7.2. The concentration of GO was 2.6 mg/L TOC..... 30
- Figure 2.6. Deposition rates of GO on PLL-coated surfaces as functions of (a) NaCl and (b)  $\text{CaCl}_2$  concentrations at pH 7.2. Error bars represent standard deviations. The lines are meant to guide the eye..... 31
- Figure 2.7. (a) EPMs of DOPC–DOEPC vesicles as a function of NaCl concentration at pH 7.2. (b) Attachment efficiencies of GO on positively charged DOPC–DOEPC SLBs as a function of NaCl concentration at pH 7.2. Error bars represent standard deviations. The lines are meant to guide the eye. .... 33

Figure 2.8. Frequency shifts during the deposition of GO on SLBs at 1.1 mM CaCl <sub>2</sub> and rinsing of deposited GO with a 1.1 mM CaCl <sub>2</sub> solution followed by DI water. The pH is maintained at 7.2 for the entire experiment.....	35
Figure 2.9. Frequency and dissipation shifts during the formation of a DOPC SVL and the deposition of GO on the SVL at 0.6 mM CaCl <sub>2</sub> and pH 7.2.....	37
Figure 2.10. Frequency (blue) and dissipation (red) shifts during the formation of a DOPC–DOEPC SVL and the deposition of GO on the SVL at 150 mM NaCl and pH 7.2. The red arrows indicate the times at which two GO suspensions were successively prepared and introduced to the QCM-D chambers to allow for the deposition of GO on the SVL. ....	39
Figure 2.11. Schematic of dye leakage detection coupled with QCM-D. Note that GO and vesicles are not drawn in scale. ....	40
Figure 2.12. (a) Frequency and dissipation shifts when supported DOPC vesicles were exposed to GO suspension in 150 mM NaCl (shaded in red), 150 mM NaCl solution (shaded in blue), and 32 mM Triton X-100. The solid and dash lines show the frequency and dissipation shifts, respectively. (b) Release of CF dye from supported vesicles upon exposure to GO suspension (in 150 mM NaCl), 150 mM NaCl solution, and 32 mM Triton X-100. The red and blue lines show the release of dye in the GO deposition and control experiments, respectively. (c) Close-up of the release of dye in the GO deposition and rinsing stages, both at 150 mM NaCl. Error bars represent standard deviations. ....	42
Figure 2.13. (a) Frequency and dissipation shifts when supported DOPC vesicles were exposed to GO suspension in 0.6 mM CaCl <sub>2</sub> (shaded in red), 0.6 mM CaCl <sub>2</sub> solution (shaded in blue), and 32 mM Triton X-100. The solid and dash lines show the frequency and dissipation shifts, respectively. (b) Release of CF dye from supported vesicles when the vesicles were exposed to GO suspension (in 0.6 mM CaCl <sub>2</sub> ), 0.6 mM CaCl <sub>2</sub> solution, and 32 mM Triton X-100. The red and blue lines show the dye release profiles in the GO deposition and control experiments, respectively. Error bars represent standard deviations. ....	45
Figure 2.14. (a) Frequency and dissipation shifts when supported DOPC vesicles were exposed to GO suspension in 1 mM NaCl (shaded in red), 1 mM NaCl solution (shaded in blue), and 32 mM Triton X-100. The solid and dash lines show the frequency and dissipation shifts, respectively. (b) Release of CF dye from supported vesicles upon exposure to GO suspension (in 1 mM NaCl), 1 mM NaCl solution,	

and 32 mM Triton X-100. The red and blue lines show the release of dye in the GO deposition and control experiments, respectively. Error bars represent standard deviations. .... 46

### Chapter 3

Figure 3.1. (a) Representative TEM of gold nanoparticles (AuNPs). The scale bar represents 100 nm. (b) Size distribution of 128 AuNPs adsorbed on a TEM grid. Longest dimensions were measured for slightly elongated nanoparticles. Each bar represents a diameter range of 0.5 nm. .... 62

Figure 3.2. (a) Coating of a QCM-D sensor with a GO layer and the deposition of AuNPs on the GO layer. (b) Coating of a QCM-D sensor with PLL and the deposition of AuNPs on the PLL layer. Duplicate experiments were performed and similar results were obtained. .... 63

Figure 3.3. (a) AFM images of GO. (b) AFM Height profiles of GO. The positions of the profiles are marked as white lines in (a). .... 66

Figure 3.4. (a) EPMs of GO at 150 mM NaCl under different pH conditions. (b) EPMs of GO at pH 7.0 with an ionic strength of 1 mM in the absence and presence of calcium ions. Error bars represent standard deviations. .... 66

Figure 3.5. (a) Adsorption isotherms of HSA on GO at pH 7.0. Dashed lines represent Freundlich fitting. (b) Wet mass of HSA adsorbed on a GO layer estimated using Sauerbrey model during the exposure of the GO layer to 125 mg/L HSA at pH 7.0 followed by rinsing with background electrolytes. Vertical lines indicate the time points at which solutions were switched from protein-free solutions (S) to protein solutions (S+HSA) and finally back to protein-free solutions (S). (c) Overall  $\Delta D/\Delta f$  values calculated from data in (b). The cartoon illustrates the proposed conformation of HSA layers on GO under different ionic strengths. .... 67

Figure 3.6. (a) Adsorption isotherms of HSA on GO at pH 7.0 in the absence and presence of calcium ions. Dashed lines represent Freundlich fitting. (b) Wet mass of HSA adsorbed on a GO layer estimated using Sauerbrey model during the exposure of the GO layer to 125 mg/L HSA at pH 7.0 followed by rinsing with background electrolytes. Vertical lines indicate the time points at which solutions were switched from protein-free solutions (S) to protein solutions (S+HSA) and finally back to protein-free solutions (S). (c) Overall  $\Delta D/\Delta f$  values calculated from data in (b). The

cartoon illustrates the proposed conformation of HSA layers on GO in absence and presence of calcium..... 71

Figure 3.7. (a) Adsorption isotherms of HSA on GO at 150 mM NaCl under varying pH conditions. Dashed lines represent Freundlich fitting. (b) Wet mass of HSA adsorbed on a GO layer estimated using Sauerbrey model during the exposure of the GO layer to 125 mg/L HSA at 150 mM NaCl followed by rinsing with background electrolytes. Vertical lines indicate the time points at which solutions were switched from protein-free solutions (S) to protein solutions (S+HSA) and finally back to protein-free solutions (S). (c) Overall  $\Delta D/\Delta f$  values calculated from data in (b). The cartoon illustrates the proposed conformation of HSA layers on GO under different pH conditions..... 72

Figure 3.8. Dissipation shift versus frequency shift plots using QCM-D data at pH 7.0 as a function of (a) ionic strength (b) calcium presence, and (c) at 150 mM NaCl as a function of pH. Inset in (c) shows the linear fitting at pH 4.7 and 7.0. The  $\Delta D$  and  $\Delta f$  data between the onset of HSA adsorption and the point where  $\Delta f$  reaches maximum magnitude are used in all  $D/f$  plots. Vertical dashed lines represent the break points of the two-stage adsorption processes. Duplicate experiments were conducted and similar results were obtained. .... 74

Figure 3.9. Frequency shifts during the adsorption of 125 mg/L HSA on silica (a) and GO (b) at 150 mM NaCl under varying pH conditions..... 76

Figure 3.10. Effect of HSA adsorption on the deposition of GO on DOPC supported lipid bilayers at pH 7.0 under different ionic strengths. The cartoon illustrates the interaction of protein-coated GO with lipid bilayers..... 77

Figure 3.11. (a) Average hydrodynamic diameter of GO and HSA-modified GO during the initial 20 min of aggregation at 30 and 150 mM NaCl, pH 7.0. (b) Electrophoretic mobilities of GO and HSA-modified GO at 30 and 150 mM NaCl, pH 7.0..... 78

## Chapter 4

Figure 4.1. (a) EPMs of CMP NPs over a wide range of NaCl concentrations at pH 7.4 in phosphate buffer. (b) EPMs of CMP NPs at 1 and 100 mM NaCl and pH 7.4 in phosphate and bicarbonate buffer. The data in phosphate buffer was reproduced from Figure 1a for comparison. (c) Phosphate adsorption by CMP NPs within a time duration of 10 min. The adsorption experiments were conducted at an initial

phosphate concentration of 100 $\mu$ M, 1 g/L NPs, 1 mM NaCl, and pH 7.4. Error bars represent standard deviations.....	98
Figure 4.2. Aggregation profiles of four CMP NPs at 150 mM NaCl and pH 7.4 in (a) phosphate and (b) bicarbonate buffer. ....	101
Figure 4.3. Aggregation profiles of (a) <i>f</i> -SiO <sub>2</sub> NPs at 150 mM NaCl at pH 7.4 (in phosphate and bicarbonate buffer) and pH 2.0 (pH adjusted with 1 M HCl), (b) <i>c</i> -SiO <sub>2</sub> NPs at 150 mM NaCl at pH 7.4 (in phosphate and bicarbonate buffer) and pH 2.0 (pH adjusted with 1 M HCl), and (c) <i>c</i> -SiO <sub>2</sub> NPs at pH 12 (pH adjusted with 1 M NaOH) at varying NaCl concentrations.....	103
Figure 4.4. Aggregation attachment efficiencies of (a) CeO <sub>2</sub> and (b) Al <sub>2</sub> O <sub>3</sub> NPs as a function of NaCl concentration at pH 7.4 in phosphate and bicarbonate buffer. The dashed lines are extrapolated from the favorable and unfavorable aggregation regimes, and their intersections yield the CCCs. ....	105
Figure 4.5. Deposition rates of (a) <i>c</i> -SiO <sub>2</sub> , (b) <i>f</i> -SiO <sub>2</sub> , (c) CeO <sub>2</sub> , and (d) Al <sub>2</sub> O <sub>3</sub> NPs on DOPC SLBs in phosphate buffer at pH 7.4. Error bars represent standard deviations and the lines are meant to guide the eye. Asterisks (*) indicates that no frequency shift was detected.....	106
Figure 4.6. Deposition rates of (a) <i>c</i> -SiO <sub>2</sub> , (b) <i>f</i> -SiO <sub>2</sub> , (c) CeO <sub>2</sub> , and (d) Al <sub>2</sub> O <sub>3</sub> NPs on PLL-modified surfaces in phosphate buffer at pH 7.4. Error bars represent standard deviations and the lines are meant to guide the eye.....	107
Figure 4.7. Deposition attachment efficiencies of (a) <i>c</i> -SiO <sub>2</sub> , (b) <i>f</i> -SiO <sub>2</sub> , (c) CeO <sub>2</sub> , and (d) Al <sub>2</sub> O <sub>3</sub> NPs on DOPC SLBs at pH 7.4 in phosphate buffer. Error bars represent standard deviations. The lines are meant to guide the eye. Asterisks (*) indicate that no frequency shift was detected on SLBs.....	108
Figure 4.8. Deposition attachment efficiencies of (a) <i>c</i> -SiO <sub>2</sub> , (b) <i>f</i> -SiO <sub>2</sub> , (c) CeO <sub>2</sub> , and (d) Al <sub>2</sub> O <sub>3</sub> NPs on DOPC SLBs at pH 7.4 in phosphate and bicarbonate buffer. Error bars represent standard deviations. The data in phosphate buffer was reproduced from Figure 4.7 for comparison. Asterisks (*) indicate that the attachment efficiencies were 0 (i.e., no frequency shift was detected on SLBs). ....	109



Figure 4.9. (a) Frequency and dissipation shifts during the formation of a SVL (26–57 min), the deposition of *f*-SiO<sub>2</sub> NPs on the SVL at 150 mM NaCl and pH 7.4 (213–257 min), and the rupture of the vesicles when they were exposed to 32 mM Triton X-100 (277–301 min). (b) Frequency and dissipation shifts when supported vesicles were exposed to *f*-SiO<sub>2</sub> NPs (in 150 mM NaCl), 150 mM NaCl, and 32 mM Triton X-100. (c) Release of CF dye from supported vesicles upon exposure to *f*-SiO<sub>2</sub> NPs (in 150 mM NaCl), 150 mM NaCl, and 32 mM Triton X-100. Insert: close-up of the release of dye in the *f*-SiO<sub>2</sub> NP deposition stage. .... 111

Figure 4.10. (a) Frequency and dissipation shifts when supported vesicles were exposed to *c*-SiO<sub>2</sub> NP suspension prepared at 150 mM NaCl (191–234 min), 150 mM NaCl solution (234–256 min), and 32 mM Triton X-100 solution (256–280 min). The solid and dash lines show the frequency and dissipation shifts, respectively. (b) Release of CF dye from supported vesicles when the vesicles were exposed to *c*-SiO<sub>2</sub> NP suspension prepared at 150 mM NaCl, 150 mM NaCl solution, and 32 mM Triton X-100 solution. The red and blue lines show the dye release profiles in the NP deposition and control experiments, respectively. Error bars represent standard deviations. .... 113

## Chapter 5

Figure 5.1. (a) Schematic of the modification of AFM probes with AgNPs on the apex. (b) Secondary electron image of the AgNP-modified tip. (c) Backscattered electron image of the same AgNP-modified tip showing the contrast in chemical composition on the tip. .... 125

Figure 5.2. Backscattered electron imaging of (a) Ag-PDA (b) Si and (c) PDA tips..... 126

Figure 5.3. Backscattered electron imaging of an Ag-PDA tip (a) and the corresponding EDS analysis at a bright spot on the tip (b). .... 127

Figure 5.4. Backscattered electron imaging of a PDA tip (a) and the corresponding EDS analysis in a selected area on the tip (b). .... 128

Figure 5.5. SEM images of three different Ag-PDA tips. The left and right panels show the secondary and backscattered electron imaging, respectively..... 129

Figure 5.6. (a) Representative force profiles during retraction of PDA and AgNP tips from mica at 1 mM NaCl. (b) Work of adhesion for PDA and AgNP tips during

retraction from mica. Positive and negative values indicate attractive and repulsive interactions, respectively. Error bars represent standard deviations ( $n = 30$ ). Asterisks (\*) indicate significant difference ( $p < 0.01$ ) between PDA and AgNP tips. .... 130

Figure 5.7. (a) Representative force profiles during retraction of PDA and AgNP tips from DOPC SLBs at 1 mM NaCl. (b) Work of adhesion for PDA and three different AgNP tips during retraction from SLBs. Positive and negative values indicate attractive and repulsive interactions, respectively. Error bars represent standard deviations ( $n = 30$ ). Asterisks (\*) indicate significant difference ( $p < 0.01$ ) between PDA and AgNP tips. .... 131

Figure 5.8. (a) AFM image of a mica surface covered with a DOPC lipid bilayer. (b) Height profiles of the holes within the bilayer. (c) Representative force curves during the approaching of an AgNP tip toward an SLB and the retraction of the tip from the SLB. Force measurements were conducted at 1 mM NaCl. .... 132

Figure 5.9. Representative approach force curves between AgNP tips and DOPC SLBs at (a) 1 mM NaCl and (b) 150 mM NaCl. The  $D$  in x-axis represents the distance between the tips and the surface of the lipid bilayers. Inserts show fitted decay lengths at (b) 1 mM NaCl (d) 150 mM NaCl. Error bars represent standard deviations,  $n = 30$ . Asterisks (\*) indicate significant difference ( $p < 0.01$ ) between fitted decay lengths in absence and presence of HSA. .... 133

Figure 5.10. Semi-log plots of representative approach force curves between AgNP tips and DOPC SLBs in absence and presence of HSA at (a) 1 mM NaCl (b) 150 mM NaCl.  $D$  represents the separation between the tips and the lipid bilayer surface. 134

Figure 5.11. (A) Representative approach force curves between an Ag-NP tip and an SLB at 1 mM NaCl. The separation represents the distance between the tip and the mica substrate. (b) Forces required for AgNP tips to penetrate DOPC SLBs in absence and presence of HSA. Error bars represent standard deviations ( $n = 30$ ). Asterisks (\*) indicate significant difference ( $p < 0.01$ ) between penetration forces in absence and presence of HSA measured using the same tip. .... 136

## List of Abbreviations

AFM	Atomic Force Microscopy
AgNPs	Silver Nanoparticles
CF	5(6)-Carboxyfluorescein
CMP	Chemical Mechanical Planarization
CNTs	Carbon Nanotubes
DLS	Dynamic Light Scattering
DOPC	1,2-dioleoyl- <i>sn</i> -glycero-3-phosphocholine
DOEPC	1,2-dioleoyl- <i>sn</i> -glycero-3-ethylphosphocholine
ENPs	Engineered Nanoparticles
GO	Graphene Oxide
HEPES	<i>N</i> -(2-hydroxyethyl)-piperazine- <i>N'</i> -(2-ethanesulfonic acid)
HSA	Human Serum Albumin
IEP	Isoelectric Point
PDA	Polydopamine
PLL	Poly-L-lysine
QCM-D	Quartz Crystal Microbalance with Dissipation Monitoring
SEM	Scanning Electron Microscopy
SLBs	Supported Lipid Bilayers
SVLs	Supported Vesicular Layers
TEM	Transmission Electron Microscopy

# **Chapter 1. Introduction**

## **1.1 Engineered Nanoparticles**

Engineered nanoparticles (ENPs) represent a class of materials with at least one dimension of 100 nm or less.<sup>1</sup> ENPs, with unique physicochemical properties stemming from their nanoscale size, have offered a myriad of exciting opportunities in diverse fields. ENPs can be classified into carbon-based (e.g., carbon nanotubes and graphene) and inorganic (e.g., metal and metal oxide) nanoparticles.<sup>2</sup>

Graphene oxide (GO) is a two-dimensional carbonaceous nanomaterial which contains oxygen functionalities at the edges and on the basal planes.<sup>3</sup> GO holds a great promise in biological applications including drug delivery, cellular imaging, and cancer detection.<sup>4-6</sup> As a potent antimicrobial agent, silver nanoparticles (AgNPs) are being incorporated in consumer products, including socks, bandages, and food containers.<sup>7</sup> The antimicrobial activities of AgNPs have also been exploited in the fabrication of anti-fouling water filtration membranes.<sup>8</sup> In the semiconductor industry, large quantities of inorganic nanoparticles (e.g., silica, ceria, and alumina) are used in the chemical mechanical planarization (CMP) process which is a key step in the production of electronic devices. These three types of nanoparticles (GO, AgNPs, and CMP nanoparticles), representing both carbon-based and inorganic nanoparticles, are the focus of this study.

## **1.2 Cytotoxicity of Engineered Nanoparticles**

With the development of ENP-enabled technologies and products, the environmental and health risks associated with the ENPs are of major concern. The release of ENPs to the environment can occur during the production, application, and disposal steps of the ENP-containing products.<sup>9</sup> These release nanoparticles may cause harm to microorganisms and

higher organisms in aquatic environments.<sup>10</sup> Given the potential risk of human exposure to nanoparticles via dermal, ingestion, and inhalation pathways,<sup>11</sup> it is imperative to improve our understanding of the mechanisms for the adverse effects of ENPs to humans health.

Recent studies have provided increasing evidence that a wide range of ENPs exhibit cytotoxicity toward human and bacterial cells. While the pathways by which ENPs cause cytotoxicity are still under investigation, a plethora of studies has shown that the damage of cell membranes by ENPs can take place during nanoparticle-cell interactions. It has been demonstrated that GO nanosheets exhibit hemolytic activity to human red blood cells, thus giving rise to health risks when these nanomaterials are applied in drug delivery applications.<sup>12</sup> AgNPs exhibit strong antimicrobial activity toward both bacteria and viruses.<sup>8, 13, 14</sup> AgNPs have been reported to accumulate in the bacterial membrane and result in the formation of “pits” on the membrane.<sup>15</sup> Silica nanoparticles have also been shown to cause membrane damage to human red blood cells.<sup>16</sup> The damage to cell membranes can take place through the direct physical interactions between nanoparticles and membranes. GO can induce the perturbation of bacterial cell membranes through the penetration of membranes by the sharp corners and edges of the graphene oxide nanosheets.<sup>17, 18</sup> The disruption of human red blood cells by silica nanoparticles has been ascribed to the wrapping of the nanoparticles by cell membranes as a result of favorable binding energies.<sup>19</sup>

In addition to causing physical damage to biological membranes, ENPs can exert oxidative stress to bacterial and human cells.<sup>20, 21</sup> Nanoparticles may induce oxidative stress to cells via nanoparticle-mediated electron transfer between cell membrane and the extracellular environment, thus resulting in the oxidation of cellular components.<sup>22, 23</sup> Under these scenarios, the attachment of nanoparticles to cell membranes is expected to be a crucial

step preceding the various oxidative pathways. Therefore, a better understanding of the nanoparticle-cell membrane interactions will help unravel the mechanisms for the cytotoxicity of nanoparticles.

### **1.3 Model (Artificial) Cell Membranes**

Cell membranes separate the intracellular environment from the extracellular surroundings and also provide an interface where numerous cellular functions (e.g., signaling, membrane vesicle trafficking, and endocytosis) take place. The skeletons of cell membranes are lipid bilayers, which serve as barriers against the passage of water-soluble species.<sup>24</sup> Lipid membranes also contain various peripheral and transmembrane proteins,<sup>25</sup> which perform a variety of biological functions<sup>26</sup> Mammalian cell membranes contain varying amounts of cholesterol, which has a unique function of regulating the fluidity and permeability of lipid membranes.<sup>27, 28</sup> In addition, carbohydrates are commonly found on the membranes of bacterial and human cells.<sup>29</sup>

Given this complexity of cell membranes, artificial membranes with known compositions and controlled physicochemical properties can provide insights into the fundamental aspects of nanoparticle-membrane interactions.<sup>29</sup> Commonly used models for cell membranes include solid-supported lipid bilayers, free-suspending lipid bilayers, supported vesicular layers, and free-suspending vesicles.<sup>29, 30</sup> Importantly, these model membranes are amenable to a spectrum of microscopic and spectroscopic techniques that are widely used in the surface science community.<sup>31, 32</sup> The focus of this study is the use of model membranes to gain fundamental insights into the nonspecific interactions between nanoparticles and cell membranes.

Solid-supported lipid bilayers (SLBs) can be facilely prepared through the spreading of vesicles on a solid surface.<sup>33</sup> SLBs are a highly versatile tool for investigating nanoparticle-membrane interactions because the composition of the lipid bilayers can be systematically varied.<sup>34</sup> SLBs can be employed to investigate the binding of nanoparticles to lipid membranes. Lipid vesicles, either freestanding or immobilized on a solid substrate, are another important model for cell membranes. Lipid vesicles can provide information on the propensity of nanoparticles to disrupt lipid membranes. Fluorescent dyes can be incorporated into vesicles, and the leakage of dye from inside of the vesicles serves as an indication of the local perturbation or formation of pores on the lipid membrane.<sup>35</sup>

#### **1.4 Interactions between Nanoparticles and Model Cell Membranes**

The use of SLBs to probe the attachment of nanoparticles to lipid membranes has been the subject of a number of studies.<sup>36-38</sup> The propensities for a variety of nanoparticles to attach to SLBs have been investigated as a function of solution chemistry, and the dominating interaction forces between nanoparticles and lipid bilayers have been proposed. It has been demonstrated that the attachment behaviors of quantum dots, carbon nanotubes, and AgNPs to SLBs were controlled by electrostatic interactions.<sup>36-38</sup> When the electrostatic interactions between nanoparticles and lipid bilayers are repulsive, van der Waals attraction serves as an important driving force for the attachment of nanoparticles to lipid bilayers.<sup>37, 38</sup> Since the head groups of lipid bilayers are highly hydrated,<sup>39</sup> repulsive hydration forces can lower the propensity for nanoparticles to bind to lipid bilayers.<sup>37</sup>

Despite recent progress on the attachment of nanoparticles to lipid bilayers, direct measurements of interaction forces between nanoparticles and lipid bilayers have received



much less attention. Measuring nanoparticle-membrane interaction forces is central to elucidating how nanoparticles would interact with cell membranes once they come into contact. Attractive nanoparticle-membrane interactions are expected to facilitate the adhesion of nanoparticles to cell membranes. When the nanoparticle-membrane interactions are predominantly repulsive, physical interactions are not likely to play a key role in determining the toxicity effect of nanoparticles.<sup>40</sup> Atomic force microscope (AFM) is a powerful tool which allows direct force measurements between an AFM tip and a surface. By modifying the AFM tip with nanoparticles, the interaction forces between nanoparticles and bacterial or mammalian cell membranes have been measured.<sup>40, 41</sup> Despite the importance of these studies, a mechanistic understanding of the interactions between nanoparticles and cell membranes is impeded by the complexity of the membranes. The use of model cell membranes with controlled membrane composition will allow for elucidation of nanoparticle-cell membrane interactions at a molecular level.

Although significant research efforts have been devoted to revealing the damage of lipid vesicles by nanoparticles, the distinction between “rupture” and “local disruption” of the lipid membrane is often unclear in previous studies. These two types of membrane damage, with contrasting degrees of severity, can have different biological implications. While cells may repair tiny disruptions on the membranes,<sup>42</sup> they may lose their integrity and undergo lysis if the membranes are ruptured significantly.<sup>43</sup> Yi and Chen<sup>37</sup> built supported vesicular layers (SVLs) on gold-coated QCM-D sensors and found that CNTs did not induce discernable rupture of the vesicles. It is not clear, however, whether the deposition of CNTs on the SVLs resulted in the formation of tiny pores on the vesicles. By encapsulating fluorescent dye into vesicles, the release of internal fluid from vesicles by nanoparticles has

been extensively examined.<sup>44-46</sup> Nevertheless, both complete rupture of vesicles and local disruption of lipid membranes can lead to the release of fluorescent dye, and the differentiation of these two processes has been largely overlooked in previous studies. By combining QCM-D measurements and fluorescent-dye experiments, which can reveal the rupture of vesicles and the formation of tiny pores on lipid membranes, respectively, we will be able to unambiguously differentiate the complete rupture of vesicles and the local disruption of lipid membranes.

While considerable efforts have been invested in examining the extent and speed of lipid membrane damage by nanoparticles, very few studies have investigated the reversibility of membrane damage. It is known that line tension can serve as a driving force for the closure of pores formed on the surface of vesicles.<sup>47, 48</sup> Numerous studies have provided evidence that lipid membranes possess a self-healing ability, i.e., the pores on the membranes can be spontaneously healed.<sup>47-50</sup> For instance, Kinoshita and Tsong<sup>42</sup> created pores on RBC membranes using electric pulses and observed the self-healing of the pores. To date, the resealing of pores induced by nanoparticle attachment has only received sporadic attention.<sup>50</sup> Given the recent evidence that GO can extract phospholipid from cell membranes,<sup>51</sup> it is of considerable interest to examine whether the damage to membranes caused by GO is reversible.

## **1.5 Biological Transformation of Nanoparticles**

When nanoparticles enter biological systems, inorganic and organic constituents in the biological fluids can readily adsorb on the nanoparticle surface, thereby impacting the surface chemistry of the nanoparticles. In biological fluids, a variety of types of proteins are

present. The adsorption of proteins results in the formation of protein coronas around the nanoparticles.<sup>52</sup> The presence of protein coronas can have significant impact on the cellular uptake and toxicity of nanoparticles.<sup>53, 54</sup> Recent studies have provided evidence that the presence of protein coronas can reduce the attachment of silica and silver nanoparticles to SLBs.<sup>38, 55</sup> Despite recent progress on nanoparticle-protein interactions, there remains a lack of understanding of the influence of solution chemistry on the adsorption of proteins on nanoparticles. When nanoparticles are transported among different biological compartments, the variation in solution chemistry conditions may lead to different amount of proteins adsorbed on nanoparticles as well as a change in the conformation of protein coronas. It remains to be elucidated how the nanoparticle-cell membrane interactions will be impacted by the presence of protein coronas formed under different solution chemistries. In addition, very limited efforts have been devoted to the direct force measurements between nanoparticles and lipid membranes in the presence of protein coronas. The delineation of the influence of protein coronas on nanoparticle-membrane interaction forces will allow for a better understanding of the impact of protein adsorption on the adhesion of nanoparticles to cell membranes.

In addition to proteins, inorganic phosphate ions are key constituents of biological fluids such as blood serum and saliva.<sup>56</sup> Some inorganic nanoparticles, including iron oxide and aluminum oxide, have high adsorption affinity toward phosphate ions.<sup>57</sup> Phosphate can adsorb on metal oxide nanoparticles through the formation of inner-sphere complexes thereby impacting the surface properties of the nanoparticles.<sup>58</sup> It has been reported that the adsorption of phosphate ions resulted in reversal of the surface charge of CeO<sub>2</sub> nanoparticles from positive to negative at neutral pH.<sup>59</sup> The change in the surface charge of nanoparticles

is expected to lead to an alteration in the electrostatic interactions between nanoparticles and cell membranes, thereby impacting the attachment of the nanoparticles to the membranes. At present, no studies have examined the effect of phosphate adsorption on the attachment of nanoparticles to lipid membranes.

## **1.6 Objectives and Scope of Dissertation**

The overarching goal of this research is to systematically investigate the influence of solution chemistry as well as inorganic and organic constituents of biological fluids on the interactions of engineered nanoparticles with model cell membranes. The emphasis will be placed on the attachment of nanoparticles to supported lipid bilayers, the disruption of lipid vesicles by nanoparticles, and the direct force measurements between nanoparticles and lipid bilayers. Specific objectives of this study include:

1. To investigate the influence of solution chemistry on the attachment of GO nanosheets to SLBs as well as the disruption of lipid vesicles by GO;
2. To examine the influence of solution chemistry on the adsorption of human serum albumin (HSA) proteins on GO, as well as the impact of protein adsorption on the attachment of GO to SLBs;
3. To unravel the impact of phosphate adsorption on the surface charge of inorganic (silica, ceria, and alumina) nanoparticles and their attachment to SLBs; and
4. To measure the interaction forces between AgNPs and lipid bilayers by the employment of nanoparticle-functionalized atomic force microscope (AFM) tips.

## 1.7 Dissertation Organization

Chapter 2 focuses on the investigation into the influence of solution chemistry on the interactions of GO nanosheets with model cell membranes using a quartz-crystal microbalance with dissipation monitoring (QCM-D). SLBs composed of zwitterionic 1,2-dioleoyl-*sn*-glycero-3-phosphocholine (DOPC) lipids were constructed on QCM-D sensors as model cell membranes. The deposition of GO to SLBs was investigated at neutral pH over a wide range of NaCl and CaCl<sub>2</sub> concentrations. The deposition kinetics of GO on SLBs were derived by normalizing the rates of GO deposition on SLBs to the favorable deposition rates of GO on positively charged surfaces under the same solution chemistry condition. The release of GO upon favorable attachment to supported lipid bilayers was examined through rinsing the deposited GO layer with electrolyte solutions. Supported vesicular layers that were encapsulated with fluorescent dye were also constructed on QCM-D sensors as another model for cell membranes. The propensity for GO to disrupt the lipid membrane was examined by monitoring the release of dye from inside the vesicles. The reversibility of the disruption of lipid membranes was explored by monitoring the dye release upon termination of the exposure of the vesicles to GO suspensions.

In Chapter 3, the adsorption of HSA proteins on GO was investigated under varying solution chemistry conditions. The dry mass of HSA adsorption on GO was studied through batch experiments, and the information concerning the wet mass and conformation of HSA layers on GO was derived through the QCM-D measurements which involve the use of GO-coated sensors. The influence of ionic strength, presence of calcium, and pH conditions on the adsorption of HSA and the conformation of adsorbed HSA layers was examined. Furthermore, the attachment of GO on DOPC SLBs in the absence and presence of HSA was

investigated under different ionic strength conditions at neutral pH in order to elucidate the role of protein layer conformation in determining nanoparticle-membrane interactions.

Chapter 4 focuses on the aggregation and interactions of chemical mechanical planarization (CMP) nanoparticles (i.e., colloidal silica, fumed silica, ceria, and alumina) with model cell membranes, with an emphasis on the role of phosphate adsorption. The adsorption of phosphate ions on the four CMP nanoparticles was investigated through batch adsorption experiments. The influence of phosphate adsorption on the electrophoretic mobilities and aggregation behaviors of the CMP nanoparticles at neutral pH conditions was studied. In addition, the deposition kinetics of CMP nanoparticles to DOPC SLBs was examined in the absence and presence of phosphate. Finally, the disruption of supported vesicular layers by the CMP nanoparticles under neutral pH conditions was investigated.

In Chapter 5, a method was first developed to functionalize AFM tips with AgNPs by sequentially exposing the tips to polydopamine (PDA) and silver nitrate solutions. The modified tips were observed under a scanning electron microscope (SEM). Secondary and backscattered electron SEM imaging were conducted to reveal the morphology and surface composition of the modified tips, respectively. DOPC SLBs were constructed on mica surfaces as model cell membranes. The interaction forces between the AgNP-modified AFM tips and SLBs were measured at neutral pH condition in the absence and presence of HSA. The forces required for the AgNPs to penetrate the SLBs were also compared in the absence and presence of HSA.

## 1.8 References

1. Nel, A.; Xia, T.; Madler, L.; Li, N., Toxic potential of materials at the nanolevel. *Science* **2006**, *311*, (5761), 622-7.

2. Fadeel, B.; Garcia-Bennett, A. E., Better safe than sorry: Understanding the toxicological properties of inorganic nanoparticles manufactured for biomedical applications. *Adv. Drug Delivery Rev.* **2010**, *62*, (3), 362-374.
3. Dreyer, D. R.; Park, S.; Bielawski, C. W.; Ruoff, R. S., The chemistry of graphene oxide. *Chem. Soc. Rev.* **2010**, *39*, (1), 228-40.
4. Liu, Z.; Robinson, J. T.; Sun, X. M.; Dai, H. J., PEGylated nano-graphene oxide for delivery of water-insoluble cancer drugs. *J. Am. Chem. Soc.* **2008**, *130*, (33), 10876-10877.
5. Sun, X. M.; Liu, Z.; Welsher, K.; Robinson, J. T.; Goodwin, A.; Zaric, S.; Dai, H. J., Nano-Graphene Oxide for Cellular Imaging and Drug Delivery. *Nano Res* **2008**, *1*, (3), 203-212.
6. Yoon, H. J.; Kim, T. H.; Zhang, Z.; Azizi, E.; Pham, T. M.; Paoletti, C.; Lin, J.; Ramnath, N.; Wicha, M. S.; Hayes, D. F.; Simeone, D. M.; Nagraath, S., Sensitive capture of circulating tumour cells by functionalized graphene oxide nanosheets. *Nat. Nanotechnol.* **2013**, *8*, (10), 735-741.
7. Benn, T. M.; Westerhoff, P., Nanoparticle silver released into water from commercially available sock fabrics. *Environ. Sci. Technol.* **2008**, *42*, (11), 4133-4139.
8. Li, Q. L.; Mahendra, S.; Lyon, D. Y.; Brunet, L.; Liga, M. V.; Li, D.; Alvarez, P. J. J., Antimicrobial nanomaterials for water disinfection and microbial control: Potential applications and implications. *Water Res.* **2008**, *42*, (18), 4591-4602.
9. Mueller, N. C.; Nowack, B., Exposure modeling of engineered nanoparticles in the environment. *Environ. Sci. Technol.* **2008**, *42*, (12), 4447-4453.
10. Batley, G. E.; Kirby, J. K.; McLaughlin, M. J., Fate and Risks of Nanomaterials in Aquatic and Terrestrial Environments. *Acc. Chem. Res.* **2013**, *46*, (3), 854-862.
11. Vance, M. E.; Kuiken, T.; Vejerano, E. P.; McGinnis, S. P.; Hochella, M. F.; Rejeski, D.; Hull, M. S., Nanotechnology in the real world: Redeveloping the nanomaterial consumer products inventory. *Beilstein J Nanotech* **2015**, *6*, 1769-1780.
12. Liao, K. H.; Lin, Y. S.; Macosko, C. W.; Haynes, C. L., Cytotoxicity of Graphene Oxide and Graphene in Human Erythrocytes and Skin Fibroblasts. *ACS Appl. Mater. Interfaces* **2011**, *3*, (7), 2607-2615.
13. Perreault, F.; de Faria, A. F.; Nejati, S.; Elimelech, M., Antimicrobial Properties of Graphene Oxide Nanosheets: Why Size Matters. *ACS Nano* **2015**, *9*, (7), 7226-7236.
14. Zodrow, K.; Brunet, L.; Mahendra, S.; Li, D.; Zhang, A.; Li, Q. L.; Alvarez, P. J. J., Polysulfone ultrafiltration membranes impregnated with silver nanoparticles show improved biofouling resistance and virus removal. *Water Res.* **2009**, *43*, (3), 715-723.
15. Sondi, I.; Salopek-Sondi, B., Silver nanoparticles as antimicrobial agent: a case study on E-coli as a model for Gram-negative bacteria. *J. Colloid Interface Sci.* **2004**, *275*, (1), 177-182.
16. Yu, T.; Malugin, A.; Ghandehari, H., Impact of Silica Nanoparticle Design on Cellular Toxicity and Hemolytic Activity. *ACS Nano* **2011**, *5*, (7), 5717-5728.
17. Chen, J. N.; Peng, H.; Wang, X. P.; Shao, F.; Yuan, Z. D.; Han, H. Y., Graphene oxide exhibits broad-spectrum antimicrobial activity against bacterial phytopathogens and fungal conidia by intertwining and membrane perturbation. *Nanoscale* **2014**, *6*, (3), 1879-1889.
18. Akhavan, O.; Ghaderi, E., Toxicity of Graphene and Graphene Oxide Nanowalls Against Bacteria. *ACS Nano* **2010**, *4*, (10), 5731-5736.

19. Zhao, Y. N.; Sun, X. X.; Zhang, G. N.; Trewyn, B. G.; Slowing, I. I.; Lin, V. S. Y., Interaction of Mesoporous Silica Nanoparticles with Human Red Blood Cell Membranes: Size and Surface Effects. *ACS Nano* **2011**, *5*, (2), 1366-1375.
20. Li, Y.; Zhang, W.; Niu, J. F.; Chen, Y. S., Mechanism of Photogenerated Reactive Oxygen Species and Correlation with the Antibacterial Properties of Engineered Metal-Oxide Nanoparticles. *ACS Nano* **2012**, *6*, (6), 5164-5173.
21. Carlson, C.; Hussain, S. M.; Schrand, A. M.; Braydich-Stolle, L. K.; Hess, K. L.; Jones, R. L.; Schlager, J. J., Unique Cellular Interaction of Silver Nanoparticles: Size-Dependent Generation of Reactive Oxygen Species. *J. Phys. Chem. B* **2008**, *112*, (43), 13608-13619.
22. Vecitis, C. D.; Zodrow, K. R.; Kang, S.; Elimelech, M., Electronic-Structure-Dependent Bacterial Cytotoxicity of Single-Walled Carbon Nanotubes. *ACS Nano* **2010**, *4*, (9), 5471-5479.
23. Liu, S. B.; Zeng, T. H.; Hofmann, M.; Burcombe, E.; Wei, J.; Jiang, R. R.; Kong, J.; Chen, Y., Antibacterial Activity of Graphite, Graphite Oxide, Graphene Oxide, and Reduced Graphene Oxide: Membrane and Oxidative Stress. *ACS Nano* **2011**, *5*, (9), 6971-6980.
24. Andersen, O. S.; Koeppe, R. E., Bilayer thickness and membrane protein function: An energetic perspective. *Annu. Rev. Biophys. Biomol. Struct.* **2007**, *36*, 107-130.
25. Simons, K.; Ikonen, E., Functional rafts in cell membranes. *Nature* **1997**, *387*, (6633), 569-572.
26. Jorgensen, P. L., Mechanism of the Na<sup>+</sup>, K<sup>+</sup> Pump Protein-Structure and Conformations of the Pure (Na<sup>+</sup> +K<sup>+</sup>)-Atpase. *Biochim. Biophys. Acta* **1982**, *694*, (1), 27-68.
27. Mouritsen, O. G.; Zuckermann, M. J., What's so special about cholesterol? *Lipids* **2004**, *39*, (11), 1101-1113.
28. Hartono, D.; Hody; Yang, K. L.; Yung, L. Y. L., The effect of cholesterol on protein-coated gold nanoparticle binding to liquid crystal-supported models of cell membranes. *Biomaterials* **2010**, *31*, (11), 3008-3015.
29. Chen, K. L.; Bothun, G. D., Nanoparticles Meet Cell Membranes: Probing Nonspecific Interactions. using Model Membranes. *Environ. Sci. Technol.* **2014**, *48*, (2), 873-880.
30. Richter, R. P.; Berat, R.; Brisson, A. R., Formation of solid-supported lipid bilayers: An integrated view. *Langmuir* **2006**, *22*, (8), 3497-3505.
31. Gozen, I.; Jesorka, A., Instrumental Methods to Characterize Molecular Phospholipid Films on Solid Supports. *Anal. Chem.* **2012**, *84*, (2), 822-838.
32. Gunsolus, I. L.; Haynes, C. L., Analytical Aspects of Nanotoxicology. *Anal. Chem.* **2015**.
33. Brian, A. A.; McConnell, H. M., Allogeneic Stimulation of Cyto-Toxic T-Cells by Supported Planar Membranes. *Proceedings of the National Academy of Sciences of the United States of America-Biological Sciences* **1984**, *81*, (19), 6159-6163.
34. Cho, N. J.; Frank, C. W.; Kasemo, B.; Hook, F., Quartz crystal microbalance with dissipation monitoring of supported lipid bilayers on various substrates. *Nat. Protoc.* **2010**, *5*, (6), 1096-106.
35. Vigneault, B.; Percot, A.; Lafleur, M.; Campbell, P. G. C., Permeability changes in model and phytoplankton membranes in the presence of aquatic humic substances. *Environ. Sci. Technol.* **2000**, *34*, (18), 3907-3913.



36. Zhang, X. F.; Yang, S. H., Nonspecific Adsorption of Charged Quantum Dots on Supported Zwitterionic Lipid Bilayers: Real-Time Monitoring by Quartz Crystal Microbalance with Dissipation. *Langmuir* **2011**, *27*, (6), 2528-2535.
37. Yi, P.; Chen, K. L., Interaction of Multiwalled Carbon Nanotubes with Supported Lipid Bilayers and Vesicles as Model Biological Membranes. *Environ. Sci. Technol.* **2013**, *47*, (11), 5711-5719.
38. Wang, Q. Y.; Lim, M. H.; Liu, X. T.; Wang, Z. W.; Chen, K. L., Influence of Solution Chemistry and Soft Protein Coronas on the Interactions of Silver Nanoparticles with Model Biological Membranes. *Environ. Sci. Technol.* **2016**, *50*, (5), 2301-2309.
39. Israelachvili, J. N., *Intermolecular and surface forces: revised third edition*. Academic press: 2011.
40. Romero-Vargas Castrillón, S.; Perreault, F.; de Faria, A. F.; Elimelech, M., Interaction of Graphene Oxide with Bacterial Cell Membranes: Insights from Force Spectroscopy. *Environ. Sci. Technol. Lett.* **2015**, *2*, (4), 112-117.
41. Pyrgiotakis, G.; Blattmann, C. O.; Demokritou, P., Real-Time Nanoparticle-Cell Interactions in Physiological Media by Atomic Force Microscopy. *ACS Sustainable Chem. Eng.* **2014**, *2*, (7), 1681-1690.
42. Kinosita, K.; Tsong, T. Y., Formation and Resealing of Pores of Controlled Sizes in Human Erythrocyte-Membrane. *Nature* **1977**, *268*, (5619), 438-441.
43. Yu, J.; Fischman, D. A.; Steck, T. L., Selective solubilization of proteins and phospholipids from red blood cell membranes by nonionic detergents. *Journal of supramolecular structure* **1973**, *1*, (3), 233-248.
44. Goodman, C. M.; McCusker, C. D.; Yilmaz, T.; Rotello, V. M., Toxicity of gold nanoparticles functionalized with cationic and anionic side chains. *Bioconjugate Chem.* **2004**, *15*, (4), 897-900.
45. Moghadam, B. Y.; Hou, W. C.; Corredor, C.; Westerhoff, P.; Posner, J. D., Role of nanoparticle surface functionality in the disruption of model cell membranes. *Langmuir* **2012**, *28*, (47), 16318-26.
46. Ip, A. C.; Liu, B.; Huang, P. J.; Liu, J., Oxidation level-dependent zwitterionic liposome adsorption and rupture by graphene-based materials and light-induced content release. *Small* **2013**, *9*, (7), 1030-5.
47. Sandre, O.; Moreaux, L.; Brochard-Wyart, F., Dynamics of transient pores in stretched vesicles. *Proc. Natl. Acad. Sci. U. S. A.* **1999**, *96*, (19), 10591-10596.
48. Karatekin, E.; Sandre, O.; Guitouni, H.; Borghi, N.; Puech, P. H.; Brochard-Wyart, F., Cascades of transient pores in giant vesicles: Line tension and transport. *Biophys. J.* **2003**, *84*, (3), 1734-1749.
49. Brochard-Wyart, F.; de Gennes, P. G.; Sandre, O., Transient pores in stretched vesicles: role of leak-out. *Physica A* **2000**, *278*, (1-2), 32-51.
50. Wang, F.; Liu, J. W., Self-healable and reversible liposome leakage by citrate-capped gold nanoparticles: probing the initial adsorption/desorption induced lipid phase transition. *Nanoscale* **2015**, *7*, (38), 15599-15604.
51. Tu, Y. S.; Lv, M.; Xiu, P.; Huynh, T.; Zhang, M.; Castelli, M.; Liu, Z. R.; Huang, Q.; Fan, C. H.; Fang, H. P.; Zhou, R. H., Destructive extraction of phospholipids from Escherichia coli membranes by graphene nanosheets. *Nat. Nanotechnol.* **2013**, *8*, (12), 594-601.

52. Cedervall, T.; Lynch, I.; Lindman, S.; Berggard, T.; Thulin, E.; Nilsson, H.; Dawson, K. A.; Linse, S., Understanding the nanoparticle-protein corona using methods to quantify exchange rates and affinities of proteins for nanoparticles. *Proc. Natl. Acad. Sci. U. S. A.* **2007**, *104*, (7), 2050-2055.
53. Hu, W. B.; Peng, C.; Lv, M.; Li, X. M.; Zhang, Y. J.; Chen, N.; Fan, C. H.; Huang, Q., Protein Corona-Mediated Mitigation of Cytotoxicity of Graphene Oxide. *ACS Nano* **2011**, *5*, (5), 3693-3700.
54. Lesniak, A.; Fenaroli, F.; Monopoli, M. R.; Aberg, C.; Dawson, K. A.; Salvati, A., Effects of the Presence or Absence of a Protein Corona on Silica Nanoparticle Uptake and Impact on Cells. *ACS Nano* **2012**, *6*, (7), 5845-5857.
55. Lesniak, A.; Salvati, A.; Santos-Martinez, M. J.; Radomski, M. W.; Dawson, K. A.; Aberg, C., Nanoparticle adhesion to the cell membrane and its effect on nanoparticle uptake efficiency. *J. Am. Chem. Soc.* **2013**, *135*, (4), 1438-44.
56. Tobey, S. L.; Anslyn, E. V., Determination of inorganic phosphate in serum and saliva using a synthetic receptor. *Org. Lett.* **2003**, *5*, (12), 2029-2031.
57. Mudunkotuwa, I. A.; Grassian, V. H., Biological and environmental media control oxide nanoparticle surface composition: the roles of biological components (proteins and amino acids), inorganic oxyanions and humic acid. *Environmental Science: Nano* **2015**, *2*, (5), 429-439.
58. Bleam, W. F.; Pfeffer, P. E.; Goldberg, S.; Taylor, R. W.; Dudley, R., A P-31 Solid-State Nuclear-Magnetic-Resonance Study of Phosphate Adsorption at the Boehmite Aqueous-Solution Interface. *Langmuir* **1991**, *7*, (8), 1702-1712.
59. Van Hoecke, K.; Quik, J. T. K.; Mankiewicz-Boczek, J.; De Schamphelaere, K. A. C.; Elsaesser, A.; Van der Meeren, P.; Barnes, C.; McKerr, G.; Howard, C. V.; Van De Meent, D.; Rydzynski, K.; Dawson, K. A.; Salvati, A.; Lesniak, A.; Lynch, I.; Silversmit, G.; De Samber, B.; Vincze, L.; Janssen, C. R., Fate and Effects of CeO<sub>2</sub> Nanoparticles in Aquatic Ecotoxicity Tests. *Environ. Sci. Technol.* **2009**, *43*, (12), 4537-4546.

## **Chapter 2. Interactions of Graphene Oxide with Model Cell Membranes: Probing Nanoparticle Attachment and Lipid Bilayer Disruption<sup>1</sup>**

---

<sup>1</sup> This chapter has been published as: Liu, X. T. and Chen, K. L., Interactions of Graphene Oxide with Model Cell Membranes: Probing Nanoparticle Attachment and Lipid Bilayer Disruption, *Langmuir*, 2015, 31, 12076–12086. DOI: 10.1021/acs.langmuir.5b02414. Copyright 2015 American Chemical Society (ACS). Reproduced/modified with permission from ACS.

## 2.1 Introduction

Graphene is a two-dimensional nanomaterial consisting of a single layer of carbon atoms.<sup>1, 2</sup> Owing to its unique structure, graphene possesses extraordinary electrical,<sup>3</sup> optical,<sup>4</sup> thermal,<sup>5</sup> and mechanical<sup>6</sup> properties. Graphene oxide (GO) is the oxidized form of graphene and it contains carboxyl, epoxy, and hydroxyl groups on its edges and basal planes.<sup>7</sup> GO has been used as the precursor for the chemical production of graphene sheets.<sup>8</sup> Furthermore, GO has found broad applications in cell imaging,<sup>9</sup> drug delivery,<sup>9, 10</sup> environmental sensors,<sup>11</sup> and the fabrication of water filtration and gas separation membranes.<sup>11-15</sup>

Recently, GO has been reported to exhibit toxicity effects on gram-negative and gram-positive bacteria,<sup>16-19</sup> as well as human cell lines.<sup>20, 21</sup> The observed cytotoxicity of GO necessitates the further elucidation of the toxicity mechanisms in order to allow for the safe design of GO-based materials. Currently, the mechanisms for the cytotoxicity of GO are still being investigated. Some mechanisms that have been reported include destructive lipid extraction,<sup>22</sup> oxidative stress toward cell components,<sup>16, 17</sup> coating of cell membranes to prohibit cell proliferation,<sup>17</sup> and penetration of lipid membranes by the edge asperities and corners of GO nanosheets.<sup>23, 24</sup> The nonspecific interactions between GO and lipid bilayers (or interactions that do not involve specific cell receptors)<sup>25, 26</sup> are expected to play a significant role in controlling the direct contact of GO with cell membranes, which is likely to be a critical initial process for the proposed mechanisms for GO cytotoxicity.<sup>25, 26</sup>

In light of the inherent complexity and dynamic nature of cell membranes, artificial membranes that are composed of lipid bilayers are commonly used as model systems to gain fundamental insights into the nonspecific interactions of cell membranes with

nanoparticles.<sup>25, 27, 28</sup> Planar supported lipid bilayers (SLBs) have been employed as such models in the evaluation of the propensity for silica nanoparticles<sup>29</sup> and quantum dots<sup>30</sup> to attach to membranes. In our earlier work,<sup>31</sup> SLBs were assembled in a quartz crystal microbalance with dissipation monitoring (QCM-D) and were used for the quantification of the propensities for nanoparticle attachment in different solution chemistries. In addition to SLBs, lipid vesicles (or liposomes) are another important model for the investigation of the cell membrane integrity upon the attachment of nanoparticles.<sup>25</sup> Specifically, the disruption of vesicles by nanoparticles can result in the release or leakage of the fluid from within the vesicles, which can be monitored either through mass measurements using the QCM-D or dye release measurements from within the vesicles.<sup>25</sup>

While current studies have provided some insights into the nature of the interactions between GO and cell membranes, several important questions still remain to be answered. First, the propensity for GO to attach to cell membranes has not been quantitatively assessed and the reversibility of GO attachment on cell membranes has only received sporadic attention.<sup>17, 32</sup> Second, only a few studies have accounted for the influence of solution chemistry in the assessment of the interactions between GO and cell membranes.<sup>33, 34</sup> The variation in electrolyte concentrations in natural aquatic systems (e.g., rivers and estuaries) and biological systems (e.g., physiological fluids) is expected to lead to a change in GO–cell membrane interactions through the alteration of electrostatic interactions between GO and lipid bilayers. Hence, a better understanding of the factors controlling GO–membrane attachment will facilitate the elucidation of the mechanisms for the biological effects of GO in different environments. Third, although previous studies have demonstrated that GO can impair the integrity of bacterial and mammalian cells,<sup>21, 22</sup> it is still unclear whether there is a

correlation between the attachment of GO on cell membranes and the disruption of cell membranes by GO.

In an effort to answer these questions, we employed a QCM-D to study the propensity for GO to attach to lipid membranes, as well as the reversibility of GO–membrane attachment, as a function of solution chemistry. We also coupled a fluorescent-dye based technique with the QCM-D in order to monitor the leakage of vesicles upon contacting GO. The results obtained in this study will improve our understanding on the nonspecific interactions of GO with lipid membranes in a more quantitative manner and may be instructive on the role of GO attachment and membrane disruption during the assessment of the cytotoxicity of GO in aqueous environments of different solution chemistries.

## **2.2 Materials and Methods**

### **2.2.1 Preparation and Characterization of GO Suspensions**

Dry GO powder was purchased from Graphene Laboratories Inc. (Calverton, New York). According to the supplier, the GO contains 79 % carbon and 20 % oxygen and has a flake size in the range of 0.5–5.0  $\mu\text{m}$ . Additionally, at least 80 % of the GO platelets consist of only one layer of carbon atoms. To prepare the GO suspensions, ca. 8 mg of the GO powder was dispersed in 200 mL deionized (DI) water (Millipore, MA) through ultrasonication in an ultrasonic bath (Branson 1510R-MT, output power 70 W, frequency 42 kHz) for 24 h. The suspension was filtered through a 0.2  $\mu\text{m}$  cellulose acetate filter (Corning, NY) and stored in a clean Pyrex bottle in the dark at 4 °C. Two batches of GO suspensions were prepared and used within six months after preparation. The average hydrodynamic sizes of the first and second batches were determined to be  $136 \pm 7$  and  $119 \pm$

3 nm, respectively, through dynamic light scattering (DLS, BI-200SM and BI-9000AT, Brookhaven, NY).

### 2.2.2 Solution Chemistry

ACS-grade NaCl, CaCl<sub>2</sub>, and NaHCO<sub>3</sub> stock solutions were prepared and filtered using 0.1- $\mu$ m syringe filters (Millipore, MA). Most experiments were conducted at pH 7.2  $\pm$  0.2 (buffered with 0.2 mM NaHCO<sub>3</sub>). Four buffers containing *N*-(2-hydroxyethyl)-piperazine-*N'*-(2-ethanesulfonic acid) (HEPES, Sigma-Aldrich) were used in the experiments. They are denoted as Buffer A (10 mM HEPES, 150 mM NaCl, pH adjusted to 7.4), Buffer B (10 mM HEPES, 100 mM NaCl, with unadjusted pH ca. 5.5), Buffer C (20 mM HEPES, 150 mM NaCl, pH adjusted to 7.4), and Buffer D (10 mM HEPES, no NaCl, pH adjusted to 7.4).

### 2.2.3 Preparation of Vesicle Stock Suspensions

Zwitterionic 1,2-dioleoyl-*sn*-glycero-3-phosphocholine (DOPC) and positively-charged 1,2-dioleoyl-*sn*-glycero-3-ethylphosphocholine (DOEPC) solutions in chloroform (Avanti Polar Lipids Inc., Alabaster, AL) were used to prepare zwitterionic DOPC vesicles and positively charged, mixed-lipid vesicles composed of DOPC and DOEPC. For the preparation of DOPC vesicles, 0.2 mL of 25 g/L DOPC solution was dried in a conical flask with an ultrapure nitrogen gas stream to form a DOPC thin film on the bottom of the flask. The DOPC film was subjected to vacuum desiccation in nitrogen for at least 4 h and then hydrated by adding 5 mL Buffer A followed by magnetic stirring for ca. 30 min. The DOPC suspension was then extruded using a mini-extruder (Avanti Polar Lipids Inc.) through a 50-nm polycarbonate membrane (Whatman) back and forth for at least 15 times to obtain

unilamellar vesicles with a hydrodynamic diameter of 91–94 nm.<sup>35</sup> For the preparation of positively charged DOPC–DOEPC vesicles, a 25 g/L DOPC solution and a 10 g/L DOEPC solution were mixed at a lipid mass ratio of 3:1 to obtain DOPC and DOEPC concentrations of 13.6 and 4.5 g/L, respectively. Then, 0.2 mL of the DOPC–DOEPC mixture was dried with an ultrapure nitrogen gas stream, vacuum desiccated, hydrated with Buffer D, and extruded for 15 times. The resulting DOPC–DOEPC suspension had DOPC and DOEPC concentrations of 0.54 and 0.18 g/L, respectively. All vesicle suspensions were stored in glass vials that were sealed with nitrogen gas at 4 °C and used within four days after preparation.

#### **2.2.4 Preparation of Vesicles Encapsulated with Fluorescent Dye**

The preparation procedure for DOPC vesicles encapsulated with a fluorescent dye was adopted from the method of Moghadam et al.<sup>28</sup> First, 5(6)-carboxyfluorescein (CF) (Molecular Probes, Eugene, OR) was dissolved in Buffer C with pH readjusted to 7.4 using KOH. The resulting maroon-colored CF solution (100 mM) was stored in dark at 4 °C and used within two months after preparation. The CF solution was used to hydrate the DOPC film and extrusion was performed using the method described in the previous section. The resulting vesicle suspension, to be referred to as CF-DOPC vesicle suspension, was stored in a glass vial wrapped with aluminum foil at 4 °C and used within four days after preparation.

#### **2.2.5 Electrophoretic Mobility and Dynamic Light Scattering Measurements**

The electrophoretic mobilities (EPMs) of GO and DOPC-DOEPC vesicles prepared in 0.2 mM NaHCO<sub>3</sub> solutions were measured (ZetaPALS, Brookhaven Instruments Corp., Holtsville, NY) over a range of NaCl and CaCl<sub>2</sub> concentrations. The concentration of GO



used for the EPM measurements was ca. 2.6 mg/L as total organic carbon (TOC) determined using a TOC analyzer (TOC-L, Shimadzu), while the concentration of DOPC–DOEPC vesicles used was 36 mg/L. Three samples were measured at each electrolyte concentration. For most experimental conditions, ten measurements were conducted for each sample. At high NaCl and CaCl<sub>2</sub> concentrations, only five measurements were conducted in order to minimize the effect of aggregation of GO and vesicles. In addition, the aggregation of GO was investigated by measuring the change in the hydrodynamic diameter with time through time-resolved DLS. These measurements were conducted over a range of NaCl and CaCl<sub>2</sub> concentrations at pH 7.2 using the method presented in our earlier publication.<sup>36</sup>

### **2.2.6 Quartz Crystal Microbalance with Dissipation Monitoring**

The interactions of GO with DOPC SLBs and vesicles were studied using a QCM-D E4 setup (Biolin Scientific, Västra Frölunda, Sweden). The system is equipped with four measurement chambers, each housing a 5 MHz quartz crystal sensor with either silica-coated (QSX 303) or gold-coated (QSX 301) surface. Before the QCM-D experiments, the flow modules and sensors were first cleaned using a protocol that was reported in our previous paper.<sup>31</sup> The temperature inside the QCM-D chambers was maintained at 25 °C. For all the experiments, the shifts in frequency and energy dissipation at the 3<sup>rd</sup> overtone ( $\Delta f_3$  and  $\Delta D_3$ , respectively) were monitored simultaneously. The frequency and dissipation shifts provide information on the deposited mass and the viscoelastic properties of the deposited layer on the sensor, respectively.<sup>37</sup> In previous studies on the deposition of multiwalled carbon nanotubes<sup>38</sup> and GO<sup>39</sup> on silica surfaces, it has been demonstrated that the rate of frequency shift was proportional to the rate of deposition. Thus, in this study, the rate of frequency shift at the 3<sup>rd</sup> overtone was used to quantify the deposition rates of GO on SLBs.

For the deposition of GO on SLBs, a SLB was first assembled on the surface of silica-coated sensor using the method of Keller and Kasemo.<sup>40</sup> Briefly, after a stable baseline was achieved (i.e., frequency signal drifts of less than 0.2 Hz within 10 min) by rinsing the sensor with Buffer A, a 0.07 g/L DOPC vesicle suspension was introduced to the QCM-D chamber. The vesicles deposited on the sensor and subsequently ruptured to form a DOPC SLB, resulting in a characteristic frequency shift of  $-25 \pm 0.5$  Hz and a dissipation shift of  $0.1 \times 10^{-6}$ . A similar approach adapted from the method of Cho et al.<sup>35</sup> was used for the formation of DOPC–DOEPC SLBs. A mixture of 0.038 g/L DOPC and 0.013 g/L DOEPC vesicles prepared in Buffer D was used to form the SLB. The formation of a DOPC–DOEPC SLB led to a frequency shift of  $-24.4$  Hz and a dissipation shift of  $0.1 \times 10^{-6}$ . After the formation of SLBs, the chamber was rinsed with Buffer A (for DOPC SLBs) or Buffer D (for DOPC–DOEPC SLBs) for 10 min to remove the remaining vesicles. An electrolyte solution of interest was then introduced into the measurement chamber to obtain a stable baseline, followed by the introduction of GO prepared in the same electrolyte solution to initiate the deposition process. The GO concentration used for all QCM-D experiments was 2.6 mg/L TOC. The flow rates were maintained at  $0.10 \pm 0.002$  mL/min using a peristaltic pump (ISM935C, Ismatec SA, Zürich, Switzerland). This flow rate resulted in a laminar flow in the measurement chambers.<sup>41</sup>

In order to quantify the deposition kinetics of GO on SLBs, the attachment efficiency,  $\alpha$ , was calculated by normalizing the rates of frequency shift on SLBs to the rates under favorable (or transport-limited) conditions at the same solution chemistry.<sup>42</sup>

$$\alpha = \frac{d\Delta f_3 / dt}{(d\Delta f_3 / dt)_{fav}} \quad (2.1)$$

where  $t$  represents time. The attachment efficiency can be understood as the probability of an attachment resulting from the collision between a GO nanoparticle and a SLB.<sup>43</sup> The favorable deposition conditions were achieved by coating the silica sensor with poly-L-lysine (PLL) (prepared in Buffer B),<sup>42, 44</sup> which is positively charged at pH 7.2. All the rates of frequency shift used to calculate attachment efficiencies were determined within the first 10 min of GO deposition.

In order to evaluate the propensity for GO to rupture vesicles, a supported vesicular layer (SVL) was formed on a gold-coated sensor.<sup>31, 40, 45</sup> The chamber was first rinsed with Buffer A to attain a stable baseline and a 0.05 g/L DOPC vesicle suspension prepared in Buffer A was introduced into the chambers for ca. 30 min. The vesicles deposited on the gold surface to form a SVL. The chamber was then rinsed with Buffer A to remove the vesicles that remained in the solution. Following that, a stable baseline was obtained by rinsing with an electrolyte of interest before a GO suspension prepared in the same electrolyte was introduced into the chamber. The same procedure was used for the formation of a CF-DOPC SVL, except that Buffer C, instead of Buffer A, was used throughout the experiment.

### **2.2.7 Detection of Dye Leakage from Supported Vesicles**

After the formation of a CF-DOPC SVL on a gold-coated sensor, the CF dye outside the vesicles was removed by rinsing the chamber with Buffer C for at least 2 h. This rinsing step was effective to reduce the CF concentration in the outflow of QCM-D system to lower than 0.05  $\mu\text{M}$ . The deposition of GO on the SVL was conducted according to the procedures

described above and the outflow samples were collected for 10 min per sample. The fluorescence of the samples was measured using a spectrofluorometer (Fluorolog, Horiba) at excitation and emission wavelengths of 490 and 517 nm, respectively. The presence of GO was shown to have negligible influence on the fluorescence intensity of CF, as shown in Figure 2.1.

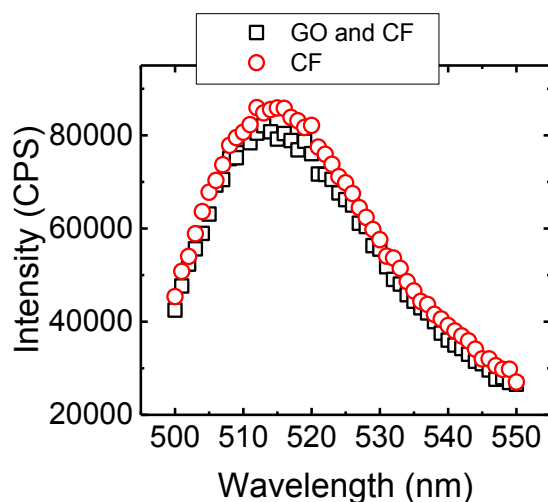


**Figure 2.1.** Effect of GO on the fluorescence intensity of 1  $\mu\text{M}$  CF dye dissolved in HEPES buffer. The concentration of GO was 2.6 mg/L TOC.

## 2.3 Results and Discussion

### 2.3.1 Electrokinetic properties of GO

Figure 2.2 presents the EPMS of GO in NaCl and CaCl<sub>2</sub> solutions at pH 7.2. The negative EPMS indicate that GO carried negative charge within the range of electrolyte concentrations employed. The negative charge of GO was attributed to the deprotonation of carboxyl groups on the surface and edges of GO.<sup>7, 8</sup> As the NaCl concentration was

increased, the magnitude of EPMs became smaller due to the screening of the surface charge of GO. The decrease in EPMs with increasing  $\text{CaCl}_2$  concentration was mainly due to charge neutralization that resulted from the binding of  $\text{Ca}^{2+}$  ions to the carboxyl groups on GO.<sup>31, 46</sup>

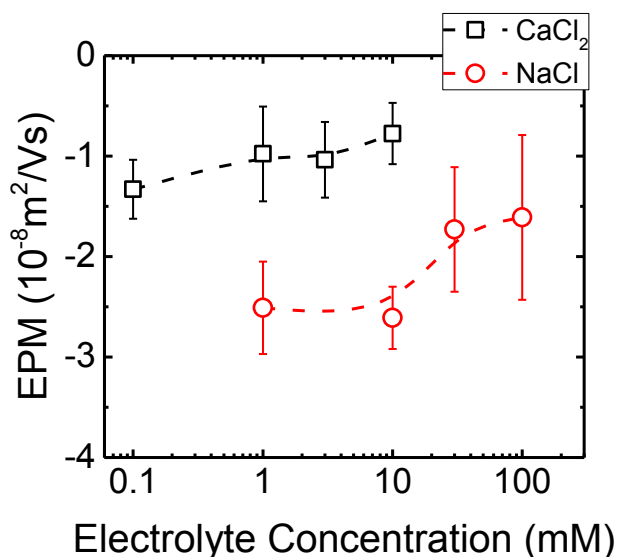


**Figure 2.2** EPMs of GO as functions of NaCl and  $\text{CaCl}_2$  concentrations at pH 7.2. Error bars represent standard deviations. The lines are meant to guide the eye.

### 2.3.2 Deposition Kinetics of GO on SLBs

Representative frequency and dissipation shifts during the formation of a DOPC SLB on a silica-coated sensor and during the deposition of GO on the SLB are shown in Figure 2.3. The silica-coated sensor was first rinsed with Buffer A until stable frequency and dissipation baselines were achieved. A suspension of DOPC vesicles was introduced into the flow chamber and the adsorption of vesicles on the sensor resulted in a negative frequency shift and a positive dissipation shift. As more and more vesicles adsorbed on the sensor, a critical surface coverage was achieved and the interaction between neighboring vesicles, as

well as that between vesicles and silica surface, resulted in the rupture of vesicles.<sup>40, 47, 48</sup> Upon rupture, the water that was encapsulated within the vesicles was released, causing a positive frequency shift and a negative dissipation shift. The formation of the DOPC SLB resulted in a  $\Delta f$  value of  $-25$  Hz and a  $\Delta D$  value of  $0.1 \times 10^{-6}$ , both consistent with the values reported by other researchers.<sup>35, 47</sup> Richter et al.<sup>47</sup> employed a B5 protein that adsorbs favorably on silica surfaces to study the integrity of the SLBs formed using this protocol. No protein binding was detected by the QCM-D, thus indicating that the SLBs on the silica surfaces were continuous.<sup>47</sup>

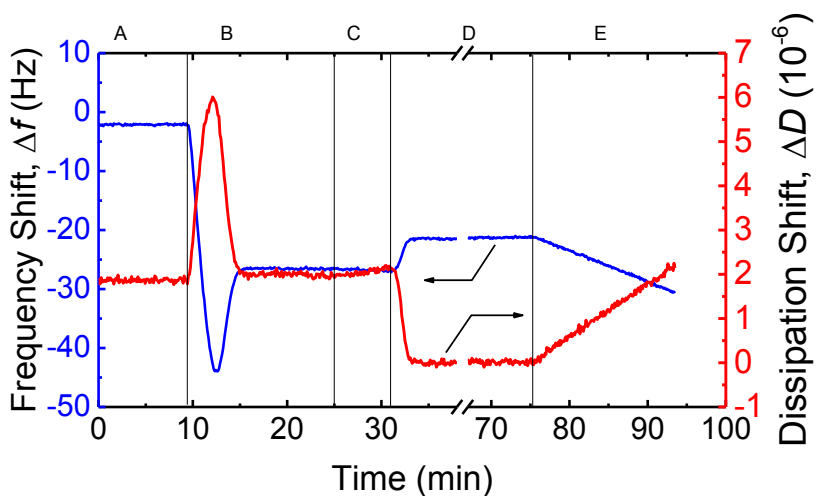


**Figure 2.3.** Representative frequency (blue) and dissipation (red) shifts during the formation of a DOPC SLB on a silica crystal and the deposition of GO on the SLB. In Stage A, stable baselines were obtained by rinsing the silica crystal with Buffer A. In Stage B, DOPC vesicles were deposited on the silica surface and they ruptured to form a SLB. In Stage C, the system was rinsed with Buffer A to remove unadsorbed vesicles. In Stage D, stable baselines were obtained by rinsing the SLB with a 0.6 mM  $\text{CaCl}_2$  and pH 7.2 solution. In Stage E, GO was deposited on the SLB in the same solution chemistry as used in Stage D.

The propensity for GO to attach to SLBs was investigated by exposing the SLBs to GO over a range of NaCl and  $\text{CaCl}_2$  concentrations. The deposition of GO on SLBs resulted in a negative frequency shift and a positive dissipation shift (Figure 2.3). The increase in

energy dissipation had also been reported during the deposition of carbon nanotubes<sup>31</sup> and quantum dots<sup>30</sup> on SLBs. The deposition rates of GO on DOPC SLBs are presented in Figure 2.4a and b. An increase in NaCl concentration from 10 to 100 mM resulted in a rise in GO deposition rates (Figure 2.4a). As the NaCl concentration was raised, the electric double layer (EDL) interaction between GO and SLBs was expected to become less repulsive due to the screening of the surface charges of both GO and SLBs, while the attractive dispersion force (i.e., the major component in van der Waals interactions) between them remained almost unchanged.<sup>49</sup> Therefore, the increase in NaCl concentration resulted in a rise in the propensity for GO to attach to DOPC SLBs. A further increase in NaCl concentration above 100 mM, however, led to a decrease in the deposition rates of GO. This decline in the deposition rates was likely due to the decrease in the diffusion coefficient of GO resulting from their aggregation at these high electrolyte concentrations, which was also reported in previous QCM-D studies on nanoparticle deposition.<sup>42, 50</sup>

Similar trends were observed when GO was deposited on DOPC SLBs in CaCl<sub>2</sub> solutions. Specifically, the rate of GO deposition increased when the CaCl<sub>2</sub> concentration was raised from 0.2 to 0.6 mM (Figure 2.4b). Calcium ions can bind to the carboxyl groups of GO<sup>39</sup> and the phosphate moieties in the headgroups of DOPC lipids,<sup>30</sup> thus resulting in the neutralization of the charges on GO and SLBs. Additionally, it was demonstrated in our earlier study<sup>31</sup> that the charge of DOPC was reversed at CaCl<sub>2</sub> concentrations higher than 0.5 mM. Within the range of CaCl<sub>2</sub> concentrations of 0.1–10 mM, GO remained negatively charged, as shown in Figure 2.2. Therefore, when the CaCl<sub>2</sub> concentration exceeded 0.5 mM, the EDL repulsion between GO and DOPC SLBs turned into attraction. Similar to the case of NaCl, a further increase in CaCl<sub>2</sub> concentration above 0.8 mM resulted in a decline in

the deposition rates owing to the concurrent aggregation of GO. Time-resolved DLS measurements verified that GO has the propensity to undergo aggregation at NaCl and CaCl<sub>2</sub> concentrations above 120 and 0.6 mM, respectively (Figure 2.5). It is thus also expected that GO may deposit on SLBs to form multilayer structures under elevated electrolyte concentrations.

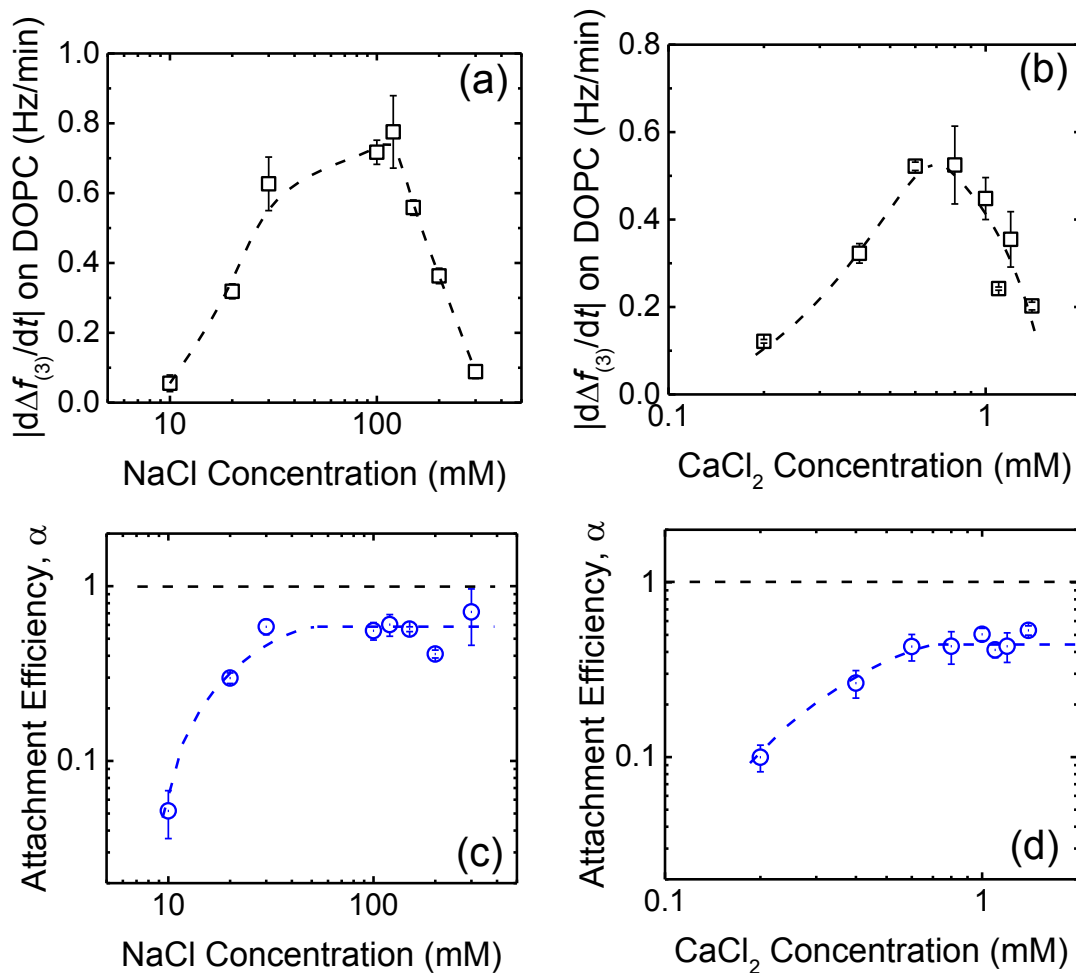


**Figure 2.4.** Deposition rates of GO on DOPC SLBs as functions of (a) NaCl and (b) CaCl<sub>2</sub> concentrations at pH 7.2. Attachment efficiencies of GO on DOPC SLBs as functions of (c) NaCl and (d) CaCl<sub>2</sub> concentrations at pH 7.2. Error bars represent standard deviations. The lines are meant to guide the eye.



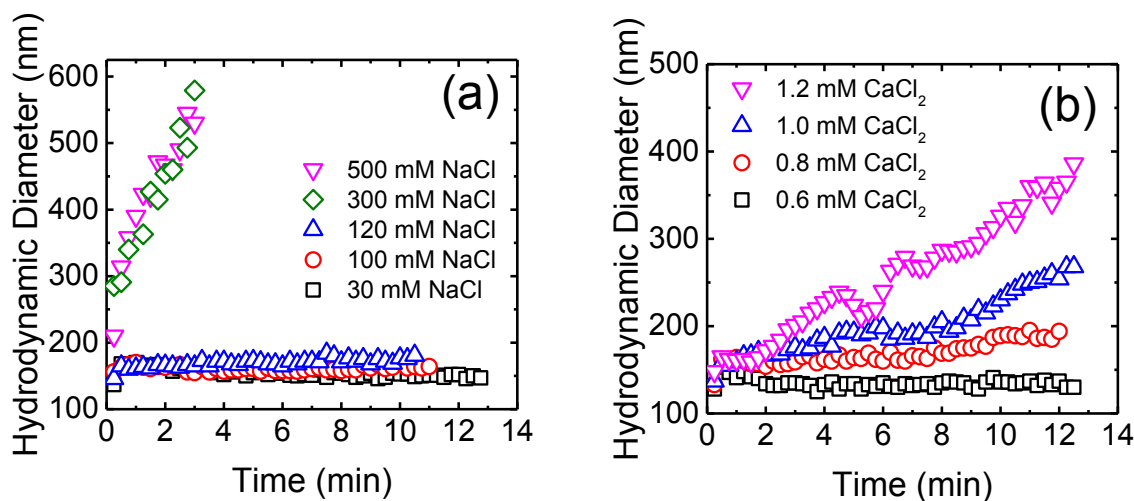


**Figure 2.5.** (a) Aggregation of GO in the presence of NaCl at pH 7.2. (b) Aggregation of GO in the presence of CaCl<sub>2</sub> at pH 7.2. The concentration of GO was 2.6 mg/L TOC.

By normalizing the deposition rates of GO on DOPC SLBs to the favorable deposition rates on PLL (Figure 2.6), the attachment efficiencies of GO on DOPC SLBs in NaCl and CaCl<sub>2</sub> can be calculated and are presented in Figure 2.4c and d, respectively. The attachment efficiencies increased with an increase in NaCl concentration within the range of 10–30 mM (slow regime). At NaCl concentrations higher than 30 mM, the attachment efficiency remained constant (fast regime). Similarly, slow and fast deposition regimes were observed in CaCl<sub>2</sub>. The CaCl<sub>2</sub> concentration that delineated the two regimes was ca. 0.6 mM, which is close to the CaCl<sub>2</sub> concentration at which the charge of DOPC SLBs is reversed (ca. 0.5 mM).<sup>31</sup> In the fast regimes, interestingly, the attachment efficiencies in NaCl and CaCl<sub>2</sub> were only  $0.57 \pm 0.10$  and  $0.46 \pm 0.05$ , respectively, both values lower than 1 which is expected if the interactions between GO and SLBs are controlled only by EDL repulsion and van der Waals attraction.<sup>51, 52</sup>

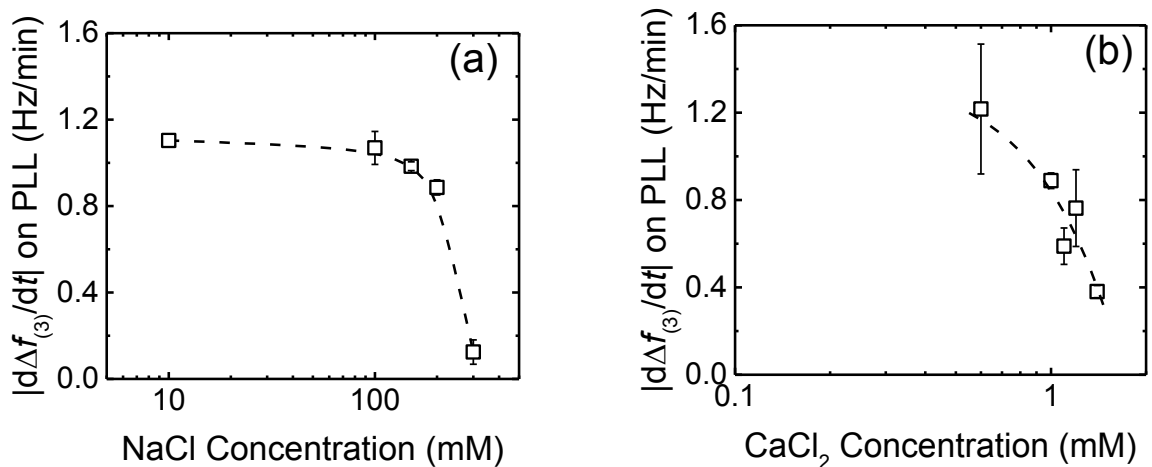


**Figure 2.6.** Deposition rates of GO on PLL-coated surfaces as functions of (a) NaCl and (b) CaCl<sub>2</sub> concentrations at pH 7.2. Error bars represent standard deviations. The lines are meant to guide the eye.

According to Derjaguin–Landau–Verwey–Overbeek (DLVO) theory,<sup>51, 52</sup> when the EDL repulsion is eliminated through charge screening at high electrolyte concentrations, favorable deposition will take place, resulting in an attachment efficiency of one.<sup>53</sup> Attachment efficiencies of lower-than-one, however, have been obtained for some systems, including the deposition of fullerene nanoparticles and bacteriophage MS2 on silica surfaces at high electrolyte concentrations.<sup>41, 54</sup> In addition, attachment efficiencies of smaller-than-one were measured for the deposition of multiwalled carbon nanotubes on DOPC SLBs at elevated NaCl concentrations.<sup>31</sup> Additional repulsive forces had been invoked in these studies<sup>31, 41, 54</sup> to account for the discrepancies between the observed attachment efficiencies and predictions based on DLVO theory. Hence, we speculate that non-DLVO repulsive

forces were also operative between GO and SLBs and contributed to the lower-than-one attachment efficiencies.

In order to test the existence of this repulsive force for positively charged SLBs, a DOPC–DOEPC SLB was used for the deposition of GO. The EPMs of DOPC–DOEPC vesicles were positive over the range of NaCl concentrations tested (i.e., 1–100 mM), as shown in Figure 2.7a. If only EDL and van der Waals attraction were regulating the interactions between GO and SLBs, an attachment efficiency of one would be expected over the entire range of NaCl concentrations. However, the attachment efficiencies of GO on DOPC–DOEPC SLBs were lower than 1 (ca. 0.3) over the entire range of NaCl concentrations (Figure 2.7b). This result demonstrated that the repulsive force was also existent between GO and positively charged lipid bilayers and that it can even “win out” over the sum of EDL and van der Waals attraction.

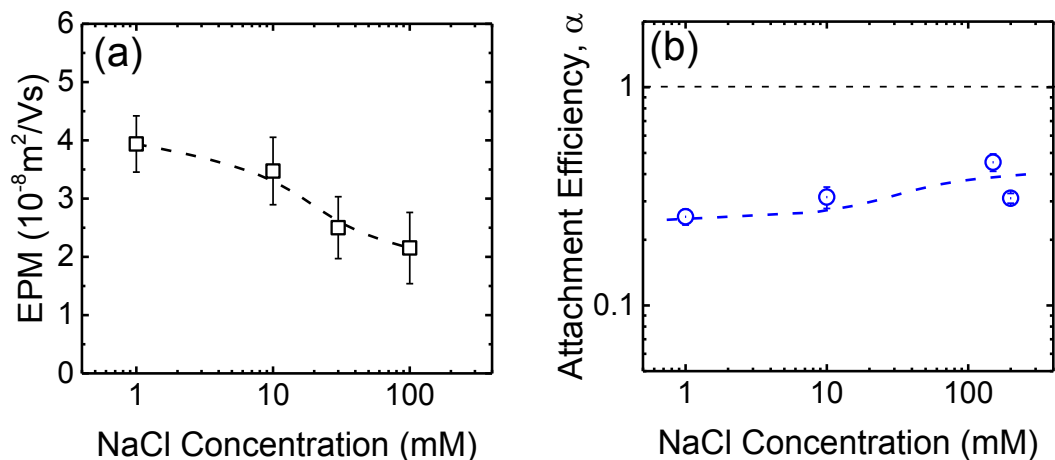


**Figure 2.7.** (a) EPMs of DOPC–DOEPC vesicles as a function of NaCl concentration at pH 7.2. (b) Attachment efficiencies of GO on positively charged DOPC–DOEPC SLBs as a function of NaCl concentration at pH 7.2. Error bars represent standard deviations. The lines are meant to guide the eye.

The headgroups of lipid bilayers are known to be highly hydrated.<sup>49</sup> NMR experiments on 1,2-dimyristoyl-*sn*-glycero-3-phosphocholine (DMPC) lipid bilayers have revealed the presence of a less mobile hydration shell of ca. 1–2 water molecules hydrogen-bonded to the oxygen in the phosphate and a more mobile hydration shell of ca. 5–6 hydrogen-bonded water molecules near the N(CH<sub>3</sub>) choline moiety.<sup>55</sup> Using frequency modulation atomic force microscopy, Fukuma et al.<sup>56</sup> observed oscillatory force profiles when an atomically sharp tip approached 1,2-dipalmitoyl-*sn*-glycero-3-phosphocholine (DPPC) lipid bilayers, thus demonstrating the presence of intrinsic hydration layers adjacent to the lipid bilayers. It is thus expected that repulsive hydration forces can be operative when a well-hydrated particle approaches a lipid surface. Using atomic force microscopy, Higgins et al.<sup>57</sup> observed the presence of an oscillatory repulsive force when a carbon nanotube approached a DPPC SLB, which was attributed to the removal of up to five structured water layers. Ahmed et al.<sup>58</sup> demonstrated that the formation of DMPC SLB on SiO<sub>2</sub> particles of

varying surface densities of silanol groups via the rupture of DMPC vesicles was slower for SiO<sub>2</sub> particles with higher silanol densities and thus more bound water. This observation indicates that hydration force was playing a crucial role in the interaction between SiO<sub>2</sub> particles and lipid vesicles. In light of these findings, hydration force was likely to be operative between GO and lipid bilayers.

GO contains abundant carboxyl, epoxy, and hydroxyl groups,<sup>7</sup> which are prone to hydration. When GO comes into close approach to lipid bilayers, the hydration layers adjacent to the functional groups on GO and the headgroups of lipid bilayers might overlap, bringing about repulsive entropic force between GO and lipid bilayers. This repulsive force may dominate van der Waals attraction and EDL interaction, especially at small separation distances, hence resulting in the lower than expected deposition kinetics of GO to SLBs. It is noteworthy that for real cell membranes that contain other components, such as lipopolysaccharides and proteins, additional steric or electrostatic forces induced by these components can potentially play a role in the interactions of GO with cell membranes.<sup>59-61</sup>

### **2.3.3 Reversibility of GO Deposition on DOPC SLBs**

After being attached on cell membranes, GO can elicit negative responses from bacterial (e.g., oxidation of cell components and inhibition of the proliferation of cells) and human cells (e.g., hemolysis of red blood cells).<sup>16,21</sup> The reversibility of GO deposition may have critical implications for the GO-induced cell responses, especially if the cell responses are dependent on the duration of GO–membrane contact. Figure 2.8 shows the change in frequency during the deposition of GO on a DOPC SLB in a 1.1 mM CaCl<sub>2</sub> solution (4–24 min), followed by the rinsing of the deposited GO with the same electrolyte solution (24–37 min) and then with DI water (37–55 min). For all stages, the pH was maintained constant at

7.2. At 1.1 mM  $\text{CaCl}_2$ , the DOPC SLB was positively charged and EDL attraction was expected to dominate between GO and DOPC SLBs. In DI water (or in the absence of  $\text{CaCl}_2$ ), however, the SLB became negatively charged, as shown in our earlier study,<sup>31</sup> thus resulting in EDL repulsion between the GO and SLBs.

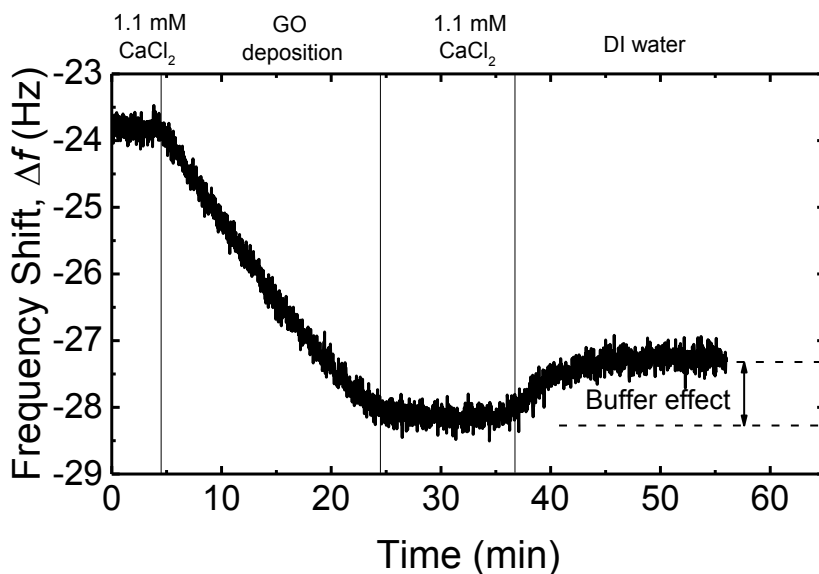


**Figure 2.8.** Frequency shifts during the deposition of GO on SLBs at 1.1 mM  $\text{CaCl}_2$  and rinsing of deposited GO with a 1.1 mM  $\text{CaCl}_2$  solution followed by DI water. The pH is maintained at 7.2 for the entire experiment.

At 1.1 mM  $\text{CaCl}_2$ , GO deposited on DOPC SLBs with an attachment efficiency of ca. 0.4 (Figure 2.4d). When the deposited GO was rinsed with a 1.1 mM  $\text{CaCl}_2$  solution, no frequency shift was observed, as shown in Figure 2.8, thus indicating that the deposited GO could not be released in the same solution chemistry. Following that, a positive frequency change of 0.8 Hz was observed when the deposited GO was rinsed with DI water. In a control experiment, the displacement of the 1.1 mM  $\text{CaCl}_2$  solution by DI water in the absence of deposited GO resulted in a similar frequency shift of 0.8 Hz since the change in solution density and viscosity can also result in a change in frequency.<sup>62, 63</sup> Taking this buffer effect<sup>62, 63</sup> into consideration, the exposure of the deposited GO to DI water did not

lead to any observable release of deposited GO from DOPC SLBs. This result indicates that the energy barrier for the release of the deposited GO was still insurmountable in DI water,<sup>64</sup> despite the transition from EDL attraction to repulsion between the deposited GO and SLB. The irreversibility of GO deposition on lipid membranes was also observed in another study<sup>17</sup> that showed that GO, after being adsorbed onto bacterial cell membranes, cannot be released even when the GO–bacteria suspension was subjected to ultrasonication.

#### **2.3.4 No Significant Rupture of Supported Vesicles when Exposed to GO**

A supported DOPC vesicular layer was used to investigate the rupture of vesicles upon the attachment of GO. Representative frequency and dissipation shifts during the formation of a SVL and the subsequent introduction of a GO suspension are presented in Figure 2.9. The SVL was first formed on a sensor by introducing a DOPC vesicle suspension into the QCM-D chamber.<sup>31, 40</sup> The large shifts in frequency and dissipation indicated that the vesicles had deposited on the sensor to form a SVL (75–154 min).<sup>40</sup> The deposited vesicles were then rinsed with Buffer A (154–215 min) followed by a 0.6 mM CaCl<sub>2</sub> solution (215–284 min). A GO suspension prepared in a 0.6 mM CaCl<sub>2</sub> solution was then introduced into the chambers (from 284 min onwards). This CaCl<sub>2</sub> concentration was selected because it corresponded to the onset of the fast deposition regime, as shown in Figure 2.4d. This calcium concentration is also representative of the concentrations in biological systems and natural aquatic systems with moderately hard water.<sup>65, 66</sup> With the continuous introduction of GO suspension, there was a negative frequency shift and a positive dissipation shift, indicating that GO was depositing on the supported vesicles. The negative frequency shift and concurrent positive dissipation shift also imply that no detectable rupture of vesicles took place upon the attachment of GO on the vesicles. In a positive control experiment performed

in our previous study,<sup>31</sup> the exposure of supported DOPC vesicles to a 32 mM Triton X-100 solution, a known membrane solubilizer, resulted in an instantaneous positive frequency shift and a concurrent negative dissipation shift resulting in final frequency and dissipation values of close to 0, which indicated that all the vesicles had ruptured instantaneously. Therefore, it was concluded from the results in Figure 2.9 that GO deposition did not induce the rupture of the supported DOPC vesicles.

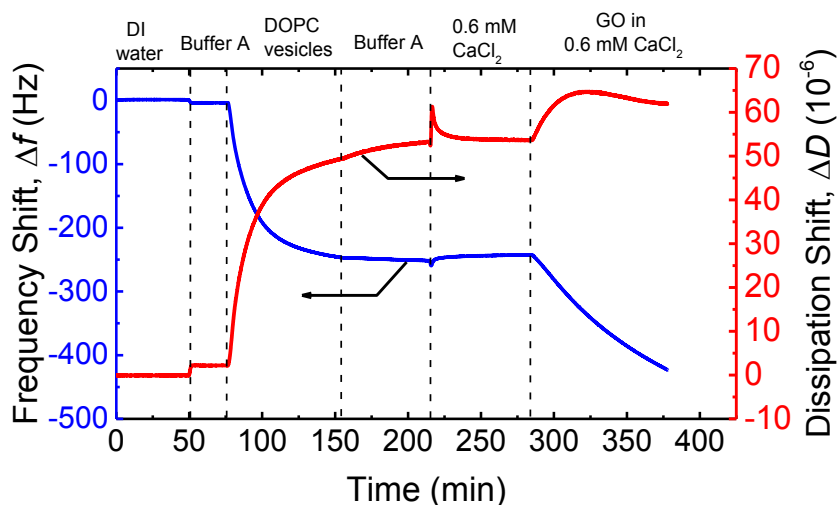


**Figure 2.9.** Frequency and dissipation shifts during the formation of a DOPC SVL and the deposition of GO on the SVL at 0.6 mM CaCl<sub>2</sub> and pH 7.2.

In the study of Frost et al.<sup>45</sup> on the interactions between GO and positively charged vesicles that were composed of 1-palmitoyl-2-oleyl-*sn*-glycero-3-phosphocholine (POPC) and 1-palmitoyl-2-oleyl-*sn*-glycero-3-ethylphosphocholine (POEPC), the supported POPC–POEPC vesicles were ruptured upon the attachment of GO. The authors attributed the rupture of the vesicles to the electrostatic attraction between GO and the bilayers. However, we did not observe significant rupture of positively charged DOPC–DOEPC vesicles upon



the attachment of GO (Figure 2.10). We speculate that the difference in membrane fluidity resulting from the different degrees of saturation of the fatty acid tails of the phospholipids,<sup>67</sup> as well as the difference in GO properties (e.g., flake size and density of surface functional groups), may account for the discrepancy between Frost et al.'s and our observations. Further investigation that involves a systematic variation in both the vesicle composition and GO properties is needed to fully elucidate their effects on the propensity for GO to rupture the vesicles.

### **2.3.5 Release of Fluorescent Dye from Supported DOPC Vesicles**

It has been reported that, after coming into attachment with cell membranes, GO may cause the destructive extraction of lipid from membranes.<sup>22</sup> This local damage of the lipid bilayers may not result in the complete rupture of cell membranes. Instead, it may lead to the formation of pores on membranes and hence the release of intracellular components,<sup>68</sup> which has been suggested to be a key mechanism for the cytotoxicity of nanoparticles.<sup>69</sup> To distinguish the complete rupture of vesicles from the local damage of vesicles that may not result in complete rupture, we use *disruption* from here on to refer to the latter process.

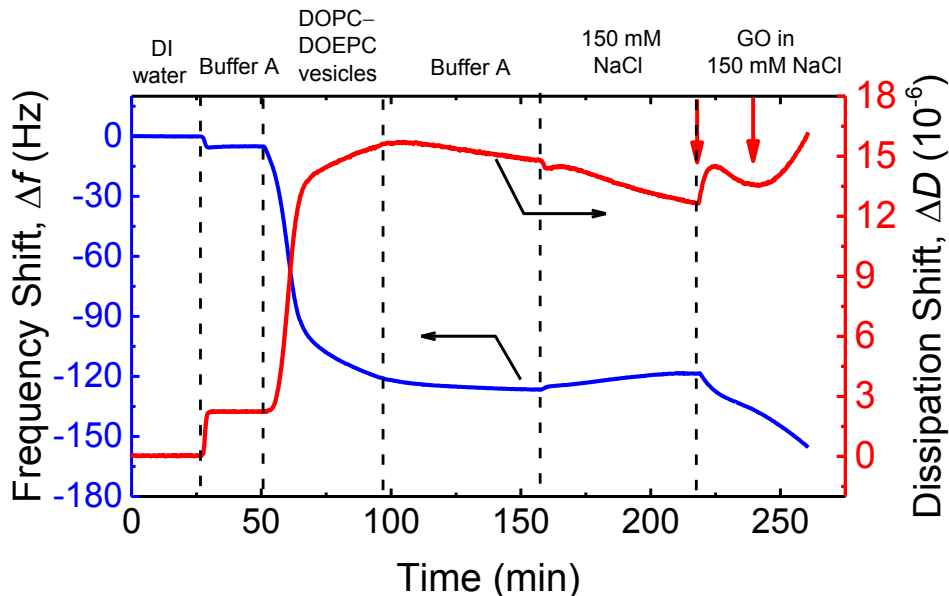
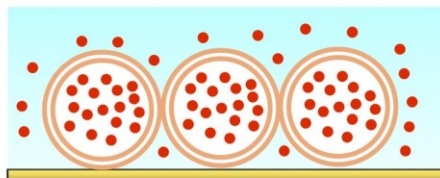


**Figure 2.10.** Frequency (blue) and dissipation (red) shifts during the formation of a DOPC–DOEPC SVL and the deposition of GO on the SVL at 150 mM NaCl and pH 7.2. The red arrows indicate the times at which two GO suspensions were successively prepared and introduced to the QCM-D chambers to allow for the deposition of GO on the SVL.

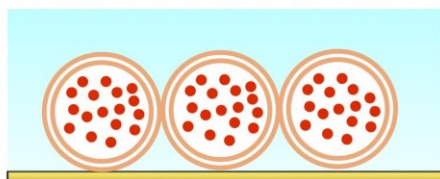
The fluorescent dye leakage technique has been proven to be a powerful tool for the study of the rupture and disruption of vesicles by nanoparticles and macromolecules (e.g., gold nanoparticles,<sup>28, 70</sup> humic acids,<sup>71</sup> and peptides<sup>72</sup>). Herein, the fluorescent dye leakage technique was coupled with QCM-D in order to monitor the leakage of vesicles and changes in the deposited mass simultaneously (scheme illustrated in Figure 2.11). This protocol involved three stages: deposition of fluorescent-dye encapsulated vesicles on gold-coated sensors (Stage A), removal of external dye by buffer rinse (Stage B), and exposure of the supported vesicles to GO suspension (Stage C). The NaCl concentration inside the supported vesicles was 150 mM, which is close to the ionic strength in biological fluids.<sup>26</sup> The frequency and dissipation shifts of the sensors, as well as the fluorescence intensity of the outflow, were monitored simultaneously throughout the experiment. At the end of each

experiment, the supported vesicles were exposed to a 32 mM Triton X-100 solution to induce the complete rupture of the vesicles. In a typical experiment, four QCM-D chambers were used in parallel. In two of the chambers, GO suspensions were introduced into the chambers to allow for the deposition of GO onto the supported vesicles. In the other two chambers, as a negative control, the supported vesicles were exposed to electrolyte solutions of the same solution chemistry in the absence of GO. Three solution chemistries were employed in preparing the GO suspensions: 150 mM NaCl and 0.6 mM CaCl<sub>2</sub>, both allowing for the fast deposition of GO to lipid bilayers, and 1 mM NaCl, at which GO underwent slow deposition on the bilayers (as shown in Figure 2.4c and d).

(A) Deposit a layer of supported vesicles on Au



(B) Rinse with buffer to remove external dye



(C) Introduce GO

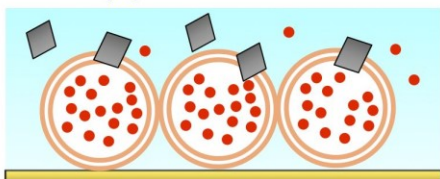


**Figure 2.11.** Schematic of dye leakage detection coupled with QCM-D. Note that GO and vesicles are not drawn to scale.

Figure 2.12a shows the frequency and dissipation response during the deposition of GO on the supported DOPC vesicles at 150 mM NaCl and Figure 2.12b shows the release of dye from the vesicles in the presence and in the absence of GO. Figure 2.12c shows a close-up of the dye release during the GO deposition and rinsing stages. Before the introduction of the GO suspension, the dye outside the supported vesicles was removed by rinsing with Buffer C followed by a 150 mM NaCl solution. When the GO suspension was introduced into the chambers (58 to 105 min), the GO deposited on the SVL, as evident from the considerable decrease in frequency response (Figure 2.12a). The decrease in the frequency response also indicated that no significant rupture of deposited vesicles occurred upon GO attachment. While GO deposition took place on the SVL, the dye concentration was also observed to be significantly higher than that in the absence of GO (Figure 2.12b and c), indicating that the attachment of GO resulted in the release of some dye from inside the vesicles. Since the lipid bilayers are impermeable barriers to CF, the release of dye implies that some pores had formed on the vesicles such that the dye molecules were able to diffuse through the lipid bilayers. This local disruption of the vesicles was not severe enough to induce the rupture of the vesicles. The disruption of model cell membranes by GO is consistent with the findings of other studies that have reported the release of RNA from *Escherichia coli* caused by the direct contact with the sharp edges of GO nanowalls<sup>18</sup> and the leakage of intracellular contents from dental pathogens when exposed to GO.<sup>73</sup>

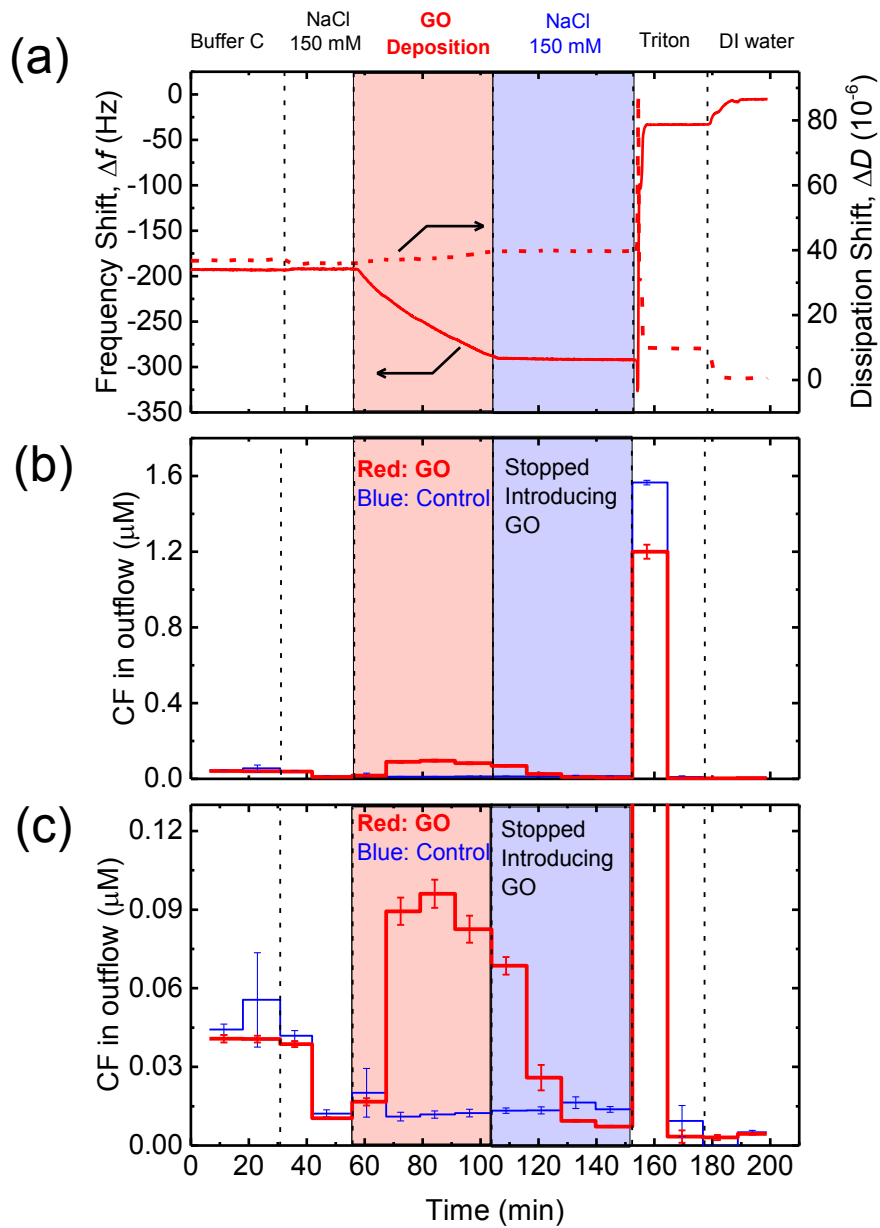


**Figure 2.12.** (a) Frequency and dissipation shifts when supported DOPC vesicles were exposed to GO suspension in 150 mM NaCl (shaded in red), 150 mM NaCl solution (shaded in blue), and 32 mM Triton X-100. The solid and dash lines show the frequency and dissipation shifts, respectively. (b) Release of CF dye from supported vesicles upon exposure to GO suspension (in 150 mM NaCl), 150 mM NaCl solution, and 32 mM Triton X-100. The red and blue lines show the release of dye in the GO deposition and control experiments, respectively. (c) Close-up of the release of dye in the GO deposition and rinsing stages, both at 150 mM NaCl. Error bars represent standard deviations.

Following the deposition of GO, the supported vesicles were rinsed with Triton X-100 (153 to 178 min) and significant dye release was observed as the deposited vesicles were solubilized by the surfactant (Figure 2.12b). It is noted that the amount of dye released upon exposure to Triton was significantly lower for the vesicles that were pre-exposed to a GO suspension since some dye had earlier been released during GO exposure. It is noteworthy that the vesicles ruptured instantaneously upon the exposure to Triton, as shown by the abrupt frequency and dissipation shifts at 153 min in Figure 2.12a. By this token, the disruption of cell membranes by GO was much less severe than that by the surfactant in terms of the extent and speed of disruption.

After GO had deposited on the SVL for 40 min, the GO suspension was replaced by a 150 mM NaCl solution at 104 min and the dye concentration dropped to background level within 20 min from the switch in solutions (Figure 2.12c). The almost complete reduction in dye release suggests that the pores on vesicles that were formed during the deposition of GO were transient and could “heal” in the absence of GO in the background solution. Although GO can cause perturbation of lipid membranes, the model membranes seemed to possess the ability to “repair” this local disruption. It is interesting to note that this “self-repairing” can take place even when the GO nanosheets were still attached to the membranes, as indicated by the stable frequency response during this NaCl rinsing stage (105–153 min, Figure 2.12a).

Vesicles deposited on a surface are subjected to membrane tension due to the restriction of thermal fluctuation of the lipid membrane.<sup>74, 75</sup> The sharp corners of GO, as shown by molecular simulation, can induce pores on lipid bilayers,<sup>23, 76</sup> consistent with our experimental observations. The growth (or shrinkage) of the pores is controlled by two opposing forces — membrane tension which is the driving force for pore opening and line

tension (or the excess free energy per unit length of the pore edge) which is the driving force for pore closure.<sup>49, 75, 77, 78</sup> Two mechanisms can come into play simultaneously to inhibit the further growth of the pores and eventually result in their closure.<sup>75, 79</sup> First, the formation of pores will allow for the lipid to be distributed over a smaller area, thereby leading to a relaxation of the membrane tension.<sup>79</sup> Additionally, the leaking of internal fluid from the vesicles due to the excess Laplace pressure<sup>75, 79</sup> will result in the shrinkage of the vesicles and hence a reduction in the membrane tension.<sup>79</sup> As the membrane tension decreases, line tension begins to dominate, hence driving the closure of the pores.<sup>79</sup> It was likely that these two mechanisms contributed to the “self-healing” of the pores when the exposure of the SVL to the GO suspension was terminated. In another study, Wong-Ekkabut et al.<sup>80</sup> performed computer simulations of the translocation of fullerene nanoparticles through lipid membranes and also reported transient distortion of the membranes. To the best of our knowledge, this study is the first to provide experimental evidence on the transient disruption of lipid membranes upon the attachment of GO.

Additionally, a similar deposition experiment was conducted with a suspension of GO prepared in 0.6 mM CaCl<sub>2</sub> (Figure 2.13). When a supported vesicular layer was rinsed with a 0.6 mM CaCl<sub>2</sub> solution, a considerable amount of dye was released from the vesicles, which is likely due to the rupture-promoting ability of Ca<sup>2+</sup> ions.<sup>35, 81</sup> Even though some dye was released in this CaCl<sub>2</sub> rinsing stage, the release of dye that resulted from the subsequent deposition of GO was still evidently higher compared to that in the control experiment, similar to the observation at 150 mM NaCl.

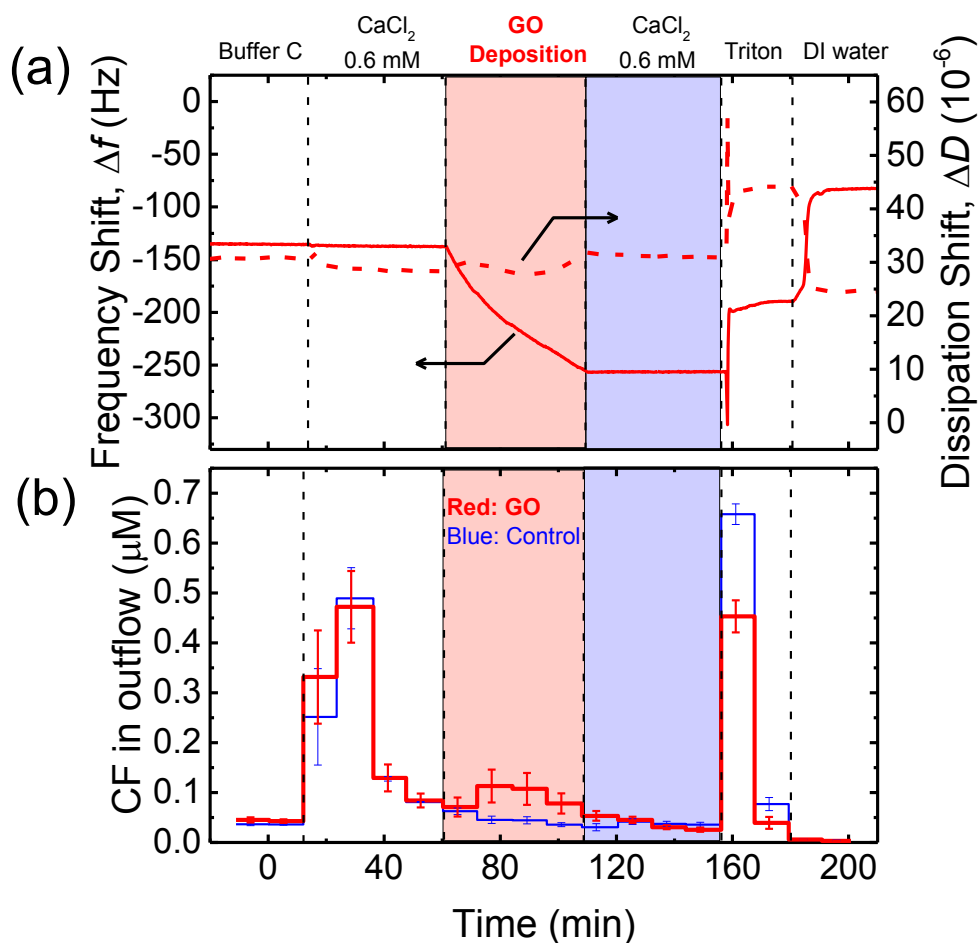


**Figure 2.13.** (a) Frequency and dissipation shifts when supported DOPC vesicles were exposed to GO suspension in 0.6 mM CaCl<sub>2</sub> (shaded in red), 0.6 mM CaCl<sub>2</sub> solution (shaded in blue), and 32 mM Triton X-100. The solid and dash lines show the frequency and dissipation shifts, respectively. (b) Release of CF dye from supported vesicles when the vesicles were exposed to GO suspension (in 0.6 mM CaCl<sub>2</sub>), 0.6 mM CaCl<sub>2</sub> solution, and 32 mM Triton X-100. The red and blue lines show the dye release profiles in the GO deposition and control experiments, respectively. Error bars represent standard deviations.

Finally, the deposition experiment was conducted at 1 mM NaCl (Figure 2.14), at which the attachment efficiency of GO on DOPC SLBs was below 0.05 (Figure 2.4c). When Buffer C was replaced by a 1 mM NaCl solution at 34 min, the frequency shift increased (Figure 2.14a) while the dye concentration of the outflow increased from 0.03 to 0.60  $\mu\text{M}$  (Figure 2.14b), indicating that some of the supported vesicles were disrupted with the switch in background solutions. The disruption of vesicles was attributed to the sudden generation



of an osmotic pressure across the lipid bilayer of vesicles with the dramatic drop in NaCl concentration (150 mM in Buffer C to 1 mM) and this osmotic-triggered disruption of vesicles was also observed in other studies.<sup>82, 83</sup>

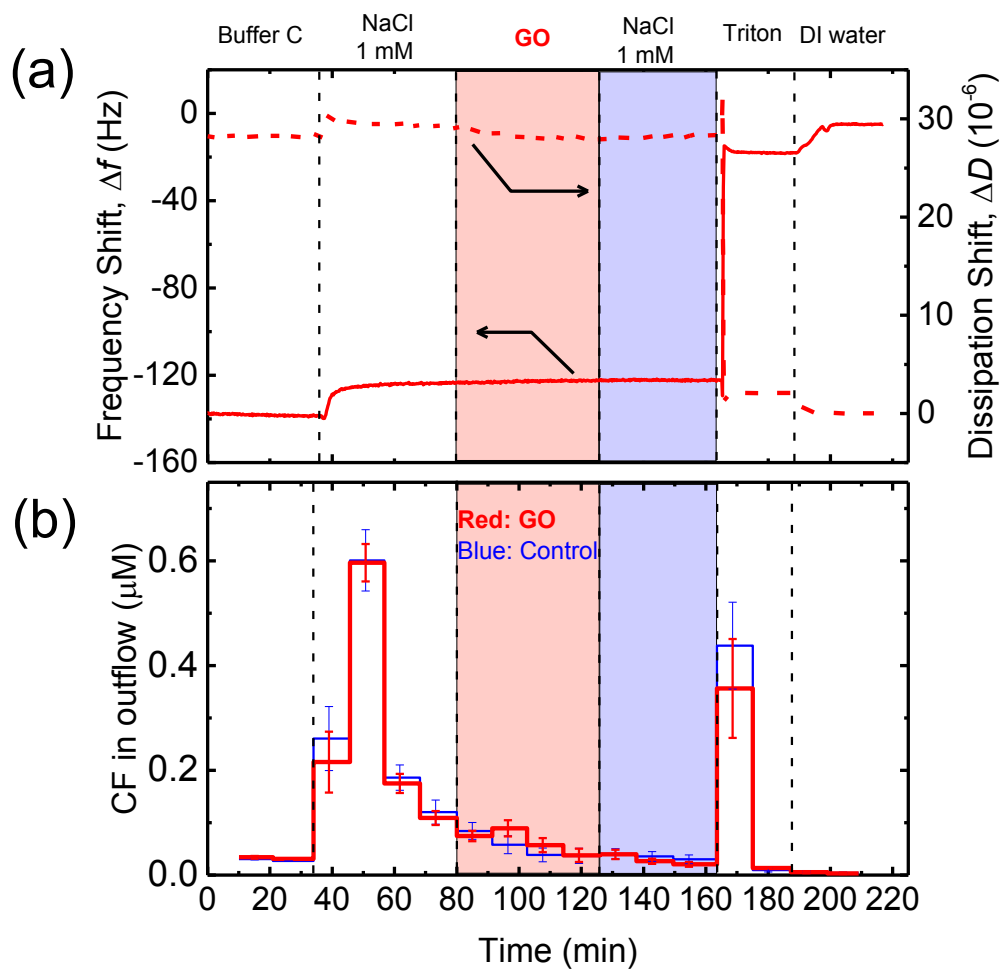


**Figure 2.14.** (a) Frequency and dissipation shifts when supported DOPC vesicles were exposed to GO suspension in 1 mM NaCl (shaded in red), 1 mM NaCl solution (shaded in blue), and 32 mM Triton X-100. The solid and dash lines show the frequency and dissipation shifts, respectively. (b) Release of CF dye from supported vesicles upon exposure to GO suspension (in 1 mM NaCl), 1 mM NaCl solution, and 32 mM Triton X-100. The red and blue lines show the release of dye in the GO deposition and control experiments, respectively. Error bars represent standard deviations.

Upon the introduction of the GO suspension (80–125 min), the QCM-D frequency and dissipation response remained constant (Figure 2.14a) because the conditions for GO deposition on DOPC vesicles were unfavorable. Meanwhile, the fluorescent dye concentrations of the QCM-D outflow in the GO deposition and control experiments (Figure 2.14b) were not significantly different (two-tailed *t* test, significance level of 0.05). This observation further verified that the deposition of GO on the surface of vesicles is vital to induce further penetration or creation of pores in the lipid bilayers. When the attachment of GO on lipid bilayers was inhibited by strong EDL repulsion, the disruption of lipid vesicles can be alleviated to a large extent. Thus, the effect of solution chemistry in the specific environments where the GO–cell membrane interactions take place should be accounted for during the assessment of the cytotoxicity of GO.

## 2.4 Conclusions

In this study, the influence of NaCl and CaCl<sub>2</sub> concentrations on the propensity of GO to attach on model cell membranes is investigated. Since both GO and SLB are negatively charged under neutral pH conditions, the rise in NaCl concentration results in the reduction of electrostatic repulsion and thus in an increase in the GO deposition kinetics. In the presence of CaCl<sub>2</sub>, Ca<sup>2+</sup> ions can bind to the headgroups of DOPC and neutralize or reverse the charge of the SLBs, hence allowing for fast GO deposition. At elevated NaCl or CaCl<sub>2</sub> concentrations, however, mass-transfer-limited deposition kinetics were not achieved, which was attributed to the existence of repulsive hydration forces between GO and SLBs. No release of GO from the SLBs was observed upon elution with DI water, indicating that the attachment of GO was largely irreversible. When GO deposited on the SVLs under

favorable conditions, no rupture of the deposited vesicles was observed. Instead, dye leakage from inside the vesicles was detected, indicating the formation of pores on the vesicles. The leakage of dye decreased significantly upon the termination of exposure to GO suspension, demonstrating the self-healing ability of the membranes. Additionally, dye leakage was not observed under unfavorable deposition conditions, further verifying that the attachment of GO was a necessary step for the disruption of lipid membranes.

## 2.5 References

1. Novoselov, K. S.; Geim, A. K.; Morozov, S. V.; Jiang, D.; Zhang, Y.; Dubonos, S. V.; Grigorieva, I. V.; Firsov, A. A., Electric field effect in atomically thin carbon films. *Science* **2004**, *306*, (5696), 666-9.
2. Geim, A. K.; Novoselov, K. S., The rise of graphene. *Nat. Mater.* **2007**, *6*, (3), 183-191.
3. Castro Neto, A. H.; Guinea, F.; Peres, N. M. R.; Novoselov, K. S.; Geim, A. K., The electronic properties of graphene. *Reviews of Modern Physics* **2009**, *81*, (1), 109-162.
4. Avouris, P., Graphene: Electronic and Photonic Properties and Devices. *Nano Lett.* **2010**, *10*, (11), 4285-4294.
5. Balandin, A. A., Thermal properties of graphene and nanostructured carbon materials. *Nat. Mater.* **2011**, *10*, (8), 569-581.
6. Lee, C.; Wei, X. D.; Kysar, J. W.; Hone, J., Measurement of the elastic properties and intrinsic strength of monolayer graphene. *Science* **2008**, *321*, (5887), 385-388.
7. Dreyer, D. R.; Park, S.; Bielawski, C. W.; Ruoff, R. S., The chemistry of graphene oxide. *Chemical Society reviews* **2010**, *39*, (1), 228-240.
8. Stankovich, S.; Dikin, D. A.; Piner, R. D.; Kohlhaas, K. A.; Kleinhammes, A.; Jia, Y.; Wu, Y.; Nguyen, S. T.; Ruoff, R. S., Synthesis of graphene-based nanosheets via chemical reduction of exfoliated graphite oxide. *Carbon* **2007**, *45*, (7), 1558-1565.
9. Sun, X. M.; Liu, Z.; Welsher, K.; Robinson, J. T.; Goodwin, A.; Zaric, S.; Dai, H. J., Nano-Graphene Oxide for Cellular Imaging and Drug Delivery. *Nano Res* **2008**, *1*, (3), 203-212.
10. Zhang, L. M.; Xia, J. G.; Zhao, Q. H.; Liu, L. W.; Zhang, Z. J., Functional Graphene Oxide as a Nanocarrier for Controlled Loading and Targeted Delivery of Mixed Anticancer Drugs. *Small* **2010**, *6*, (4), 537-544.
11. Perreault, F.; Fonseca de Faria, A.; Elimelech, M., Environmental applications of graphene-based nanomaterials. *Chem. Soc. Rev.* **2015**, *44*, (16), 5861-96.
12. Hu, M.; Mi, B. X., Enabling Graphene Oxide Nanosheets as Water Separation Membranes. *Environ. Sci. Technol.* **2013**, *47*, (8), 3715-3723.

13. Li, H.; Song, Z. N.; Zhang, X. J.; Huang, Y.; Li, S. G.; Mao, Y. T.; Ploehn, H. J.; Bao, Y.; Yu, M., Ultrathin, Molecular-Sieving Graphene Oxide Membranes for Selective Hydrogen Separation. *Science* **2013**, *342*, (6154), 95-98.
14. Perreault, F.; Tousley, M. E.; Elimelech, M., Thin-Film Composite Polyamide Membranes Functionalized with Biocidal Graphene Oxide Nanosheets. *Environmental Science & Technology Letters* **2013**, *1*, (1), 71-76.
15. Jiang, Y.; Wang, W.; Liu, D.; Nie, Y.; Li, W.; Wu, J.; Zhang, F.; Biswas, P.; Fortner, J. D., Engineered Crumpled Graphene Oxide Nanocomposite Membrane Assemblies for Advanced Water Treatment Processes. *Environ Sci Technol* **2015**, *49*, 6846-6854.
16. Liu, S. B.; Zeng, T. H.; Hofmann, M.; Burcombe, E.; Wei, J.; Jiang, R. R.; Kong, J.; Chen, Y., Antibacterial Activity of Graphite, Graphite Oxide, Graphene Oxide, and Reduced Graphene Oxide: Membrane and Oxidative Stress. *ACS Nano* **2011**, *5*, (9), 6971-6980.
17. Liu, S.; Hu, M.; Zeng, T. H.; Wu, R.; Jiang, R.; Wei, J.; Wang, L.; Kong, J.; Chen, Y., Lateral dimension-dependent antibacterial activity of graphene oxide sheets. *Langmuir* **2012**, *28*, (33), 12364-72.
18. Akhavan, O.; Ghaderi, E., Toxicity of Graphene and Graphene Oxide Nanowalls Against Bacteria. *ACS Nano* **2010**, *4*, (10), 5731-5736.
19. Zhao, J.; Wang, Z. Y.; White, J. C.; Xing, B. S., Graphene in the Aquatic Environment: Adsorption, Dispersion, Toxicity and Transformation. *Environmental Science & Technology* **2014**, *48*, (17), 9995-10009.
20. Chang, Y. L.; Yang, S. T.; Liu, J. H.; Dong, E.; Wang, Y. W.; Cao, A. N.; Liu, Y. F.; Wang, H. F., In vitro toxicity evaluation of graphene oxide on A549 cells. *Toxicol. Lett.* **2011**, *200*, (3), 201-210.
21. Liao, K. H.; Lin, Y. S.; Macosko, C. W.; Haynes, C. L., Cytotoxicity of Graphene Oxide and Graphene in Human Erythrocytes and Skin Fibroblasts. *ACS Appl. Mater. Interfaces* **2011**, *3*, (7), 2607-2615.
22. Tu, Y. S.; Lv, M.; Xiu, P.; Huynh, T.; Zhang, M.; Castelli, M.; Liu, Z. R.; Huang, Q.; Fan, C. H.; Fang, H. P.; Zhou, R. H., Destructive extraction of phospholipids from Escherichia coli membranes by graphene nanosheets. *Nat. Nanotechnol.* **2013**, *8*, (12), 594-601.
23. Li, Y.; Yuan, H.; von dem Bussche, A.; Creighton, M.; Hurt, R. H.; Kane, A. B.; Gao, H., Graphene microsheets enter cells through spontaneous membrane penetration at edge asperities and corner sites. *Proc. Natl. Acad. Sci. U. S. A.* **2013**, *110*, (30), 12295-300.
24. Yi, X.; Gao, H. J., Cell interaction with graphene microsheets: near-orthogonal cutting versus parallel attachment. *Nanoscale* **2015**, *7*, (12), 5457-5467.
25. Chen, K. L.; Bothun, G. D., Nanoparticles Meet Cell Membranes: Probing Nonspecific Interactions. using Model Membranes. *Environ. Sci. Technol.* **2014**, *48*, (2), 873-880.
26. Nel, A. E.; Madler, L.; Velegol, D.; Xia, T.; Hoek, E. M. V.; Somasundaran, P.; Klaessig, F.; Castranova, V.; Thompson, M., Understanding biophysicochemical interactions at the nano-bio interface. *Nat. Mater.* **2009**, *8*, (7), 543-557.
27. Lu, B.; Smith, T.; Li, R. B.; Xia, T.; Nel, A.; Schmidt, J., Nanoparticle-Membrane Interactions Studied with Lipid Bilayer Arrays. *Biophys J* **2014**, *106*, (2), 415a-415a.
28. Moghadam, B. Y.; Hou, W. C.; Corredor, C.; Westerhoff, P.; Posner, J. D., Role of nanoparticle surface functionality in the disruption of model cell membranes. *Langmuir* **2012**, *28*, (47), 16318-26.

29. Lesniak, A.; Salvati, A.; Santos-Martinez, M. J.; Radomski, M. W.; Dawson, K. A.; Aberg, C., Nanoparticle adhesion to the cell membrane and its effect on nanoparticle uptake efficiency. *J. Am. Chem. Soc.* **2013**, *135*, (4), 1438-44.
30. Zhang, X. F.; Yang, S. H., Nonspecific Adsorption of Charged Quantum Dots on Supported Zwitterionic Lipid Bilayers: Real-Time Monitoring by Quartz Crystal Microbalance with Dissipation. *Langmuir* **2011**, *27*, (6), 2528-2535.
31. Yi, P.; Chen, K. L., Interaction of Multiwalled Carbon Nanotubes with Supported Lipid Bilayers and Vesicles as Model Biological Membranes. *Environ Sci Technol* **2013**, *47*, (11), 5711-5719.
32. Akhavan, O.; Ghaderi, E.; Esfandiari, A., Wrapping Bacteria by Graphene Nanosheets for Isolation from Environment, Reactivation by Sonication, and Inactivation by Near-Infrared Irradiation. *J. Phys. Chem. B* **2011**, *115*, (19), 6279-6288.
33. Ip, A. C.; Liu, B.; Huang, P. J.; Liu, J., Oxidation level-dependent zwitterionic liposome adsorption and rupture by graphene-based materials and light-induced content release. *Small* **2013**, *9*, (7), 1030-5.
34. Wang, F.; Liu, J., Nanodiamond decorated liposomes as highly biocompatible delivery vehicles and a comparison with carbon nanotubes and graphene oxide. *Nanoscale* **2013**.
35. Cho, N. J.; Frank, C. W.; Kasemo, B.; Hook, F., Quartz crystal microbalance with dissipation monitoring of supported lipid bilayers on various substrates. *Nat. Protoc.* **2010**, *5*, (6), 1096-106.
36. Huynh, K. A.; Chen, K. L., Aggregation kinetics of citrate and polyvinylpyrrolidone coated silver nanoparticles in monovalent and divalent electrolyte solutions. *Environ. Sci. Technol.* **2011**, *45*, (13), 5564-71.
37. Hook, F.; Kasemo, B.; Nylander, T.; Fant, C.; Sott, K.; Elwing, H., Variations in coupled water, viscoelastic properties, and film thickness of a Mefp-1 protein film during adsorption and cross-linking: A quartz crystal microbalance with dissipation monitoring, ellipsometry, and surface plasmon resonance study. *Anal. Chem.* **2001**, *73*, (24), 5796-5804.
38. Yi, P.; Chen, K. L., Influence of surface oxidation on the aggregation and deposition kinetics of multiwalled carbon nanotubes in monovalent and divalent electrolytes. *Langmuir* **2011**, *27*, (7), 3588-99.
39. Chowdhury, I.; Duch, M. C.; Mansukhani, N. D.; Hersam, M. C.; Bouchard, D., Deposition and Release of Graphene Oxide Nanomaterials Using a Quartz Crystal Microbalance. *Environ. Sci. Technol.* **2014**, *48*, (2), 961-969.
40. Keller, C. A.; Kasemo, B., Surface specific kinetics of lipid vesicle adsorption measured with a quartz crystal microbalance. *Biophys. J.* **1998**, *75*, (3), 1397-1402.
41. Qu, X. L.; Alvarez, P. J. J.; Li, Q. L., Impact of Sunlight and Humic Acid on the Deposition Kinetics of Aqueous Fullerene Nanoparticles (nC(60)). *Environ. Sci. Technol.* **2012**, *46*, (24), 13455-13462.
42. Chen, K. L.; Elimelech, M., Interaction of Fullerene (C-60) Nanoparticles with Humic Acid and Alginate Coated Silica Surfaces: Measurements, Mechanisms, and Environmental Implications. *Environ. Sci. Technol.* **2008**, *42*, (20), 7607-7614.
43. Elimelech, M. G., J.; Jia, X.; Williams, R. A., *Particle Deposition and Aggregation: Measurement, Modelling and Simulation*. Butterworth-Heinemann: Oxford: England, 1995.

44. de Kerchove, A. J.; Elimelech, M., Structural growth and viscoelastic properties of adsorbed alginate layers in monovalent and divalent salts. *Macromolecules* **2006**, *39*, (19), 6558-6564.
45. Frost, R.; Jonsson, G. E.; Chakarov, D.; Svedhem, S.; Kasemo, B., Graphene Oxide and Lipid Membranes: Interactions and Nanocomposite Structures. *Nano Lett.* **2012**, *12*, (7), 3356-3362.
46. Saleh, N. B.; Pfefferle, L. D.; Elimelech, M., Aggregation Kinetics of Multiwalled Carbon Nanotubes in Aquatic Systems: Measurements and Environmental Implications. *Environ. Sci. Technol.* **2008**, *42*, (21), 7963-7969.
47. Richter, R.; Mukhopadhyay, A.; Brisson, A., Pathways of lipid vesicle deposition on solid surfaces: A combined QCM-D and AFM study. *Biophys. J.* **2003**, *85*, (5), 3035-3047.
48. Richter, R. P.; Berat, R.; Brisson, A. R., Formation of solid-supported lipid bilayers: An integrated view. *Langmuir* **2006**, *22*, (8), 3497-3505.
49. Israelachvili, J. N., *Intermolecular and surface forces: revised third edition*. Academic press: 2011.
50. Chen, K. L.; Elimelech, M., Aggregation and deposition kinetics of fullerene (C-60) nanoparticles. *Langmuir* **2006**, *22*, (26), 10994-11001.
51. Verwey, E. J. W., Theory of the Stability of Lyophobic Colloids. *Philips Research Reports* **1945**, *1*, (1), 33-49.
52. Derjaguin, B. V.; Landau, L. D., Theory of the Stability of Strongly Charged Lyophobic Sols and of the Adhesion of Strongly Charged-Particles in Solutions of Electrolytes. *Acta Physicochim. URSS* **1941**, *14*, 633-662.
53. Trefalt, G.; Ruiz-Cabello, F. J. M.; Borkovec, M., Interaction Forces, Heteroaggregation, and Deposition Involving Charged Colloidal Particles. *J. Phys. Chem. B* **2014**, *118*, (23), 6346-6355.
54. Yuan, B. L.; Pham, M.; Nguyen, T. H., Deposition Kinetics of Bacteriophage MS2 on a Silica Surface Coated with Natural Organic Matter in a Radial Stagnation Point Flow Cell. *Environ. Sci. Technol.* **2008**, *42*, (20), 7628-7633.
55. Hsieh, C. H.; Wu, W. G., Structure and dynamics of primary hydration shell of phosphatidylcholine bilayers at subzero temperatures. *Biophys. J.* **1996**, *71*, (6), 3278-3287.
56. Fukuma, T.; Higgins, M. J.; Jarvis, S. P., Direct imaging of individual intrinsic hydration layers on lipid bilayers at Angstrom resolution. *Biophys. J.* **2007**, *92*, (10), 3603-3609.
57. Higgins, M. J.; Polcik, M.; Fukuma, T.; Sader, J. E.; Nakayama, Y.; Jarvis, S. P., Structured water layers adjacent to biological membranes. *Biophys. J.* **2006**, *91*, (7), 2532-2542.
58. Ahmed, S.; Madathingal, R. R.; Wunder, S. L.; Chen, Y. J.; Bothun, G., Hydration repulsion effects on the formation of supported lipid bilayers. *Soft Matter* **2011**, *7*, (5), 1936-1947.
59. Romero-Vargas Castrillón, S.; Perreault, F.; de Faria, A. F.; Elimelech, M., Interaction of Graphene Oxide with Bacterial Cell Membranes: Insights from Force Spectroscopy. *Environ. Sci. Technol. Lett.* **2015**, *2*, (4), 112-117.
60. Huang, R. X.; Carney, R. R.; Ikuma, K.; Stellacci, F.; Lau, B. L. T., Effects of Surface Compositional and Structural Heterogeneity on Nanoparticle-Protein Interactions: Different Protein Configurations. *ACS Nano* **2014**, *8*, (6), 5402-5412.

61. Jacobson, K. H.; Gunsolus, I. L.; Kuech, T. R.; Troiano, J. M.; Melby, E. S.; Lohse, S. E.; Hu, D.; Chrisler, W. B.; Murphy, C. J.; Orr, G.; Geiger, F. M.; Haynes, C. L.; Pedersen, J. A., Lipopolysaccharide density and structure governs the extent and distance of nanoparticle interaction with actual and model bacterial outer membranes. *Environ. Sci. Technol.* **2015**, *49*, (17), 10642-10650.
62. Peh, W. Y. X.; Reimhult, E.; Teh, H. F.; Thomsen, J. S.; Su, X. D., Understanding ligand binding effects on the conformation of estrogen receptor alpha-DNA complexes: A combinational quartz crystal microbalance with dissipation and surface plasmon resonance study. *Biophys. J.* **2007**, *92*, (12), 4415-4423.
63. Yi, P.; Chen, K. L., Influence of Solution Chemistry on the Release of Multiwalled Carbon Nanotubes from Silica Surfaces. *Environ. Sci. Technol.* **2013**, *47*, (21), 12211-12218.
64. Ruckenstein, E.; Prieve, D. C., Adsorption and Desorption of Particles and Their Chromatographic-Separation. *AIChE J.* **1976**, *22*, (2), 276-283.
65. McLean, F. C.; Hastings, A. B., The state of calcium in the fluids of the body I. The conditions affecting the ionization of calcium. *J. Biol. Chem.* **1935**, *108*, (1), 285-321.
66. Livingstone, D. A., *Chemical composition of rivers and lakes*. US Government Printing Office: 1963.
67. Maherani, B.; Arab-Tehrany, E.; Kheirilomoom, A.; Cleymand, F.; Linder, M., Influence of lipid composition on physicochemical properties of nanoliposomes encapsulating natural dipeptide antioxidant L-carnosine. *Food Chem.* **2012**, *134*, (2), 632-640.
68. Zhang, Y. B.; Ali, S. F.; Dervishi, E.; Xu, Y.; Li, Z. R.; Casciano, D.; Biris, A. S., Cytotoxicity Effects of Graphene and Single-Wall Carbon Nanotubes in Neural Phaeochromocytoma-Derived PC12 Cells. *ACS Nano* **2010**, *4*, (6), 3181-3186.
69. Chen, J. M.; Hessler, J. A.; Putschakayala, K.; Panama, B. K.; Khan, D. P.; Hong, S.; Mullen, D. G.; DiMaggio, S. C.; Som, A.; Tew, G. N.; Lopatin, A. N.; Baker, J. R.; Holl, M. M. B.; Orr, B. G., Cationic Nanoparticles Induce Nanoscale Disruption in Living Cell Plasma Membranes. *J. Phys. Chem. B* **2009**, *113*, (32), 11179-11185.
70. Goodman, C. M.; McCusker, C. D.; Yilmaz, T.; Rotello, V. M., Toxicity of gold nanoparticles functionalized with cationic and anionic side chains. *Bioconjugate Chem.* **2004**, *15*, (4), 897-900.
71. Ojwang', L. M.; Cook, R. L., Environmental Conditions That Influence the Ability of Humic Acids to Induce Permeability in Model Biomembranes. *Environ. Sci. Technol.* **2013**, *47*, (15), 8280-8287.
72. Tabaei, S. R.; Rabe, M.; Zhdanov, V. P.; Cho, N. J.; Hook, F., Single Vesicle Analysis Reveals Nanoscale Membrane Curvature Selective Pore Formation in Lipid Membranes by an Antiviral alpha-Helical Peptide. *Nano Lett.* **2012**, *12*, (11), 5719-5725.
73. He, J.; Zhu, X.; Qi, Z.; Wang, C.; Mao, X.; Zhu, C.; He, Z.; Li, M.; Tang, Z., Killing Dental Pathogens Using Antibacterial Graphene Oxide. *ACS Appl. Mater. Interfaces* **2015**.
74. Sens, P.; Safran, S. A., Pore formation and area exchange in tense membranes. *Europhys. Lett.* **1998**, *43*, (1), 95-100.
75. Sandre, O.; Moreaux, L.; Brochard-Wyart, F., Dynamics of transient pores in stretched vesicles. *Proc. Natl. Acad. Sci. U. S. A.* **1999**, *96*, (19), 10591-10596.
76. Wang, J. L.; Wei, Y. J.; Shi, X. H.; Gao, H. J., Cellular entry of graphene nanosheets: the role of thickness, oxidation and surface adsorption. *RSC Adv.* **2013**, *3*, (36), 15776-15782.

77. Huang, H. W.; Chen, F. Y.; Lee, M. T., Molecular mechanism of peptide-induced pores in membranes. *Phys. Rev. Lett.* **2004**, *92*, (19).
78. Brochard-Wyart, F.; de Gennes, P. G.; Sandre, O., Transient pores in stretched vesicles: role of leak-out. *Physica A* **2000**, *278*, (1-2), 32-51.
79. Karatekin, E.; Sandre, O.; Guitouni, H.; Borghi, N.; Puech, P. H.; Brochard-Wyart, F., Cascades of transient pores in giant vesicles: Line tension and transport. *Biophys. J.* **2003**, *84*, (3), 1734-1749.
80. Wong-Ekkabut, J.; Baoukina, S.; Triampo, W.; Tang, I. M.; Tieleman, D. P.; Monticelli, L., Computer simulation study of fullerene translocation through lipid membranes. *Nat. Nanotechnol.* **2008**, *3*, (6), 363-368.
81. Zhu, T.; Xu, F.; Yuan, B.; Ren, C. L.; Jiang, Z. Y.; Ma, Y. Q., Effect of calcium cation on lipid vesicle deposition on silicon dioxide surface under various thermal conditions. *Colloid Surface B* **2012**, *89*, 228-233.
82. Taupin, C.; Dvolaitzky, M.; Sauterey, C., Osmotic-Pressure Induced Pores in Phospholipid Vesicles. *Biochemistry* **1975**, *14*, (21), 4771-4775.
83. Ohki, S., Effects of Divalent-Cations, Temperature, Osmotic-Pressure Gradient, and Vesicle Curvature on Phosphatidylserine Vesicle Fusion. *J. Membr. Biol.* **1984**, *77*, (3), 265-275.



**Chapter 3. Adsorption of Human Serum Albumin  
on Graphene Oxide: Implications for Protein  
Corona Conformation and Nanoparticle-Cell  
Membrane Interactions<sup>1</sup>**

---

<sup>1</sup> This chapter will be submitted for publication in a peer-reviewed journal. Co-author Chenxu Yan performed the batch adsorption experiments and wrote the Materials and Methods section for the batch experiments. Co-author Kai Loon Chen helped with data interpretation and manuscript editing.

### 3.1 Introduction

Owing to its unique optical,<sup>1</sup> mechanical,<sup>2</sup> chemical,<sup>3</sup> and antibacterial properties,<sup>4</sup> graphene oxide (GO) has recently found widespread applications in diverse fields including energy storage,<sup>5</sup> water treatment,<sup>6</sup> and sensing of biomolecules.<sup>7</sup> In particular, GO has been proposed as a promising candidate for efficient cellular imaging and drug delivery.<sup>8, 9</sup> Recently, GO has been reported to show cyto- and geno-toxicity toward human cells.<sup>10, 11</sup> A mechanistic understanding of how GO nanosheets interact with biological systems, when they are accidentally uptaken (e.g., from GO-contaminated water) or purposely administered (e.g., use of GO for drug delivery) into the human body, will enable a better assessment of the biological impacts of GO.

When nanoparticles enter a biological fluid (such as blood plasma), proteins present in the medium can adsorb on the nanoparticle surface to form protein coronas.<sup>12-14</sup> The formation of protein coronas on nanoparticles is expected to have at least two-fold implications for the biological impacts of nanoparticles. First, the coronas bound to nanoparticle surface confer a biological identity to the nanoparticles and have a pronounced influence on the cellular responses to the nanoparticles.<sup>12, 15</sup> In their study of the interactions of silica nanoparticles with A549 lung epithelial cells, Lesniak et al.<sup>16</sup> reported that weaker adhesion to cell membranes and lower internalization efficiency were observed when the nanoparticles were coated with protein coronas. Second, upon being adsorbed to nanoparticles, proteins may undergo conformational changes, which can lead to an alteration in the biological functions of the proteins.<sup>17</sup>

The formation of protein coronas on GO has been the subject of several recent studies. Chong et al.<sup>18</sup> demonstrated that the toxicity of GO toward A549 cells was decreased when

the GO was coated with bovine serum albumin (BSA). They also observed an alteration in the secondary structures of BSA upon binding to GO.<sup>18</sup> Lim and co-workers<sup>19</sup> reported that the wavelength of the maximum fluorescence emission of human serum albumin (HSA) was red-shifted, which is indicative of conformational change of the protein,<sup>20</sup> upon adsorbing on GO. These studies provide insights into the mechanisms for the interactions between GO and proteins. Nevertheless, there is still a lack of understanding of the influence of solution chemistry on the amount of proteins adsorbed on GO and the conformation of protein coronas. Such information is critical to evaluating the biological responses to GO when protein-coated GO is transported among different biological compartments with varying solution chemistries. In addition, our previous work has shown that GO can disrupt lipid bilayers upon favorable attachment.<sup>21</sup> The mechanisms by which protein coronas influence the adhesion of GO to cell membranes remain to be elucidated.

In this study, we investigate the adsorption of HSA, which is the most abundant protein in human plasma,<sup>22</sup> on GO. Adsorption isotherms of HSA on GO were obtained through batch experiments under varying solution chemistry conditions. Those isotherms will provide quantitative information on the absolute (dry) mass of HSA adsorbed on GO. The adsorption of HSA on GO was also investigated through quartz crystal microbalance with dissipation (QCM-D) measurements by employing GO-coated sensors. The QCM-D senses “wet” mass of protein layers (adsorbed proteins plus water associated with the proteins)<sup>23</sup> on GO. In addition, the QCM-D measurements provide information on the initial kinetics of protein adsorption. The combination of batch and QCM-D experiments can thus enable comprehensive understanding of the formation and conformation of protein coronas on GO. Finally, the impact of HSA adsorption on the attachment of GO to a supported lipid

bilayer (SLB) as a model cell membrane was investigated. Our findings provide fundamental insights into the interactions of serum proteins with GO and will enable a better understanding of the biological impacts of GO in different biological fluids with varying solution chemistry conditions.

## **3.2 Materials and Methods**

### **3.2.1 Preparation and Characterization of GO Suspensions**

GO powder was purchased from Graphene Laboratories Inc. (Calverton, NY). According to the supplier, the GO contains 79% carbon and 20 % oxygen. To prepare GO suspensions, 50 mg of GO powder was dispersed in 100 mL of DI water through ultrasonication in an ultrasonic bath (Branson 1510R-MT, output power 70 W, frequency 42 kHz) for 24 h. The resulting GO suspension, which showed a brownish color, was stored in a Pyrex bottle wrapped with aluminum foil at 4 °C. Two GO suspensions were prepared. One of the GO suspensions was directly used in the batch adsorption experiments (denoted as raw GO suspension, 500 mg/L as GO mass). The other GO suspension was subjected to centrifugation at 1,400 g (Avanti centrifuge J-20 XPI, Beckman Coulter Inc., Brea, CA) for 5 min, and the supernatant was withdrawn with glass pipets (denoted as GO supernatant) and was used for the preparation of GO-coated QCM-D sensors. The concentration of the GO supernatant was determined to be 120 mg/L (as total organic carbon, TOC) using a TOC analyzer (TOC-L, Shimadzu). The average hydrodynamic size of the GO-raw and GO-supernatant suspensions was determined as  $764 \pm 126$  nm and  $542 \pm 91$  nm, respectively, through dynamic light scattering (DLS) measurements (see below).

### 3.2.2 Solution Chemistry

ACS-grade NaCl, CaCl<sub>2</sub>, and NaHCO<sub>3</sub> were used for the preparation of stock solutions. All stock solutions were filtered through 0.1- $\mu$ m polyvinylidene fluoride filters (Millipore, MA) prior to use. The adsorption of HSA on GO was carried out under three pH conditions: pH  $7.0 \pm 0.5$ , buffered with NaHCO<sub>3</sub>; pH  $2.0 \pm 0.1$ , adjusted with 1 M HCl; and pH  $4.7 \pm 0.4$ , without pH adjustment.

### 3.2.3 Dynamic Light Scattering (DLS)

Time-resolved DLS measurements were carried out with a light scattering unit to investigate the hydrodynamic size of GO and the rates of aggregation of GO and HSA-modified GO. This unit is composed of an argon laser (Lexel 95, Cambridge laser, CA) that emits laser light at a wavelength of 488 nm, a photomultiplier tube mounted on a goniometer (BI-200SM, Brookhaven, NY), a digital correlator (BI-9000AT, Brookhaven, NY), and a thermostatted vat filled with an index-matching *cis*- and *trans*-mixture of decahydronaphthalene. The room temperature was maintained at 25 °C. New borosilicate glass vials (VWR) were soaked in a 2 % Extran solution (Extran MA01, Merck KGaA, Darmstadt, Germany) for at least 2 hr, rinsed extensively with DI water, and oven-dried prior to use. For the investigation of the aggregation of GO in the absence and presence of HSA, a predetermined amount of NaCl solution was introduced to a glass vial containing either a diluted GO suspension or a mixture of GO and HSA. The total volume of the suspension was 1 mL. After the suspension in the vial was briefly mixed using a vortex mixer, the vial was inserted into the vat and the DLS measurement was started immediately. All DLS measurements were conducted at a scattering angle of 90°. Each autocorrelation function

was accumulated for 15 s. The intensity-weighted hydrodynamic diameters were derived through second-order cumulant analysis (Brookhaven software).

### **3.2.4 Atomic Force Microscopy (AFM) Imaging of GO Nanosheets**

Half microliter of the diluted GO suspension was subjected to ultrasonication for 10 min, deposited on a freshly cleaved mica (V1 grade, SPI Supplies, PA), and then dried in the air. The mica was mounted on the stage of an AFM (Multimode NanoScope IIIa, Bruker Nano Inc.) and was imaged with a RTESP cantilever (Bruker) in tapping mode. The AFM images were analyzed using NanoScope Analysis Software (version 1.50, Bruker).

### **3.2.5 Electrophoretic mobility (EPM) measurements**

The EPMs of GO were measured (ZetaPALS, Brookhaven Instruments Corp., Holtsville, NY) using GO-supernatant under varying solution chemistry conditions. The concentration of GO used in all EPM measurements was 6 mg TOC/L. Three samples were measured at each condition. For most of the experimental conditions, ten measurements were conducted for each sample. At high NaCl concentration (150 mM), only five measurements were conducted in order to minimize the effect of GO aggregation.

### **3.2.6 Batch Adsorption Experiments**

Lyophilized powder HSA ( $\geq 97\%$ , M.W. 66.5 kDa, Sigma-Aldrich) was used for the preparation of HSA solutions. Batch experiments were conducted in 2-mL low protein binding centrifuge tubes (LoBind, Eppendorf) at room temperature ( $20 \pm 1$  °C). A mass concentration of 120 mg/L for GO was used in all experiments. Batch experiments were carried out under six conditions: pH  $7.4 \pm 0.5$  with 1 mM, 30 mM, 150 mM NaCl or 0.33 mM  $\text{CaCl}_2$ ; and pH  $2.0 \pm 0.1$  or pH  $4.7 \pm 0.4$  with 150 mM NaCl. Experiments were carried

out in triplicates under each condition. HSA stock solution was prepared immediately prior to the experiments by dissolving HSA powder (Sigma-Aldrich) in deionized water. The HSA stock solution was spiked into the centrifuge tubes to initiate the adsorption. All the samples were wrapped with aluminum foil and mixed on a rotator (TC-7, New Brunswick Scientific) at 45 rpm for 6 hours. We have verified that this duration of adsorption was sufficient for samples to reach apparent adsorption equilibrium (no further adsorption of HSA after 6 hours) based on our preliminary experiment.

After 6-hr adsorption, all samples were centrifuged at 25,000 g (Centrifuge 5417R, Eppendorf) for a pre-determined duration to separate GO from the aqueous phase. The duration of centrifugation was 60 minutes at pH 7.4 with 1 mM, 30 mM NaCl and 0.33 mM CaCl<sub>2</sub>; 5 minutes at pH 7.4 and 150 mM NaCl; 3 minutes at pH 2.0 and 150 mM NaCl; and 2 minutes at pH 4.7 and 150 mM NaCl. Such durations of centrifugation were chosen such that less than 2 % (mass vs. mass) GO remained in the supernatant after centrifugation under all conditions. The percentage of GO remained in the supernatant after centrifugation was determined via comparison of scattered light intensities, measured by DLS, between the supernatant and a GO suspension with a predetermined mass concentration. This method was validated by the fact the HSA in the supernatant scattered significantly less light than GO.

The supernatants containing HSA were diluted 10 times in 40 mL amber vials and the HSA concentrations were subsequently determined using a total organic carbon analyzer (TOC-L, Shimadzu). We determined in our preliminary experiments that the adsorption of HSA to the LoBind centrifuge tubes was negligible over the course of the adsorption

experiments. The adsorbed mass of HSA was calculated from the difference between added mass and the mass in the supernatant.

The assumptions for Langmuir isotherm model (e.g., homogeneous adsorption sites and no adsorbate-adsorbate interactions) are invalid in the case of protein adsorption.<sup>24, 25</sup> Herein, the isotherms of HSA on GO were fit to the Freundlich model:

$$q = K_F C_w^n \quad (3.1)$$

where  $q$  (mg HSA/mg GO) and  $C_w$  (mg/L) are the equilibrium adsorbed and solution concentrations of HSA, respectively;  $K_F$  [(mg HSA)<sup>1- $n$</sup>  L <sup>$n$</sup>  (mg GO)<sup>-1</sup>] is the Freundlich affinity coefficient; and  $n$  (unitless) is the Freundlich linearity index.<sup>26</sup> The parameter  $K_F$  reflects the adsorption density and can be understood as indication of the overall binding strength between the adsorbate and adsorbent.<sup>27</sup>

### 3.2.7 Preparation of GO-coated QCM-D Sensors

We employed a layer-by-layer approach to assemble GO layers on 5 MHz quartz crystal sensors with silica-coated surfaces (QSX 303). A QCM-D E4 setup (Biolin Scientific, Västra Frölunda, Sweden) was used for the modification of the sensors with GO and the subsequent adsorption of HSA on the GO-coated sensors. Prior to each experiment, the sensors were cleaned and dried using a protocol described previously.<sup>21, 28</sup> The temperature inside the QCM-D chambers was maintained at 25 °C. A flow rate of 0.1 mL/min, corresponding to laminar flow condition in the chambers,<sup>29</sup> was employed in all QCM-D measurements.

A solution of 0.1 g/L poly-L-lysine (PLL, molecular weight 70,000–150,000, Sigma-Aldrich) dissolved in a buffer containing 10 mM N-(2-hydroxyethyl)-piperazine-N'-(2-ethanesulfonic acid) (HEPES) and 100 mM NaCl was flowed through the QCM-D chambers



to allow for the adsorption of PLL on the sensors. Next, a GO suspension at a concentration of 30 mg TOC/L (buffered with 1 mM NaHCO<sub>3</sub> at pH 7) was flowed across the sensor surface to allow for the favorable deposition of a GO layer on top of the positively charged PLL layer. Finally, the chambers were rinsed with 1 mM NaHCO<sub>3</sub> to remove unadsorbed GO.

In order to test the coverage of the GO layer, we investigated the deposition of negatively charged gold nanoparticles (AuNPs) (NanoXact, NanoComposix, San Diego, CA) on GO-coated sensors as well as on PLL-coated sensors. The AuNPs were observed under a transmission electron microscope (TEM, Philips EM 420). A drop of AuNP suspension was deposited and dried on a formvar/carbon-coated grid prior to being observed under the TEM at 100 kV. The size distribution of the AuNPs (Figure 3.1) was obtained from the TEM images by measuring the diameters of 128 individual AuNPs using ImageJ software (National Institutes of Health). The average diameter of the AuNPs was determined to be 5.6 nm.

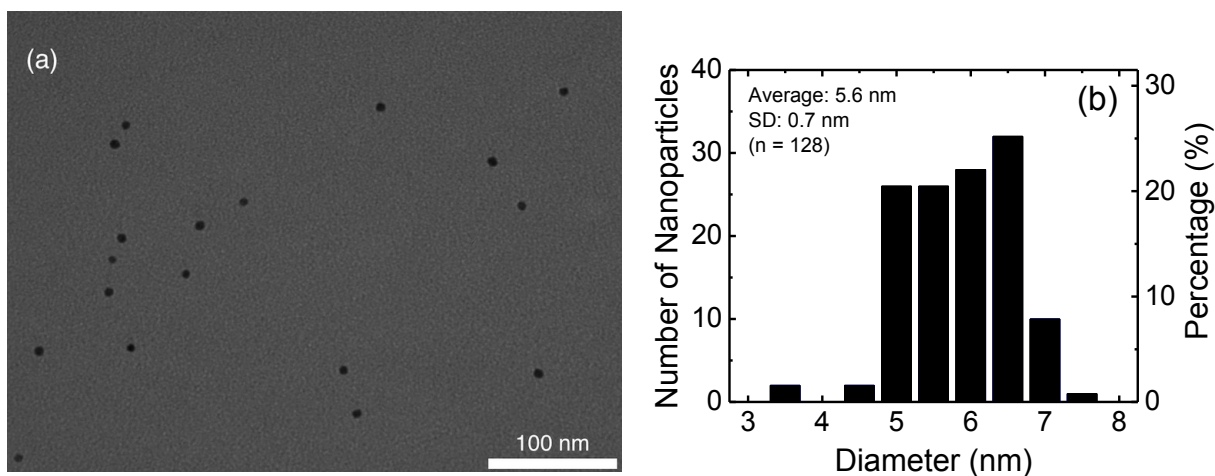


**Figure 3.1.** (a) Representative TEM of gold nanoparticles (AuNPs). The scale bar represents 100 nm. (b) Size distribution of 128 AuNPs adsorbed on a TEM grid. Longest dimensions were measured for slightly elongated nanoparticles. Each bar represents a diameter range of 0.5 nm.

The deposition of the AuNPs on a sensor exposed successively to PLL and GO, as well as on a sensor that is solely exposed to PLL, was shown in Figure 3.2. Appreciable deposition of AuNPs was observed on the PLL-coated sensor, while the deposition of AuNPs on GO-coated sensor was undetected. This result implies that there were no exposed PLL regions larger than  $5 \times 5$  nm on the GO-coated sensor. Since HSA has a dimension of  $8 \times 8 \times 3$  nm,<sup>30</sup> the adsorption of HSA on the GO-coated sensor is expected to be attributed solely to GO-HSA interactions.

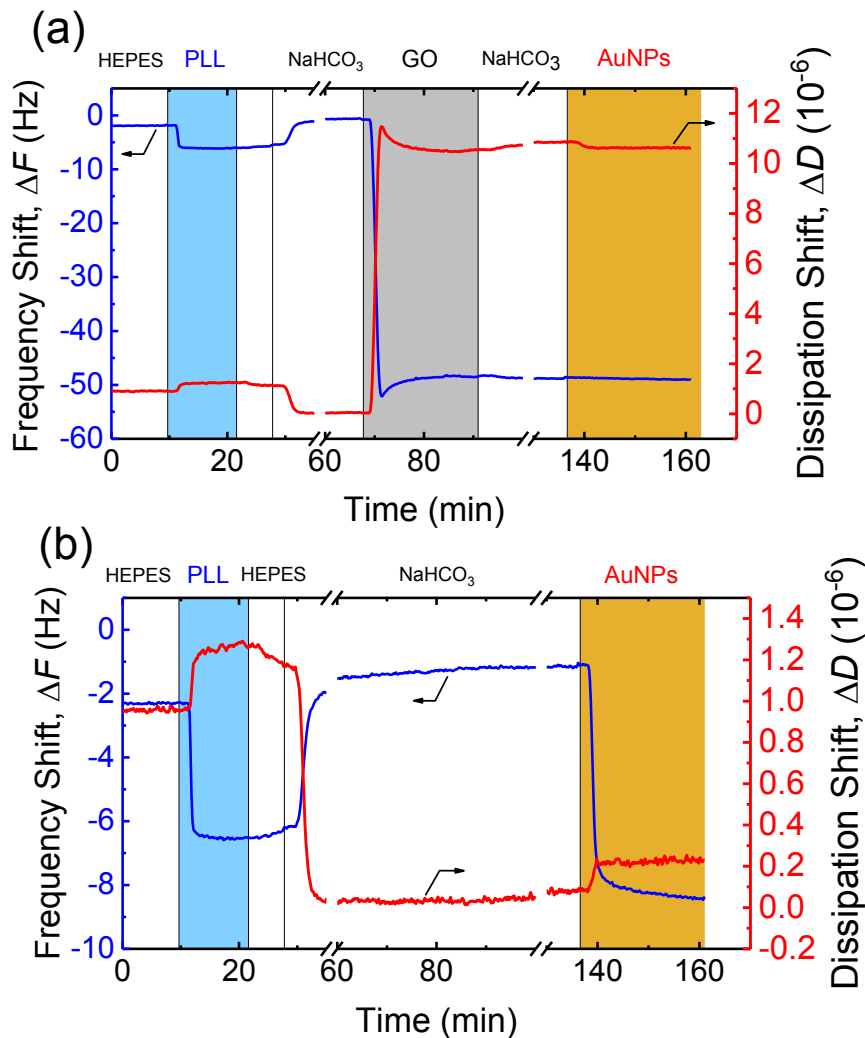


**Figure 3.2.** (a) Coating of a QCM-D sensor with a GO layer and the deposition of AuNPs on the GO layer. (b) Coating of a QCM-D sensor with PLL and the deposition of AuNPs on the PLL layer. Duplicate experiments were performed and similar results were obtained.

### 3.2.8 Adsorption of HSA on GO-coated Sensors

Following the coating of QCM-D sensors by GO, an electrolyte solution of interest was flowed through the chambers until a stable baseline was attained. A HSA solution prepared in the same electrolyte solution (125 mg/L) was introduced to the chambers to initiate the adsorption process. After 2-h adsorption, the same electrolyte solution was flowed through the chambers to test the reversibility of HSA adsorption on GO.

The deposition or adsorption of mass on the sensors result in a decrease in the resonance frequency of the sensor ( $\Delta f$ ), which can be related to the mass added on the sensor ( $\Delta m$ ) according to the Sauerbrey equation:<sup>31</sup>

$$\Delta m = -C \frac{\Delta f}{n} \quad (3.2)$$

where  $C$  is the mass sensitivity factor ( $= 17.7 \text{ ng cm}^{-2} \text{ Hz}^{-1}$  at 5 MHz) and  $n$  is the overtone number (1, 3, 5, 7, 11, 13). The Sauerbrey relation can be applied for sufficiently rigid and thin layers that are evenly distributed over the sensor surface.<sup>12</sup> The deposition or adsorption of a viscoelastic layer will result in an enhancement in the ability of the sensor to dissipate energy, which is represented by the dissipation factor  $D$ .<sup>32</sup> Reviakine et al.<sup>33</sup> proposed that the Sauerbrey equation can be applied to the adsorbed layer when the ratio of  $\Delta D/\Delta f$  is significantly less than  $0.4 \times 10^{-6}/\text{Hz}$ . The ratios of  $\Delta D/\Delta f$  values for HSA layers were calculated from the total frequency and dissipation shifts (in 7<sup>th</sup> overtone) caused by the adsorption of HSA on GO. Under most conditions employed in HSA adsorption experiments, the ratio  $\Delta D/\Delta f$  was lower than  $0.12 \times 10^{-6}/\text{Hz}$  and the wet mass of HSA layer on GO was derived using the Sauerbrey model. At pH 2.0 and 150 mM NaCl, the ratio  $\Delta D/\Delta f$  was high (ca.  $0.5 \times 10^{-6}/\text{Hz}$ ), indicating that the HSA layer was viscoelastic.<sup>34</sup> The wet mass estimated

using Sauerbrey model is thus underestimated under this condition as suggested by Höök et al.<sup>23, 35</sup>

### **3.2.9 Deposition of GO and HSA-modified GO on DOPC SLBs**

To examine the influence of HSA adsorption on the interactions of GO with model cell membranes, we investigated the rate of deposition of GO and HSA-modified GO on DOPC SLBs. The preparation of DOPC vesicles and the formation of DOPC SLBs on silica-coated QCM-D sensors have been described in previous publications<sup>21, 36</sup> and also in Chapter 2. To prepare HSA-modified GO, 10 mg/L HSA and 6 mg/L GO were mixed in a centrifuge tube at a solution chemistry of interest followed by being left on the bench for 20 min to allow for the adsorption of HSA on GO. After the formation of SLBs on QCM-D sensors, an electrolyte solution of interest was flowed through the chambers to obtain a stable baseline. Next, either a GO suspension (6 mg/L) or a mixture of GO and HSA (6 mg/L GO, 10 mg/L HSA) was introduced to the chambers to initiate the deposition process. The rate of deposition, expressed as the rate of frequency shift (Hz/min), was calculated by performing a linear regression during the initial 10 min of GO deposition.

## **3.3 Results and Discussion**

### **3.3.1 Characterization of GO**

AFM imaging revealed that the thickness of the GO nanosheets was ca. 1 nm (Figure 3.3), consistent with that of monolayer GO.<sup>37</sup> The EPMs of GO were measured at 150 mM NaCl under varying pH conditions (Figure 3.4a). Over the pH range of 2.0–7.0, GO was negatively charged owing to the deprotonation of carboxyl groups on the edges and basal

planes of GO.<sup>3</sup> A decrease in pH from 7.0 to 2.0 results in a reduction in the magnitude of the EPM of GO (Figure 3.4a), which is expected since fewer carboxyl groups were dissociated under lower pH conditions. At an ionic strength of 1 mM, the magnitude of the EPM of GO was smaller in the presence of calcium (Figure 3.4b). The presence of CaCl<sub>2</sub> reduced the EPMs through charge neutralization stemming from the binding of calcium ions to the dissociated carboxyl groups.<sup>28</sup>

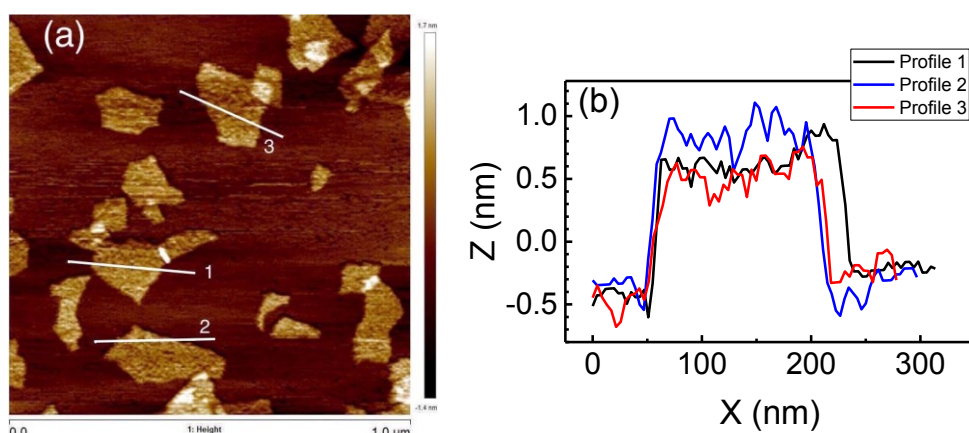


**Figure 3.3.** (a) AFM images of GO on mica. (b) AFM Height profiles of GO. The positions of the profiles are marked as white lines in (a).

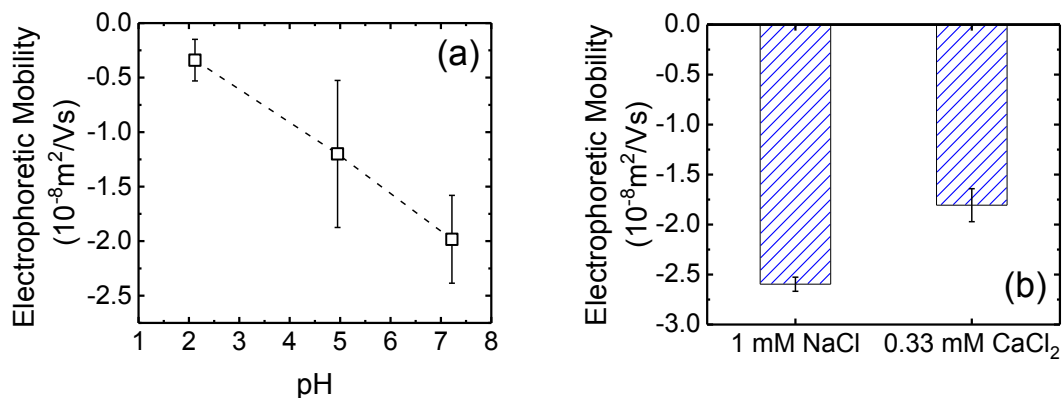


**Figure 3.4.** (a) EPMs of GO at 150 mM NaCl under different pH conditions. (b) EPMs of GO at pH 7.0 with an ionic strength of 1 mM in the absence and presence of calcium ions. Error bars represent standard deviations.

### 3.3.2 Influence of Ionic Strength on HSA Adsorption on GO

The isotherms at pH 7.0 and varying NaCl concentrations are presented in Figure 3.5a and the fitted parameters ( $K_F$  and  $n$ ) are shown in Table 3.1. The adsorbed absolute mass of HSA ( $q$ ) increased with increasing the equilibrium HSA concentration in solution ( $C_w$ ) at 1, 30, and 150 mM. The adsorbed mass followed the order 150 mM > 30 mM > 1 mM when  $C_w$  was below 125 mg/L. At higher  $C_w$ , the adsorbed mass was comparable at 30 and 150 mM NaCl, both higher than that at 1 mM NaCl. It is notable that  $K_F$  increases with increasing NaCl concentration, suggesting that the overall binding strength between HSA and GO increases with the rise in ionic strength.

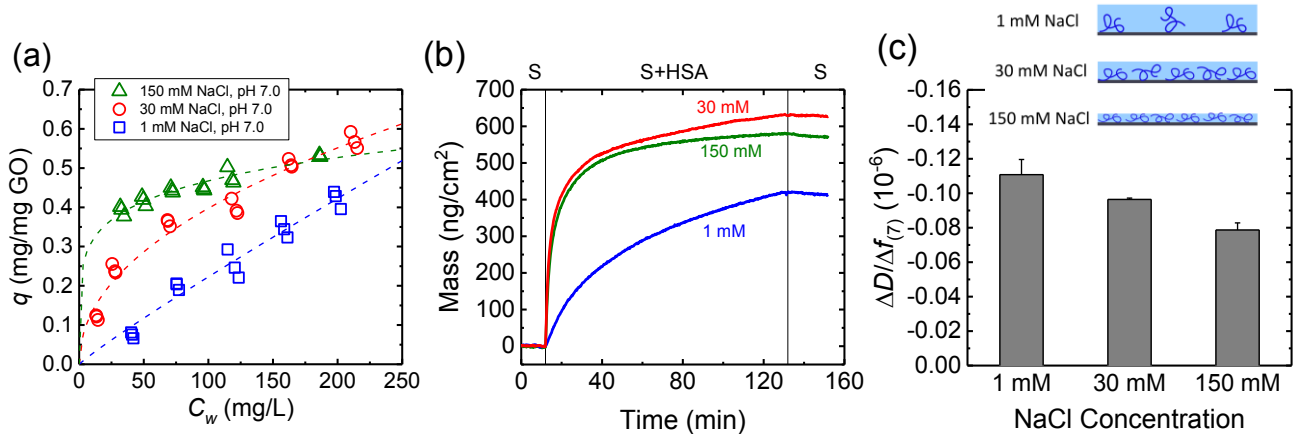


**Figure 3.5.** (a) Adsorption isotherms of HSA on GO at pH 7.0. Dashed lines represent Freundlich fitting. (b) Wet mass of HSA adsorbed on a GO layer estimated using Sauerbrey model during the exposure of the GO layer to 125 mg/L HSA at pH 7.0 followed by rinsing with background electrolytes. Vertical lines indicate the time points at which solutions were switched from protein-free solutions (S) to protein solutions (S+HSA) and finally back to protein-free solutions (S). (c) Overall  $\Delta D/\Delta f$  values calculated from data in (b). The cartoon illustrates the proposed conformation of HSA layers on GO under different ionic strengths.

The “wet” mass of protein layer adsorbed on GO, which is calculated from the frequency shifts during the exposure of GO-coated QCM-D sensors to HSA based on Sauerbrey model, is presented in Figure 3.5b. The wet mass of adsorbed HSA layer

increased with time over the course of 2 h at all ionic strengths. The HSA layer was subsequently rinsed with the same electrolyte solution. Negligible release of HSA upon rinsing was observed, indicating that the adsorption of HSA on GO was largely irreversible.

**Table 3.1.** Fitted parameters of Freundlich isotherm for HSA adsorption on GO.

Conditions	Freundlich Model		
	$q_e = K_F C_e^n$		
	$K_F$	$n$	$R^2$
1 mM NaCl, pH 7	0.0032	0.9233	0.9431
30 mM NaCl, pH 7	0.0451	0.4725	0.9597
150 mM NaCl, pH 7	0.2111	0.1727	0.9043
0.33 mM CaCl <sub>2</sub> , pH 7	0.0560	0.4271	0.9624
150 mM, pH 2	0.4018	0.0595	0.5214
150 mM, pH 4.7	0.5832	0.0854	0.8726

The irreversibility of HSA adsorption on GO is indicative of the strong binding between HSA and GO. The protein coronas formed around nanoparticles are divided into two categories: “soft” corona, where rapid dynamic exchange of proteins between the medium and the particles dominates, and “hard” corona, where the affinity of proteins to the particle surface is strong.<sup>13</sup> Proteins in soft corona are loosely associated with the particle surface and can be readily desorbed upon exposure to protein-free solutions.<sup>13</sup> Therefore, the HSA layers adsorbed on the GO-coated sensors are expected to have similar properties to the hard coronas formed around GO. Our results from QCM-D experiments can thus help elucidate the conformation of hard coronas on GO under varying conditions.

Figure 3.5b shows that the wet mass of HSA layer was larger at 30 mM and 150 mM than 1 mM, consistent with the absolute mass of adsorption shown in Figure 3.5a. However,

the wet mass was slightly lower at 150 mM than 30 mM, which is opposite to the order for the absolute mass of adsorption under similar equilibrium HSA concentration (125 mg/L). This observation indicates that more water was coupled in the HSA layer at 30 mM than 150 mM, which overwhelmed the difference in absolute HSA adsorption under these conditions. Another notable observation from Figure 3.5b is that the initial rate of HSA adsorption on GO (initial slope in mass–time plot) was much smaller at 1 mM than 30 and 150 mM.

The conformation of the adsorbed HSA layer on GO under varying ionic strength was investigated by comparing the ratios of  $\Delta D/\Delta f$  (Figure 3.5c). Higher  $\Delta D/\Delta f$  values indicate that the adsorbed layer is more fluid or hydrated, whereas lower  $\Delta D/\Delta f$  values are indicative of more rigid/compact layers on the sensor.<sup>38,39</sup> The ratio  $\Delta D/\Delta f$  decreases with the increase in ionic strength, indicating that the adsorbed HSA layers were the most fluid at 1 mM and most rigid at 150 mM.

The adsorption of HSA on surfaces is a complex process which involves intertwining subprocesses including the electric double layer (EDL) and van der Waals interactions between proteins and the surface, structural rearrangements of proteins, and change in degree of hydration of proteins and the surface upon adsorption.<sup>25,40</sup> The ionic strength of solution can regulate the EDL interactions between protein and GO and between adsorbed proteins, thereby influencing HSA adsorption. The isoelectric point (IEP) of HSA has been reported as 4.7–5.8.<sup>41-43</sup> At pH 7.0, HSA carries net negative charge which is the same sign as the surface charge of GO. At 1 mM, the thickness of the EDL of both HSA and GO (characterized by the Debye screening length) was ca. 10 nm. The overlapping of EDLs of the protein and the adsorbent is enthalpically unfavorable,<sup>25</sup> resulting in lower binding affinity between HSA and GO at 1 mM. Additionally, the presence of EDL repulsion gave



rise to an energy barrier to the deposition of HSA on GO and caused a slower rate of adsorption at 1 mM (Figure 3.5b). Furthermore, the EDL repulsion between adsorbed HSA molecules led to a sparse distribution of HSA on GO and thereby a more fluid/hydrated HSA layer at 1 mM (Figure 3.5c). Due to screening of the charge of both HSA and GO at 150 mM, the adsorption density was highest and the HSA layer took the most compact structure (Figure 3.5a and c).

### 3.3.3 Influence of Calcium on HSA Adsorption on GO

Calcium ions are a key constituent in biological fluids and are present in human plasma at a concentration of ca. 1 mM.<sup>44, 45</sup> The effect of calcium ions on the adsorption of HSA on GO at neutral pH and an ionic strength of 1 mM was investigated. The adsorbed dry mass of HSA on GO increases with increasing  $C_w$  in the presence and absence of calcium (Figure 3.6a). In the presence of calcium ions, the adsorbed dry mass and the fitted  $K_F$  (Table 3.1) were both higher, indicating stronger binding between HSA and GO. Higher rate of initial adsorption and greater wet mass uptake during the exposure of GO layer to HSA were observed in the presence of calcium (Figure 3.6b). The lower ratio of  $\Delta D/\Delta f$  (Figure 3.6c) indicates that a more compact HSA layer was formed on GO in the presence of calcium.

The presence of calcium ions results in a reduction in the magnitude of the EPMS of GO (Figure 3.4b). Additionally, calcium ions can neutralize the charge of HSA molecules at neutral pH through binding to the imidazole and deprotonated carboxyl groups of HSA.<sup>46</sup> In addition to forming a monodentate chelate with one of these groups, one calcium ion can bind to two of these groups on HSA to form a bidentate chelate<sup>46</sup> which is more stable than a monodentate chelate. As a consequence of the lower magnitude of the surface charge of GO and the net charge of HSA, the EDL repulsion between HSA and GO was reduced in the

presence of calcium, resulting in faster initial adsorption. Furthermore, calcium ions can serve as a bridge between two deprotonated carboxyl groups from different peptide chains.<sup>47</sup> It is expected that such bridging can take place between two adjacent HSA molecules, leading to the adsorption of a HSA layer with a dense protein distribution and a rigid structure in the presence of calcium.

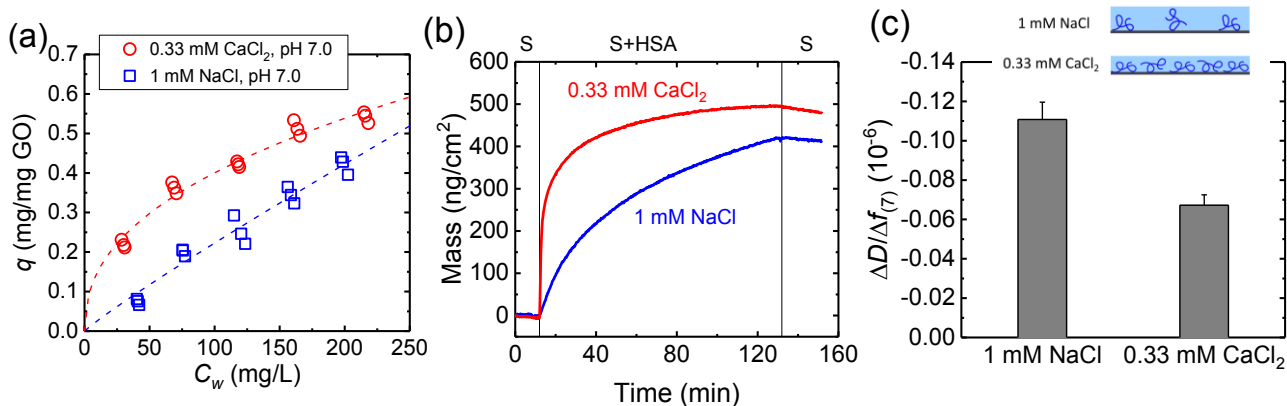


**Figure 3.6.** (a) Adsorption isotherms of HSA on GO at pH 7.0 in the absence and presence of calcium ions. Dashed lines represent Freundlich fitting. (b) Wet mass of HSA adsorbed on a GO layer estimated using Sauerbrey model during the exposure of the GO layer to 125 mg/L HSA at pH 7.0 followed by rinsing with background electrolytes. Vertical lines indicate the time points at which solutions were switched from protein-free solutions (S) to protein solutions (S+HSA) and finally back to protein-free solutions (S). (c) Overall  $\Delta D/\Delta f$  values calculated from data in (b). The cartoon illustrates the proposed conformation of HSA layers on GO in absence and presence of calcium.

### 3.3.4 Influence of pH on HSA Adsorption on GO

The adsorption of HSA on GO was investigated at 150 mM (ionic strength in most biological fluids)<sup>14</sup> under pH 2.0, 4.7, and 7.0, which are lower than, equal to, and higher than the IEP of HSA, respectively. These pH conditions are also close to the pH of some biological fluids. For example, the pH of human gastric fluids, duodenal fluids, and blood is ca. 1–3, ca. 5–6, and ca. 7.4, respectively.<sup>48-50</sup> The dry mass of HSA adsorption generally

increased with increasing  $C_w$  under pH 2.0, 4.7, and 7.0 (Figure 3.7a). The dry mass of adsorption was higher at pH 4.7 than 2.0 and 7.0. The wet mass of HSA layer adsorbed on GO (Figure 3.7b) followed the order pH 2.0 > pH 4.7 > pH 7.0. The contrary orders of dry and wet mass of HSA adsorption at pH 2.0 and 4.7 indicate that more water was trapped in the adsorbed HSA layer at pH 2.0. This proposition is further supported by the observation that the ratio  $\Delta D/\Delta f$  at pH 2.0 was over 5 times higher than that at pH 4.7 (Figure 3.7c). The lowest  $\Delta D/\Delta f$  value was observed at pH 4.7, suggesting that the adsorbed HSA layer took the most compact conformation.

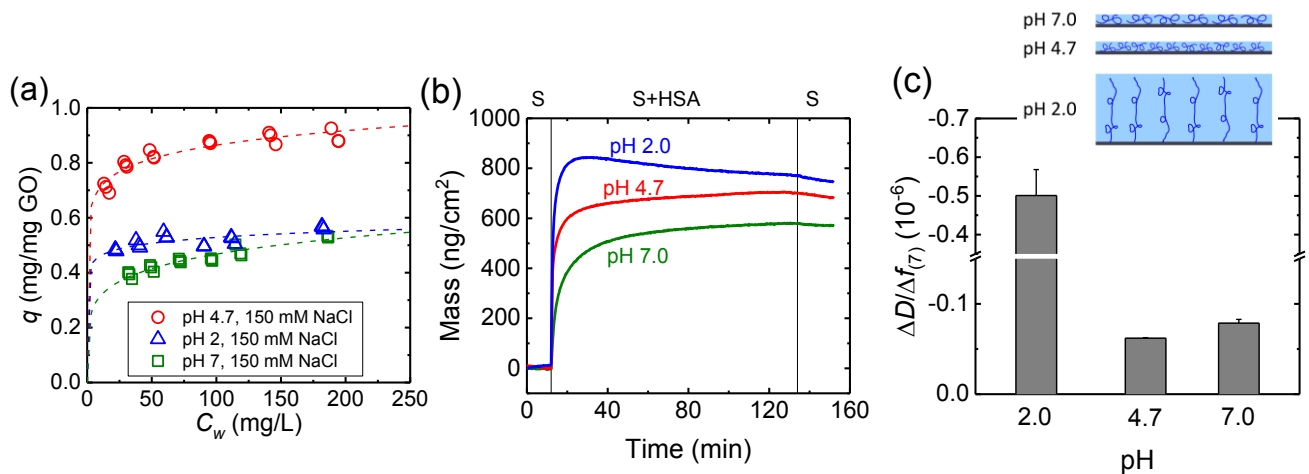


**Figure 3.7.** (a) Adsorption isotherms of HSA on GO at 150 mM NaCl under varying pH conditions. Dashed lines represent Freundlich fitting. (b) Wet mass of HSA adsorbed on a GO layer estimated using Sauerbrey model during the exposure of the GO layer to 125 mg/L HSA at 150 mM NaCl followed by rinsing with background electrolytes. Vertical lines indicate the time points at which solutions were switched from protein-free solutions (S) to protein solutions (S+HSA) and finally back to protein-free solutions (S). (c) Overall  $\Delta D/\Delta f$  values calculated from data in (b). The cartoon illustrates the proposed conformation of HSA layers on GO under different pH conditions.

The stronger adsorption and more compact HSA layer at pH 4.7 than at 7.0 (Figure 3.7a and c) is most likely due to the difference in the net charge of HSA under these two

conditions. Between pH 4.5 and 8, most HSA molecules are expected to take its normal conformation (N form).<sup>51</sup> With the decrease in pH from 7.0 to 4.7, the surface of GO became less negatively charged (Figure 3.4a), whereas the net charge of HSA changed from negative to zero. At IEP, the protein molecules take the most compact structure as the intramolecular electrostatic repulsion is minimized.<sup>52</sup> In addition, the adsorbed HSA molecules experience negligible electrostatic repulsion between one another. Koutsoukos et al.<sup>53</sup> reported that the lateral interactions between adsorbed HSA molecules were the most enthalpically favorable at the IEP of HSA. The adsorbed HSA molecules at IEP can interact with one another favorably, resulting in a high packing density of HSA on GO. Maximum adsorption near the IEP of HSA was also reported on polystyrene,<sup>54</sup> silicon wafer,<sup>42</sup> and TiO<sub>2</sub><sup>51</sup> surfaces.

At neutral pH, HSA is heart shaped, consisting of three homologous domains with similar 3-D structures.<sup>30</sup> When the pH is lowered to 2.0, HSA carries net positive charge due to the protonation of ionizable residues. The electrostatic repulsion between positively charged residues in adjacent domains of HSA leads to a separation of the domains and further a structural transition of HSA to a fully extended conformation (E form) with a high aspect ratio.<sup>55-57</sup> Despite the electrostatic attraction between HSA and GO at pH 2.0, the lower dry mass adsorption at pH 2.0 than pH 4.7 (Figure 3.7a) is likely due to the lateral repulsion between adsorbed HSA molecules and a more sparse distribution of HSA on GO. Under the extended conformation at pH 2.0, more residues in HSA are exposed to the solution<sup>58</sup>, thereby increasing the amount of water bound to the HSA molecules through H-bonding and leading to a more fluid HSA layer on GO.

### 3.3.5 Evolution of Protein Layer Conformations Over Time during HSA Adsorption

The  $\Delta D$  versus  $\Delta f$  ( $D$ - $f$ ) plots are shown in Figure 3.8 to reveal the change in fluidity of the HSA layers adsorbed on GO. The origin (0,0) in each plot corresponds to the onset of HSA adsorption on GO. The point with the highest  $D$  value in each plot represents the endpoint of HSA adsorption on GO. A two-stage adsorption process, as shown by the two stages with different slopes in the  $D$ - $f$  plots, was observed for all conditions investigated except for pH 2.0 (Figure 3.8c). At pH 7.0 and 1 mM NaCl, the  $D$ - $f$  plot was characterized by an initial stage with a higher slope (in magnitude) followed by a stage with a lower slope (Figure 3.8a). This decrease in slope suggests that the adsorbed HSA layer on GO became more compact with time. This is consistent with the findings by Richter and co-workers<sup>59, 60</sup> who reported that less water is coupled with adsorbed proteins with the increase in surface coverage. Such decrease in slope in the  $D$ - $f$  plots was also observed in the adsorption of BSA on a poly(acrylic acid) film at pH 7.0 under an ionic strength of 10 mM.<sup>61</sup>

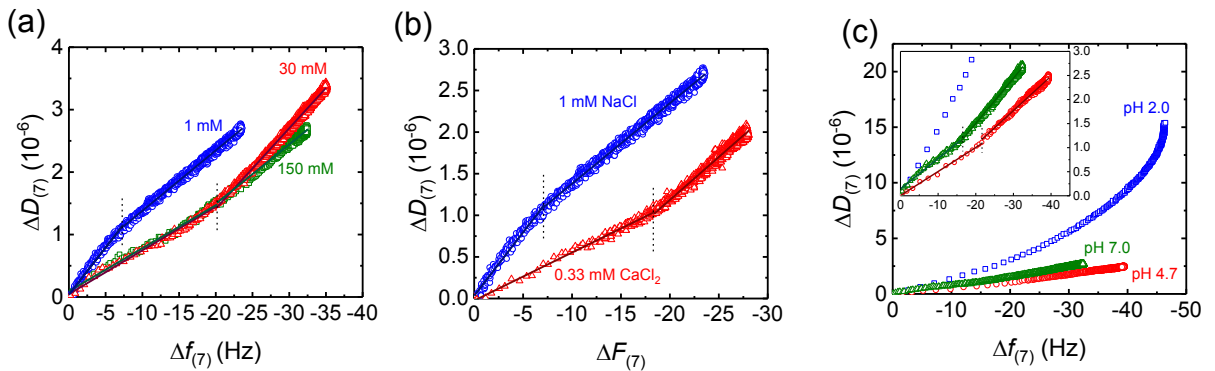


**Figure 3.8.** Dissipation shift versus frequency shift plots using QCM-D data at pH 7.0 as a function of (a) ionic strength (b) calcium presence, and (c) at 150 mM NaCl as a function of pH. Inset in (c) shows the linear fitting at pH 4.7 and 7.0. The  $\Delta D$  and  $\Delta f$  data between the onset of HSA adsorption and the point where  $\Delta f$  reaches maximum magnitude are used in all  $D/f$  plots. Vertical dashed lines represent the break points of the two-stage adsorption processes. Duplicate experiments were conducted and similar results were obtained.

Under higher ionic strength (30 and 150 mM) at pH 7.0 and 4.7, an opposite trend was observed: the slope in the second adsorption stage was larger than that in the first stage. (Figure 3.8a and c). Similar trend was also observed in the presence of calcium ions (Figure 3.8b). These observations are indicative of the formation of a more compact HSA layer on GO followed by the adsorption of a looser layer.

Höök et al.<sup>62</sup> observed similar *D-f* plots (higher slope in second stage) during the adsorption of hemoglobin on hydrophobic surfaces. They proposed that the adsorption of the first protein layer involves structural/conformational changes of proteins whereas the proteins in the second layer take native conformations.<sup>62</sup> Our findings are in accordance with Höök's reports and suggest that conformational changes of HSA may have taken place during the initial adsorption of HSA on GO. In aqueous solutions the hydrophobic residues in HSA are mostly buried in the interior of the molecules.<sup>25</sup> On GO surface, HSA can undergo structural changes to allow for the direct contact of its hydrophobic residues with the hydrophobic sp<sup>2</sup> regions on GO.<sup>25, 63</sup> The conformational change of HSA on GO has been reported by Ding et al.<sup>18</sup> who observed a decrease in  $\alpha$ -helical content of HSA upon being adsorbed on GO. The looser HSA layer in the second stage is likely a result of a reduction in available hydrophobic regions on GO and thus less conformational change of subsequently adsorbed HSA molecules.<sup>61</sup> It is worth noting that such adsorption of a tighter protein layer followed by a looser layer on GO was not observed at 1 mM NaCl and pH 7.0 likely due to the strong electrostatic repulsion between HSA molecules.

To verify the key role of hydrophobic interactions in driving HSA adsorption on GO, the adsorption of HSA on a hydrophilic silica-coated sensor was investigated (Figure 3.9). At pH 2.0 and 7.0, the adsorption of HSA on silica was negligible and was much smaller than

that on GO. The van der Waals attraction between HSA and silica is expected to be stronger than that between HSA and GO, as the Hamaker constant of silica is much higher than that of GO (6.3<sup>64</sup> and 0.237<sup>65</sup>, respectively). The striking difference in HSA adsorption on GO and silica at pH 2.0 likely stems from the fact that GO contains hydrophobic sp<sup>2</sup> regions<sup>3</sup> while the silica-coated sensor is highly hydrophilic (contact angle with water < 5 °).<sup>66</sup>

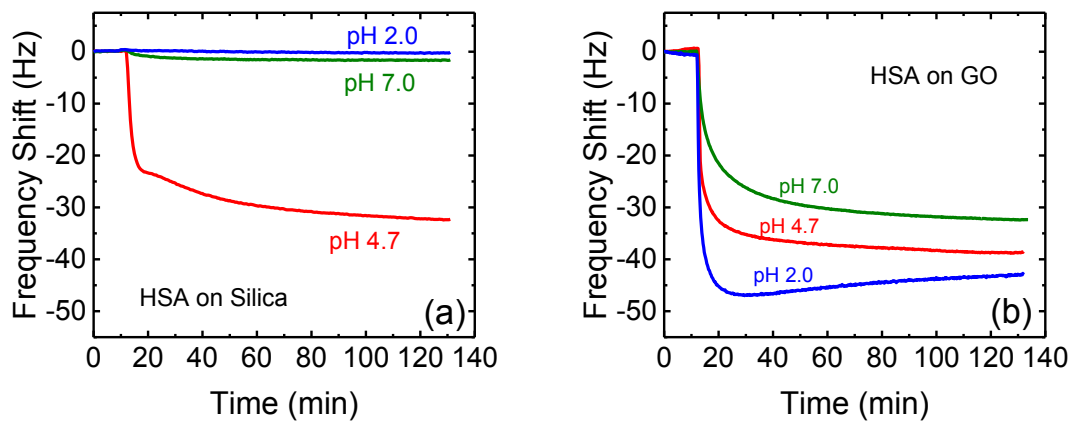


**Figure 3.9.** Frequency shifts during the adsorption of 125 mg/L HSA on silica (a) and GO (b) at 150 mM NaCl under varying pH conditions.

At pH 2.0, the magnitude of slope  $\Delta D/\Delta f$  continuously increased with the adsorption of HSA (Figure 3.8c). Besides the aforementioned structural change of HSA on GO due to hydrophobic interactions, the extended conformation of HSA at pH 2.0 may also contribute to the increase in slope. During the initial stage of HSA adsorption, HSA may adsorb on GO either via a side-on or end-on orientation, as there were plenty of binding sites on GO. With the increase in surface coverage of HSA on GO, the incoming HSA molecules are likely to take predominantly end-on orientation due to the limitation on available binding sites on GO, thereby resulting in an increase in the fluidity of HSA layer (higher magnitude of  $\Delta D/\Delta f$ ). This transition from side-on to end-on orientation has also been reported by Roach et al.<sup>67</sup> in

their study of the adsorption of fibrinogen, which has an elongated shape, on a hydrophobic surface.

### 3.3.6 HSA adsorption Reduced GO attachment to SLBs at pH 7

The influence of HSA coronas on the deposition of GO on SLBs was investigated at neutral pH condition. Note that we did not separate the hard-corona-coated GO from the protein solution and therefore the GO nanosheets were expected to be dressed with both hard and soft coronas. The rate of GO deposition on SLBs were similar at 30 and 150 mM NaCl (Figure 3.10), consistent with our previous work demonstrating that fast deposition of GO on DOPC SLBs was achieved at NaCl concentration higher than ca. 30 mM.<sup>21</sup> In the presence of HSA, the rates of deposition were reduced under both ionic strength conditions, but the extent of reduction was much greater at 30 mM than at 150 mM (Figure 3.10). This observation implies that the adsorbed HSA on GO had a more substantial impact on the interactions between GO and SLBs at 30 mM NaCl.

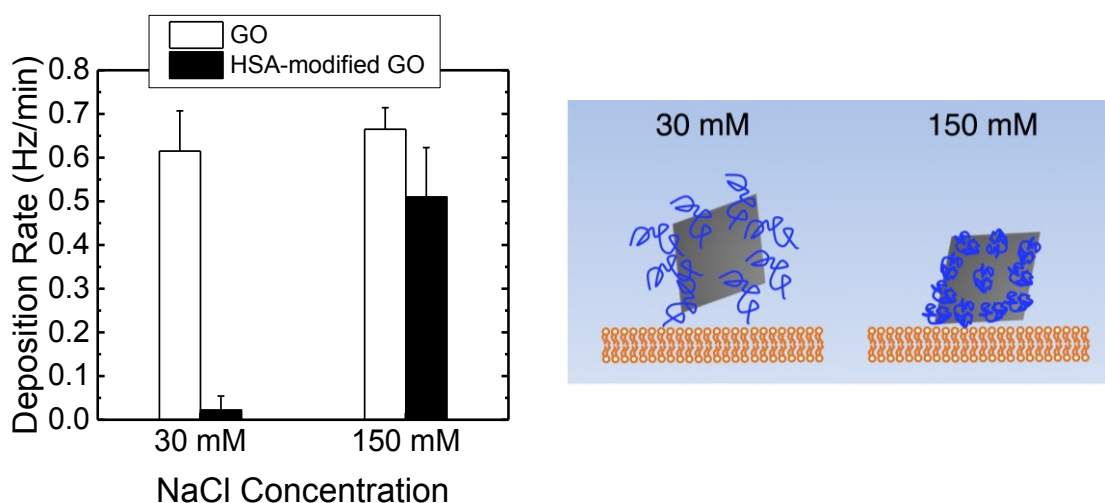


**Figure 3.10.** Effect of HSA adsorption on the deposition of GO on DOPC supported lipid bilayers at pH 7.0 under different ionic strengths. The cartoon illustrates the interaction of protein-coated GO with lipid bilayers.



Under both 30 and 150 mM NaCl, the average hydrodynamic size of GO was similar in the absence and presence of HSA over the course of the deposition experiment (Figure 3.11a). Meanwhile, the magnitude of EPs of GO was not significantly increased in the presence of HSA under both conditions (Figure 3.11b). Therefore, the inhibition of GO deposition by HSA adsorption at 30 and 150 mM NaCl was probably not due to the change in the aggregation behavior of GO or the enhancement in the surface charge of GO.

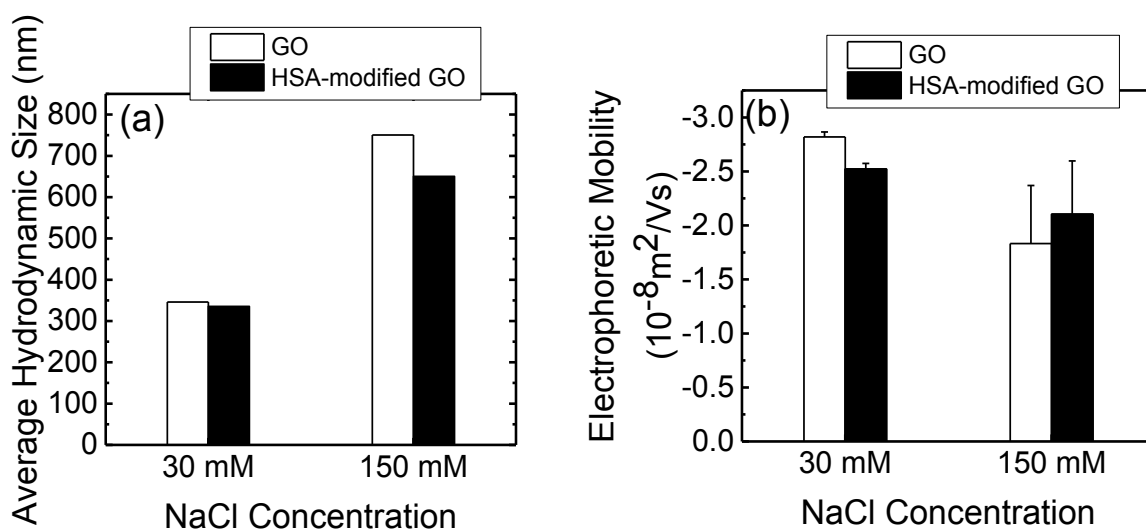


**Figure 3.11.** (a) Average hydrodynamic diameter of GO and HSA-modified GO during the initial 20 min of aggregation at 30 and 150 mM NaCl, pH 7.0. (b) Electrophoretic mobilities of GO and HSA-modified GO at 30 and 150 mM NaCl, pH 7.0.

As shown in Figure 3.5c, the HSA layer on GO at 30 mM was more fluid (hydrated) compared to that at 150 mM NaCl. In their study on the deposition of humic matter-coated colloids on quartz sand, Amirbahman and Olson<sup>68, 69</sup> postulated that the magnitude of steric repulsion between the colloids and the sand was directly dependent upon the conformations of the adsorbed polymers. A more hydrated HSA layer is expected to impart more steric (or

electrosteric) repulsion between HSA-coated GO and SLB, thereby inhibiting the deposition of GO on SLB more significantly.

### **3.3.7 Implications**

In order to better understand the formation and conformation of protein coronas on GO, the adsorption of HSA on GO was investigated under biologically relevant conditions. Our results show that the ionic strength and pH conditions as well as presence of calcium ions in the media had key influences on both the HSA-GO binding strength and the conformations of the hard coronas on GO. Higher ionic strength (e.g., blood compared to saliva)<sup>70</sup> can lead to enhanced binding of HSA to GO and more compact protein coronas on GO. Under acidic conditions (such as in gastric fluids), the coronas on GO are expected to be highly hydrated due to the conformational changes of proteins. These findings will provide fundamental insights into the dynamic changes of protein coronas when GO is transported from one biological compartment to another. We also show that the attachment of GO to lipid bilayers was reduced upon being coated by protein coronas, with a higher degree of reduction observed with more fluid (hydrated) protein coronas. Therefore, the hemolytic activity of GO<sup>10</sup> may be mitigated by protein coronas to varying degrees depending upon the corona conformations. Given the complexity of biological media, the coronas formed on nanoparticle surfaces often include multiple components (e.g., fatty acids, lipids, proteins)<sup>71</sup> and undergo dynamic nanoparticle-biomolecule association and dissociation.<sup>14</sup> Further investigations that involve the use of more realistic biological media are warranted to allow for a holistic understanding of the biological impacts of GO.

### 3.4 References

1. Loh, K. P.; Bao, Q. L.; Eda, G.; Chhowalla, M., Graphene oxide as a chemically tunable platform for optical applications. *Nature Chem.* **2010**, *2*, (12), 1015-1024.
2. Dikin, D. A.; Stankovich, S.; Zimney, E. J.; Piner, R. D.; Dommett, G. H. B.; Evmenenko, G.; Nguyen, S. T.; Ruoff, R. S., Preparation and characterization of graphene oxide paper. *Nature* **2007**, *448*, (7152), 457-460.
3. Dreyer, D. R.; Park, S.; Bielawski, C. W.; Ruoff, R. S., The chemistry of graphene oxide. *Chem. Soc. Rev.* **2010**, *39*, (1), 228-40.
4. Liu, S. B.; Zeng, T. H.; Hofmann, M.; Burcombe, E.; Wei, J.; Jiang, R. R.; Kong, J.; Chen, Y., Antibacterial Activity of Graphite, Graphite Oxide, Graphene Oxide, and Reduced Graphene Oxide: Membrane and Oxidative Stress. *ACS Nano* **2011**, *5*, (9), 6971-6980.
5. Xu, J. J.; Wang, K.; Zu, S. Z.; Han, B. H.; Wei, Z. X., Hierarchical Nanocomposites of Polyaniline Nanowire Arrays on Graphene Oxide Sheets with Synergistic Effect for Energy Storage. *ACS Nano* **2010**, *4*, (9), 5019-5026.
6. Perreault, F.; Fonseca de Faria, A.; Elimelech, M., Environmental applications of graphene-based nanomaterials. *Chem. Soc. Rev.* **2015**, *44*, (16), 5861-96.
7. Dong, H. F.; Gao, W. C.; Yan, F.; Ji, H. X.; Ju, H. X., Fluorescence Resonance Energy Transfer between Quantum Dots and Graphene Oxide for Sensing Biomolecules. *Anal. Chem.* **2010**, *82*, (13), 5511-5517.
8. Sun, X. M.; Liu, Z.; Welsher, K.; Robinson, J. T.; Goodwin, A.; Zaric, S.; Dai, H. J., Nano-Graphene Oxide for Cellular Imaging and Drug Delivery. *Nano Res* **2008**, *1*, (3), 203-212.
9. Liu, Z.; Robinson, J. T.; Sun, X. M.; Dai, H. J., PEGylated nano-graphene oxide for delivery of water-insoluble cancer drugs. *J. Am. Chem. Soc.* **2008**, *130*, (33), 10876-10877.
10. Liao, K. H.; Lin, Y. S.; Macosko, C. W.; Haynes, C. L., Cytotoxicity of Graphene Oxide and Graphene in Human Erythrocytes and Skin Fibroblasts. *ACS Appl. Mater. Interfaces* **2011**, *3*, (7), 2607-2615.
11. Akhavan, O.; Ghaderi, E.; Akhavan, A., Size-dependent genotoxicity of graphene nanoplatelets in human stem cells. *Biomaterials* **2012**, *33*, (32), 8017-8025.
12. Lynch, I.; Dawson, K. A., Protein-nanoparticle interactions. *Nano Today* **2008**, *3*, (1-2), 40-47.
13. Lundqvist, M.; Stigler, J.; Elia, G.; Lynch, I.; Cedervall, T.; Dawson, K. A., Nanoparticle size and surface properties determine the protein corona with possible implications for biological impacts. *Proc. Natl. Acad. Sci. U. S. A.* **2008**, *105*, (38), 14265-14270.
14. Nel, A. E.; Madler, L.; Velegol, D.; Xia, T.; Hoek, E. M. V.; Somasundaran, P.; Klaessig, F.; Castranova, V.; Thompson, M., Understanding biophysicochemical interactions at the nano-bio interface. *Nat. Mater.* **2009**, *8*, (7), 543-557.
15. Monopoli, M. P.; Aberg, C.; Salvati, A.; Dawson, K. A., Biomolecular coronas provide the biological identity of nanosized materials. *Nat. Nanotechnol.* **2012**, *7*, (12), 779-786.
16. Lesniak, A.; Fenaroli, F.; Monopoli, M. R.; Aberg, C.; Dawson, K. A.; Salvati, A., Effects of the Presence or Absence of a Protein Corona on Silica Nanoparticle Uptake and Impact on Cells. *ACS Nano* **2012**, *6*, (7), 5845-5857.

17. Linse, S.; Cabaleiro-Lago, C.; Xue, W. F.; Lynch, I.; Lindman, S.; Thulin, E.; Radford, S. E.; Dawson, K. A., Nucleation of protein fibrillation by nanoparticles. *Proc. Natl. Acad. Sci. U. S. A.* **2007**, *104*, (21), 8691-8696.
18. Chong, Y.; Ge, C. C.; Yang, Z. X.; Garate, J. A.; Gu, Z. L.; Weber, J. K.; Liu, J. J.; Zhou, R. H., Reduced Cytotoxicity of Graphene Nanosheets Mediated by Blood-Protein Coating. *ACS Nano* **2015**, *9*, (6), 5713-5724.
19. Kenry; Loh, K. P.; Lim, C. T., Molecular interactions of graphene oxide with human blood plasma proteins. *Nanoscale* **2016**, *8*, (17), 9425-9441.
20. Aguanno, J. J.; Ladenson, J. H., Influence of Fatty-Acids on the Binding of Calcium to Human-Albumin - Correlation of Binding and Conformation Studies and Evidence for Distinct Differences between Unsaturated Fatty-Acids and Saturated Fatty-Acids. *J. Biol. Chem.* **1982**, *257*, (15), 8745-8748.
21. Liu, X.; Chen, K. L., Interactions of Graphene Oxide with Model Cell Membranes: Probing Nanoparticle Attachment and Lipid Bilayer Disruption. *Langmuir* **2015**, *31*, (44), 12076-86.
22. Rixman, M. A.; Dean, D.; Macias, C. E.; Ortiz, C., Nanoscale intermolecular interactions between human serum albumin and alkanethiol self-assembled monolayers. *Langmuir* **2003**, *19*, (15), 6202-6218.
23. Hook, F.; Voros, J.; Rodahl, M.; Kurrat, R.; Boni, P.; Ramsden, J. J.; Textor, M.; Spencer, N. D.; Tengvall, P.; Gold, J.; Kasemo, B., A comparative study of protein adsorption on titanium oxide surfaces using in situ ellipsometry, optical waveguide lightmode spectroscopy, and quartz crystal microbalance/dissipation. *Colloid Surface B* **2002**, *24*, (2), 155-170.
24. Latour, R. A., The Langmuir isotherm: A commonly applied but misleading approach for the analysis of protein adsorption behavior. *J Biomed Mater Res A* **2015**, *103*, (3), 949-958.
25. Norde, W., Adsorption of Proteins from Solution at the Solid-Liquid Interface. *Adv. Colloid Interface Sci.* **1986**, *25*, (4), 267-340.
26. Zhu, D. Q.; Pignatello, J. J., Characterization of aromatic compound sorptive interactions with black carbon (charcoal) assisted by graphite as a model. *Environ. Sci. Technol.* **2005**, *39*, (7), 2033-2041.
27. Benjamin, M. M.; Lawler, D. F., *Water quality engineering: physical/chemical treatment processes*. John Wiley & Sons: 2013.
28. Yi, P.; Chen, K. L., Influence of surface oxidation on the aggregation and deposition kinetics of multiwalled carbon nanotubes in monovalent and divalent electrolytes. *Langmuir* **2011**, *27*, (7), 3588-99.
29. Qu, X. L.; Alvarez, P. J. J.; Li, Q. L., Impact of Sunlight and Humic Acid on the Deposition Kinetics of Aqueous Fullerene Nanoparticles (nC(60)). *Environ. Sci. Technol.* **2012**, *46*, (24), 13455-13462.
30. Sugio, S.; Kashima, A.; Mochizuki, S.; Noda, M.; Kobayashi, K., Crystal structure of human serum albumin at 2.5 angstrom resolution. *Protein Eng.* **1999**, *12*, (6), 439-446.
31. Sauerbrey, G., Verwendung Von Schwingquarzen Zur Wagung Dunner Schichten Und Zur Mikrowagung. *Zeitschrift Fur Physik* **1959**, *155*, (2), 206-222.
32. Rodahl, M.; Hook, F.; Krozer, A.; Brzezinski, P.; Kasemo, B., Quartz-Crystal Microbalance Setup for Frequency and Q-Factor Measurements in Gaseous and Liquid Environments. *Rev. Sci. Instrum.* **1995**, *66*, (7), 3924-3930.

33. Reviakine, I.; Johannsmann, D.; Richter, R. P., Hearing What You Cannot See and Visualizing What You Hear: Interpreting Quartz Crystal Microbalance Data from Solvated Interfaces. *Anal. Chem.* **2011**, *83*, (23), 8838-8848.
34. Hook, F.; Kasemo, B.; Nylander, T.; Fant, C.; Sott, K.; Elwing, H., Variations in coupled water, viscoelastic properties, and film thickness of a Mefp-1 protein film during adsorption and cross-linking: A quartz crystal microbalance with dissipation monitoring, ellipsometry, and surface plasmon resonance study. *Anal. Chem.* **2001**, *73*, (24), 5796-5804.
35. Voinova, M. V.; Rodahl, M.; Jonson, M.; Kasemo, B., Viscoelastic acoustic response of layered polymer films at fluid-solid interfaces: Continuum mechanics approach. *Phys. Scr.* **1999**, *59*, (5), 391-396.
36. Yi, P.; Chen, K. L., Interaction of Multiwalled Carbon Nanotubes with Supported Lipid Bilayers and Vesicles as Model Biological Membranes. *Environ. Sci. Technol.* **2013**, *47*, (11), 5711-5719.
37. Stankovich, S.; Dikin, D. A.; Piner, R. D.; Kohlhaas, K. A.; Kleinhammes, A.; Jia, Y.; Wu, Y.; Nguyen, S. T.; Ruoff, R. S., Synthesis of graphene-based nanosheets via chemical reduction of exfoliated graphite oxide. *Carbon* **2007**, *45*, (7), 1558-1565.
38. de Kerchove, A. J.; Elimelech, M., Structural growth and viscoelastic properties of adsorbed alginate layers in monovalent and divalent salts. *Macromolecules* **2006**, *39*, (19), 6558-6564.
39. Nguyen, T. H.; Elimelech, M., Plasmid DNA adsorption on silica: Kinetics and conformational changes in monovalent and divalent salts. *Biomacromolecules* **2007**, *8*, (1), 24-32.
40. Norde, W.; Lyklema, J., Thermodynamics of Protein Adsorption - Theory with Special Reference to the Adsorption of Human-Plasma Albumin and Bovine Pancreas Ribonuclease at Polystyrene Surfaces. *J. Colloid Interface Sci.* **1979**, *71*, (2), 350-366.
41. Gianazza, E.; Frigerio, A.; Astruategori, S.; Righetti, P. G., The Behavior of Serum-Albumin Upon Isoelectric-Focusing on Immobilized Ph Gradients. *Electrophoresis* **1984**, *5*, (5), 310-312.
42. Ortega-Vinuesa, J. L.; Tengvall, P.; Lundstrom, I., Molecular packing of HSA, IgG, and fibrinogen adsorbed on silicon by AFM imaging. *Thin Solid Films* **1998**, *324*, (1-2), 257-273.
43. Langer, K.; Balthasar, S.; Vogel, V.; Dinauer, N.; von Briesen, H.; Schubert, D., Optimization of the preparation process for human serum albumin (HSA) nanoparticles. *Int. J. Pharm.* **2003**, *257*, (1-2), 169-180.
44. Robertson, W. G., Measurement of Ionized Calcium in Biological Fluids. *Clin. Chim. Acta* **1969**, *24*, (1), 149-157.
45. Brini M, Ottolini D, Cali T, Carafoli E (2013). "Chapter 4. Calcium in Health and Disease". In Sigel A, Helmut RK. Interrelations between Essential Metal Ions and Human Diseases. Metal Ions in Life Sciences. 13. Springer. pp. 81-137.
46. Saroff, H.; Lewis, M., The binding of calcium ions to serum albumin. *The Journal of Physical Chemistry* **1963**, *67*, (6), 1211-1216.
47. Xiong, Y. L. L., Influence of pH and Ionic Environment on Thermal Aggregation of Whey Proteins. *J. Agric. Food Chem.* **1992**, *40*, (3), 380-384.
48. Fordtran, J. S.; Locklear, T. W., Ionic Constituents and Osmolality of Gastric and Small-Intestinal Fluids after Eating. *Am J Dig Dis* **1966**, *11*, (7), 503-&.

49. Fallingborg, J., Intraluminal pH of the human gastrointestinal tract. *Danish Medical Bulletin* **1999**, *46*, (3), 183-196.
50. Hermansen, L.; Osnes, J. B., Blood and Muscle Ph after Maximal Exercise in Man. *J. Appl. Physiol.* **1972**, *32*, (3), 304-+.
51. Oliva, F. Y.; Avalle, L. B.; Camara, O. R.; De Pauli, C. P., Adsorption of human serum albumin (HSA) onto colloidal TiO<sub>2</sub> particles, Part I. *J. Colloid Interface Sci.* **2003**, *261*, (2), 299-311.
52. Jones, K. L.; O'Melia, C. R., Protein and humic acid adsorption onto hydrophilic membrane surfaces: effects of pH and ionic strength. *J. Membr. Sci.* **2000**, *165*, (1), 31-46.
53. Koutsoukos, P. G.; Norde, W.; Lyklema, J., Protein Adsorption on Hematite (Alpha-Fe<sub>2</sub>O<sub>3</sub>) Surfaces. *J. Colloid Interface Sci.* **1983**, *95*, (2), 385-397.
54. Norde, W.; Lyklema, J., Adsorption of Human-Plasma Albumin and Bovine Pancreas Ribonuclease at Negatively Charged Polystyrene Surfaces .1. Adsorption Isotherms. Effects of Charge, Ionic-Strength, and Temperature. *J. Colloid Interface Sci.* **1978**, *66*, (2), 257-265.
55. Dockal, M.; Carter, D. C.; Ruker, F., Conformational transitions of the three recombinant domains of human serum albumin depending on pH. *J. Biol. Chem.* **2000**, *275*, (5), 3042-3050.
56. Rosenoer, V. M.; Oratz, M.; Rothschild, M. A., *Albumin: Structure, function and uses*. Elsevier: 2014.
57. Tsai, D. H.; DelRio, F. W.; Keene, A. M.; Tyner, K. M.; MacCuspie, R. I.; Cho, T. J.; Zachariah, M. R.; Hackley, V. A., Adsorption and Conformation of Serum Albumin Protein on Gold Nanoparticles Investigated Using Dimensional Measurements and in Situ Spectroscopic Methods. *Langmuir* **2011**, *27*, (6), 2464-2477.
58. Leonard, W. J.; Foster, J. F., Changes in optical rotation in the acid transformations of plasma albumin. Evidence for the contribution of tertiary structure to rotatory behavior. *J. Biol. Chem.* **1961**, *236*, (10), 2662-2669.
59. Bingen, P.; Wang, G.; Steinmetz, N. F.; Rodahl, M.; Richter, R. P., Solvation Effects in the Quartz Crystal Microbalance with Dissipation Monitoring Response to Biomolecular Adsorption. A Phenomenological Approach. *Anal. Chem.* **2008**, *80*, (23), 8880-8890.
60. Carton, I.; Brisson, A. R.; Richter, R. P., Label-Free Detection of Clustering of Membrane-Bound Proteins. *Anal. Chem.* **2010**, *82*, (22), 9275-9281.
61. Belegriou, S.; Mannelli, I.; Lisboa, P.; Bretagnol, F.; Valsesia, A.; Ceccone, G.; Colpo, P.; Rauscher, H.; Rossi, F., pH-dependent immobilization of proteins on surfaces functionalized by plasma-enhanced chemical vapor deposition of poly(acrylic acid)- and poly(ethylene oxide)-like films. *Langmuir* **2008**, *24*, (14), 7251-7261.
62. Hook, F.; Rodahl, M.; Kasemo, B.; Brzezinski, P., Structural changes in hemoglobin during adsorption to solid surfaces: Effects of pH, ionic strength, and ligand binding. *Proc. Natl. Acad. Sci. U. S. A.* **1998**, *95*, (21), 12271-12276.
63. Norde, W., Driving forces for protein adsorption at solid surfaces. *Macromol. Symp.* **1996**, *103*, 5-18.
64. Israelachvili, J. N., *Intermolecular and surface forces: revised third edition*. Academic press: 2011.
65. McAllister, M. J.; Li, J. L.; Adamson, D. H.; Schniepp, H. C.; Abdala, A. A.; Liu, J.; Herrera-Alonso, M.; Milius, D. L.; Car, R.; Prud'homme, R. K.; Aksay, I. A., Single sheet functionalized graphene by oxidation and thermal expansion of graphite. *Chem. Mater.* **2007**, *19*, (18), 4396-4404.

66. Sander, M.; Madliger, M.; Schwarzenbach, R. P., Adsorption of Transgenic Insecticidal Cry1Ab Protein to SiO<sub>2</sub>. 1. Forces Driving Adsorption. *Environ. Sci. Technol.* **2010**, *44*, (23), 8870-8876.
67. Roach, P.; Farrar, D.; Perry, C. C., Interpretation of protein adsorption: Surface-induced conformational changes. *J. Am. Chem. Soc.* **2005**, *127*, (22), 8168-8173.
68. Amirbahman, A.; Olson, T. M., The Role of Surface Conformations in the Deposition Kinetics of Humic Matter-Coated Colloids in Porous-Media. *Colloid Surface A* **1995**, *95*, (2-3), 249-259.
69. Amirbahman, A.; Olson, T. M., Transport of Humic Matter-Coated Hematite in Packed-Beds. *Environ. Sci. Technol.* **1993**, *27*, (13), 2807-2813.
70. Macakova, L.; Yakubov, G. E.; Plunkett, M. A.; Stokes, J. R., Influence of ionic strength on the tribological properties of pre-adsorbed salivary films. *Tribol Int* **2011**, *44*, (9), 956-962.
71. Docter, D.; Westmeier, D.; Markiewicz, M.; Stolte, S.; Knauer, S. K.; Stauber, R. H., The nanoparticle biomolecule corona: lessons learned - challenge accepted? *Chem. Soc. Rev.* **2015**, *44*, (17), 6094-6121.

**Chapter 4. Aggregation and Interactions of  
Chemical Mechanical Planarization Nanoparticles  
with Model Biological Membranes: Role of  
Phosphate Adsorption<sup>1</sup>**

---

<sup>1</sup> This chapter has been published as: Liu, X. T. and Chen, K. L., Aggregation and Interactions of Chemical Mechanical Planarization Nanoparticles with Model Biological Membranes: Role of Phosphate Adsorption, *Environmental Science: Nano*, 2016, 3, 146–156. DOI: 10.1039/C5EN00176E.



## 4.1 Introduction

Chemical mechanical planarization (CMP) is a key process in the semiconductor industry for the production of integrated circuit devices.<sup>1</sup> In CMP processes, slurries of abrasive particles, including SiO<sub>2</sub>, CeO<sub>2</sub>, and Al<sub>2</sub>O<sub>3</sub>, are employed to planarize wafers through a combination of mechanical abrasion and chemical etching.<sup>2</sup> The planarized wafers are subsequently rinsed with ultra-pure water, resulting in the generation of CMP wastewater.<sup>3, 4</sup> Although CMP wastewaters are generally subjected to on-site wastewater treatment (e.g., electrocoagulation<sup>5</sup> and microfiltration<sup>6</sup>) and/or municipal biological wastewater treatment, the wastewater effluent from municipal wastewater treatment plants still contains some unremoved CMP NPs which can be discharged, together with the treated effluent, into surface waters.<sup>7</sup> In their study on the removal efficiency of CeO<sub>2</sub> NPs by a model wastewater treatment plant, Limbach et al.<sup>8</sup> reported that about 6 wt % of the added CeO<sub>2</sub> NPs was found in the outflow of the model plant. The release of CMP NPs into the natural environment potentially poses a threat to the ecosystem and human health. In addition to the risks associated with the environmental release of CMP NPs, the exposure of workers to CMP NPs at the workplace may give rise to health risk concerns.<sup>9, 10</sup>

There have been extensive studies concerning the toxicity of SiO<sub>2</sub>, CeO<sub>2</sub>, and Al<sub>2</sub>O<sub>3</sub> NPs. The SiO<sub>2</sub> NPs used in CMP processes mainly include colloidal silica (*c*-SiO<sub>2</sub>) and fumed silica (*f*-SiO<sub>2</sub>).<sup>7</sup> Colloidal SiO<sub>2</sub> is synthesized through the hydrolysis and condensation of a Si precursor (e.g., silicon alkoxide),<sup>11</sup> while fumed SiO<sub>2</sub> is produced by pyrolysis of silicon tetrachloride (SiCl<sub>4</sub>) at high temperatures (1800 °C).<sup>12, 13</sup> It has been reported that *f*-SiO<sub>2</sub> has a greater ability than *c*-SiO<sub>2</sub> to generate hydroxyl radicals and cause red blood cells (RBCs) to undergo lysis due to their strained three-membered rings and

chainlike aggregate structure.<sup>14</sup> The CeO<sub>2</sub> NPs used in CMP processes are made from high temperature calcination (> 300 °C).<sup>7</sup> CeO<sub>2</sub> NPs have been shown to induce oxidative stress in human cancer cells and subsequently result in the damage of cell membranes.<sup>15</sup> Finally, Al<sub>2</sub>O<sub>3</sub> NPs can be produced through dehydration of  $\gamma$ -AlOOH (boehmite) at high temperatures (500–700 °C).<sup>16</sup> Previous studies have reported that Al<sub>2</sub>O<sub>3</sub> NPs can show inhibitory effect on human bronchial epithelial cells and cause hemolysis of RBCs.<sup>17, 18</sup>

While the mechanisms for the cytotoxicity of different classes of nanomaterials are still under investigation, studies have shown that the direct association of NPs with cell membranes is often a critical step that precedes the subsequent biological responses.<sup>19, 20</sup> The attachment of NPs on cell membranes can also result in damage of the membranes.<sup>20</sup> Therefore, a detailed assessment of the interactions of CMP NPs with cell membranes is expected to improve our understanding on the biological effects of these nanomaterials. Due to the inherent heterogeneity and diversity of cell membranes, the use of model (or artificial) cell membranes that are composed of lipid bilayers is an attractive approach to gain fundamental insights into the interactions between NPs and cell membranes.<sup>20-22</sup> A common approach to investigate the attachment of NPs to cell membranes involves the employment of supported lipid bilayers (SLBs) to evaluate the NP's propensity to attach on lipid bilayers.<sup>23, 24</sup> Since a lipid bilayer is a key component of cell membranes, the use of SLBs will enable the elucidation of the nonspecific interactions between NPs and cell membranes at the nano-bio interface.<sup>19, 20, 24-28</sup> A recent study utilizing model membranes showed that the presence of proteins can decrease the attachment of NPs to membranes and hence reduce the uptake of NPs by human epithelial cells.<sup>29</sup> Additionally, lipid bilayer vesicles have been used as model cell membranes to probe the propensity of NPs to disrupt lipid bilayers.<sup>20, 30-32</sup>

The objective of this work is to investigate the interactions of model CMP NPs with model biological membranes which include SLBs and supported vesicular layers (SVLs). Since phosphate is a key constituent in biological fluids, such as human blood serum (0.81–1.45 mM) and saliva (5–14 mM),<sup>33</sup> the role of phosphate in these interactions will be studied. In addition, we will examine the aggregation behavior of CMP NPs in model biological media since the cellular uptake of NPs, as well as the subsequent biological responses, has been shown to be dependent on the aggregation state of the NPs.<sup>34, 35</sup> The results of this study will provide new insights into the nonspecific interactions of CMP NPs with cell membranes when they enter biological systems.

## **4.2 Materials and Methods**

### **4.2.1 CMP NP Suspensions**

Four model CMP NPs, namely, *c*-SiO<sub>2</sub>, *f*-SiO<sub>2</sub>, CeO<sub>2</sub>, and Al<sub>2</sub>O<sub>3</sub>, were provided by Cabot Microelectronics Corporation (Aurora, Illinois, USA) as slurries. These NP slurries are shared within a research consortium and have been extensively characterized.<sup>7</sup> Their physicochemical properties (including shape, size, crystalline structure, and surface charge) are presented in a recently published paper by Speed et al.<sup>7</sup> These slurries were maintained colloidally stable by pH adjustment and did not contain organic stabilizers.<sup>7</sup> Here, we highlight some of the properties of the CMP NPs reported by Speed et al.<sup>7</sup> Through transmission electron microscopy (TEM) imaging, the *c*-SiO<sub>2</sub> NPs were observed to be mostly spherical, while the *f*-SiO<sub>2</sub> NPs appeared irregular-shaped and fused together. X-ray diffraction (XRD) analysis showed that both *c*-SiO<sub>2</sub> and *f*-SiO<sub>2</sub> NPs had amorphous SiO<sub>2</sub> structures. The CeO<sub>2</sub> NPs were rectangular and XRD patterns of the CeO<sub>2</sub> slurry revealed the

cubic fluorite structure of the NPs.<sup>36</sup> Finally, the Al<sub>2</sub>O<sub>3</sub> NPs contained a broad range of particle sizes and XRD results indicated that the Al<sub>2</sub>O<sub>3</sub> NPs were  $\gamma$ -Al<sub>2</sub>O<sub>3</sub>.<sup>37</sup> The mean diameters of the *c*-SiO<sub>2</sub>, CeO<sub>2</sub>, and Al<sub>2</sub>O<sub>3</sub> NPs determined through TEM imaging were 36, 39, and 38 nm, respectively. The size of the *f*-SiO<sub>2</sub> NPs could not be determined through TEM due to their coalesced state. By employing dynamic light scattering (DLS), the hydrodynamic diameter of the *f*-SiO<sub>2</sub> NPs was determined to be ca. 148 nm. All slurries were used directly after being diluted in deionized (DI) water (18 M $\Omega$  cm, Millipore, MA) without further purification.

#### 4.2.2 Solution Chemistry

ACS-grade NaCl, NaH<sub>2</sub>PO<sub>4</sub>, Na<sub>2</sub>HPO<sub>4</sub>, and NaHCO<sub>3</sub> were used for the preparation of stock solutions. All stock solutions were filtered using 0.1  $\mu$ m polyvinylidene fluoride syringe filters (Millipore, MA). The pH of the diluted CMP dispersions was maintained at 7.4 with either a phosphate (1.13 mM NaH<sub>2</sub>PO<sub>4</sub> and 3.87 mM Na<sub>2</sub>HPO<sub>4</sub>) or bicarbonate (0.4 mM NaHCO<sub>3</sub>) buffer. Three buffers containing *N*-(2-hydroxyethyl)-piperazine-*N'*-(2-ethanesulfonic acid) (HEPES, Sigma-Aldrich) were also used in the experiments using a quartz crystal microbalance with dissipation monitoring (QCM-D). They are denoted as Buffer A (10 mM HEPES, 150 mM NaCl, pH adjusted to 7.4), Buffer B (10 mM HEPES, 100 mM NaCl, with unadjusted pH ca. 5.5), and Buffer C (20 mM HEPES, 150 mM NaCl, pH adjusted to 7.4).

#### 4.2.3 Electrophoretic Mobility Measurements

The electrophoretic mobilities (EPMs) of the CMP NPs were measured (ZetaPALS, Brookhaven Instruments Corp., Holtsville, NY) over a range of NaCl concentrations in either

phosphate or bicarbonate buffer at pH 7.4. The concentrations of the CMP NPs used in the EPM measurements are presented in Table 4.1. Three samples were measured at each electrolyte concentration. For most of the experimental conditions, ten measurements were conducted for each sample. At high NaCl concentrations, only five measurements were conducted in order to minimize the effect of NP aggregation.

**Table 4.1.** Concentrations of CMP NPs used in electrophoretic mobility measurements

Name	<i>c</i> -SiO <sub>2</sub>	<i>f</i> -SiO <sub>2</sub>	CeO <sub>2</sub>	Al <sub>2</sub> O <sub>3</sub>
Dilution factor	100	1,000	1,000	1,000
Concentration	270 mg Si L <sup>-1</sup>	50 mg Si L <sup>-1</sup>	9.6 mg Ce L <sup>-1</sup>	29 mg Al L <sup>-1</sup>

#### 4.2.4 Phosphate Adsorption by CMP NPs

The CMP NPs in the stock suspensions were washed before being used for the phosphate adsorption experiments. For the *f*-SiO<sub>2</sub>, CeO<sub>2</sub>, and Al<sub>2</sub>O<sub>3</sub> NPs, 50 mL of each NP suspension was centrifuged at 3,650 *g* (Beckman Coulter, CA, 4,000 rpm) for 3 h. 90 % of the supernatant was carefully decanted and replaced with an equal volume of deionized (DI) water. This cleaning process was repeated two times. For the *c*-SiO<sub>2</sub> NPs, a similar procedure was used, except that the centrifugation was performed at 12,000 *g* (Eppendorf, NY, 13,375 rpm) for 40 min and the cleaning process was repeated four times. The concentrations of the *c*-SiO<sub>2</sub>, *f*-SiO<sub>2</sub>, CeO<sub>2</sub>, and Al<sub>2</sub>O<sub>3</sub> NPs in the washed suspensions were determined to be 22.5 ± 1.3, 46.3 ± 7.8, 5.5 ± 0.1, and 19.4 ± 0.3 g/L, respectively, by gravimetric analysis.

Adsorption experiments were conducted in glass scintillation vials at room temperature. These experiments were conducted at an initial phosphate concentration of 100

$\mu\text{M}$ , 1 g/L NPs, 1 mM NaCl, and pH 7.4. Two duplicate adsorption reactors were set up for each type of NPs. After the suspension was stirred on a magnetic stir plate at 400 rpm for 10 min, aliquots of the suspension were drawn and centrifuged at 12,000 g (Eppendorf, NY, 13,375 rpm) for 40 min. The concentration of phosphate in the supernatant was determined using the colorimetric technique of Murphy and Riley.<sup>38</sup> Briefly, 0.06 mL of 11 N  $\text{H}_2\text{SO}_4$  was added to 3 mL of the supernatant, followed by the addition of 0.24 mL of 8 g/L ammonium molybdate (Fluka) and 0.2 g/L antimony potassium tartrate (Sigma-Aldrich). The resulting solution was mixed to allow for the formation of an antimony-phosphomolybdate complex. Next, 0.12 mL of 60 g/L ascorbic acid (Sigma-Aldrich) was added to the solution to reduce the complex to a blue-colored complex. The absorbance of the solution was measured with a UV/Vis spectrophotometer (Shimadzu, UV-1800) at 650 nm. A linear calibration curve was obtained over the range of phosphate concentration of 0–25  $\mu\text{M}$ .

Control experiments were also performed on the four CMP suspensions without the addition of phosphate. Two duplicate control reactors were set up for each NP. Each control reactor contains 1 g/L CMP NPs and 1 mM NaCl. After 10 min of stirring, aliquots of the control suspensions were drawn, centrifuged, and measured in a similar manner as the NP-phosphate suspensions (described in the previous paragraph). The absorbance of the supernatants of the control suspensions at 650 nm was subtracted from that of the supernatants of the NP-phosphate suspensions. The concentrations of phosphate in the supernatants of NP-phosphate suspensions were determined using the calibration curve and the amount of phosphate adsorbed on the NPs was calculated through material balance (expressed as  $\mu\text{mol}$  phosphate/g NPs).

#### 4.2.5 Dynamic Light Scattering

Time-resolved dynamic light scattering (DLS) measurements were conducted with a light scattering unit to investigate the aggregation kinetics of four CMP NPs in phosphate and bicarbonate buffers. This unit consists of an argon laser with a wavelength of 488 nm (Lexel 95, Cambridge laser, CA), a photomultiplier tube mounted on a goniometer (BI-200SM, Brookhaven, NY), a digital correlator (BI-9000AT, Brookhaven, NY), and a thermostatted vat filled with an index-matching *cis*- and *trans*-mixture of decahydronaphthalene. The room temperature was maintained at 25 °C. New glass vials were soaked overnight in a cleaning solution (Extran MA01, Merck KGaA, Darmstadt, Germany), rinsed thoroughly with DI water, and dried in an oven under dust-free conditions prior to use. For each aggregation experiment, a predetermined amount of NaCl solution was introduced to a glass vial containing a diluted suspension of CMP NPs. The pH of the suspension was maintained at 7.4 with either phosphate or bicarbonate buffer, or adjusted to 1.0, 2.0, and 12.0 using 1 M HCl or NaOH. The total volume of the suspension was 1 mL. The suspension in the vial was briefly mixed using a vortex mixer. The vial was then inserted into the index-matching vat and the DLS measurements were started immediately.

All DLS measurements were performed at a scattering angle of 90° and each autocorrelation function was accumulated for 15 s. The intensity-weighted hydrodynamic diameters of the aggregates were derived through second-order cumulant analysis (Brookhaven software). The DLS measurements were performed over time periods of 10–50 min to allow for a large enough increase in the intensity-weighted hydrodynamic diameter for an accurate determination of the NP aggregation kinetics.

The early-stage aggregation kinetics of CMP NPs can be derived from time-resolved DLS measurements using eq 4.1.<sup>39, 40</sup>

$$k \propto \frac{1}{N_0} \left( \frac{dD_h(t)}{dt} \right)_{t \rightarrow 0} \quad (4.1)$$

where  $k$  is the aggregation rate constant,  $N_0$  is the initial primary particle concentration, and  $D_h(t)$  is the intensity-weighted hydrodynamic diameter at time  $t$ . Note that  $D_h(t)$  is calculated from the diffusion coefficient of the CMP NPs/aggregates and is equivalent to the diameter of a sphere that has the same diffusion coefficient as the CMP NPs/aggregates. The DLS technique has also been used to investigate the aggregation kinetics of other non-spherical colloids, such as nickel hydroxycarbonate,<sup>41</sup> carbon nanotubes,<sup>42</sup> and graphene oxide.<sup>43</sup> The NP concentrations used in the DLS experiments are presented in Table 4.2.

**Table 4.2.** Concentrations of CMP NPs used in dynamic light scattering measurements.

Name	<i>c</i> -SiO <sub>2</sub>	<i>f</i> -SiO <sub>2</sub>	CeO <sub>2</sub>	Al <sub>2</sub> O <sub>3</sub>
Dilution factor	1,000	25,000	5,000	25,000
Concentration	27 mg Si L <sup>-1</sup>	2 mg Si L <sup>-1</sup>	1.92 mg Ce L <sup>-1</sup>	1.16 mg Al L <sup>-1</sup>

For most NaCl concentrations employed in the DLS measurements, the initial aggregation rates were derived by performing linear least-squares regression in the early aggregation stage before the intensity-weighted hydrodynamic diameter reached 1.4  $D_h(0)$ .<sup>44</sup> At low NaCl concentrations, however, the hydrodynamic diameter failed to reach 1.4  $D_h(0)$  and the linear regressions were performed over the first 50 min of aggregation. The aggregation attachment efficiency,  $\alpha_A$ , was calculated to quantify the aggregation kinetics of the CMP NPs at different NaCl concentrations:<sup>40, 44</sup>



$$\alpha_A = \frac{k}{k_{fast}} = \frac{\frac{1}{N_0} \left( \frac{dD_h(t)}{dt} \right)_{t \rightarrow 0}}{\frac{1}{(N_0)_{fast}} \left( \frac{dD_h(t)}{dt} \right)_{t \rightarrow 0, fast}} \quad (4.2)$$

The terms with subscript “fast” refer to diffusion-limited conditions.

#### 4.2.6 Preparation of Vesicle Stock Suspensions

Two types of vesicles were used in the QCM-D experiments: 1) zwitterionic 1,2-dioleoyl-*sn*-glycero-3-phosphocholine (DOPC) vesicles for the formation of SLBs to investigate the propensity for CMP NPs to attach to lipid bilayers, and 2) DOPC vesicles encapsulated with carboxyfluorescein (CF) dye (to be referred to as CF-DOPC vesicles) to assess the disruption of lipid membranes by the NPs. For the preparation of DOPC vesicles, 0.2 mL of 25 g/L DOPC chloroform solution (Avanti Polar Lipids, Inc., Alabaster, AL) was dried in an Erlenmeyer flask using a gentle stream of ultrapure nitrogen gas. A DOPC thin film was formed at the bottom of the flask and the film was subjected to vacuum desiccation for at least 4 h. The DOPC lipids were then re-suspended in 5 mL Buffer A and the solution was magnetically stirred for ca. 30 min. To obtain unilamellar vesicles, the DOPC solution was extruded using a mini-extruder (Avanti Polar Lipids) through a 50-nm polycarbonate membrane (Whatman) for at least 15 times.<sup>45</sup> For the preparation of CF-DOPC vesicles, the aforementioned DOPC thin film was hydrated with a 100 mM CF solution prepared in Buffer C and was subsequently subjected to the same extrusion treatment.<sup>32</sup> All vesicle suspensions were stored in glass vials at 4 °C and used within four days after preparation.

#### 4.2.7 Quartz Crystal Microbalance with Dissipation Monitoring

The interactions of CMP NPs with DOPC SLBs and vesicles were studied using a QCM-D E4 setup (Biolin Scientific, Västra Frölunda, Sweden) that is equipped with four measurement chambers. Each chamber housed a 5 MHz quartz crystal sensor with either a silica-coated (QSX 303) or gold-coated (QSX 301) surface. The sensors were cleaned prior to the QCM-D experiments according to a protocol that was described in our previous paper.<sup>46</sup> The temperature inside the QCM-D chambers was maintained at 25 °C. The rate of frequency shift at the 3<sup>rd</sup> overtone,  $d\Delta f_{(3)}/dt$ , was used to quantify the deposition rates of GO on SLBs.<sup>46, 47</sup> Duplicate experiments were carried out for each condition.

For the deposition of CMP NPs on SLBs, a SLB was first formed on the surface of a silica-coated sensor using the method of Keller and Kasemo.<sup>48</sup> The sensor was rinsed with Buffer A until a stable baseline was achieved (i.e., frequency signal drifts of less than 0.2 Hz per 10 min). Following that, a 0.07 g/L DOPC vesicle suspension was flowed through the QCM-D chamber for ca. 5 min. The vesicles deposited on the silica surface and subsequently ruptured on the surface to form a SLB.<sup>48</sup> The formation of a DOPC SLB resulted in a characteristic frequency shift of  $-25 \pm 0.5$  Hz and a simultaneous dissipation shift of  $0.1 \times 10^{-6}$ .<sup>48</sup> After the SLB was formed, the chamber was rinsed with Buffer A for ca. 10 min to remove the unadsorbed vesicles. A NaCl solution with phosphate or bicarbonate buffer was then flowed through the measurement chamber to obtain a stable baseline, followed by the introduction of CMP NPs in the same solution chemistry to initiate the deposition process. The NP concentrations used in the QCM-D experiments are presented in Table 4.3. The flow rate was maintained at  $0.10 \pm 0.002$  mL/min using a

peristaltic pump (ISM935C, Ismatec SA, Zürich, Switzerland). This flow rate resulted in a laminar flow in the QCM-D chamber.<sup>47</sup>

**Table 4.3.** Concentrations of CMP NPs used in quartz crystal microbalance experiments.

Name	<i>c</i> -SiO <sub>2</sub>	<i>f</i> -SiO <sub>2</sub>	CeO <sub>2</sub>	Al <sub>2</sub> O <sub>3</sub>
Dilution factor	10,000	25,000	1,000	10,000
Concentration	2.7 mg Si L <sup>-1</sup>	2 mg Si L <sup>-1</sup>	9.6 mg Ce L <sup>-1</sup>	2.9 mg Al L <sup>-1</sup>

The deposition kinetics of CMP NPs on SLBs were quantified using the deposition attachment efficiency,  $\alpha_D$ , which can be calculated by normalizing the rate of frequency shift on SLBs to the rate under favorable condition obtained at the same solution chemistry:<sup>49, 50</sup>

$$\alpha_D = \frac{d\Delta f_3 / dt}{(d\Delta f_3 / dt)_{fav}} \quad (4.3)$$

The subscript “fav” refers to favorable deposition condition. For *c*-SiO<sub>2</sub>, *f*-SiO<sub>2</sub>, and CeO<sub>2</sub> NPs in both phosphate and bicarbonate buffers, as well as Al<sub>2</sub>O<sub>3</sub> NPs in phosphate buffer, the favorable deposition experiments were performed on silica sensors coated with positively charged poly-L-lysine (PLL).<sup>49, 51</sup> To prepare the PLL-coated sensors, PLL was diluted in Buffer B to a concentration of 0.01 g/L before the mixture was used to modify the silica crystals.<sup>49</sup> For Al<sub>2</sub>O<sub>3</sub> NPs in bicarbonate buffer, favorable deposition conditions were achieved by using bare silica surfaces since the Al<sub>2</sub>O<sub>3</sub> NPs are positively charged in bicarbonate buffer at pH 7.4 while silica is negatively charged.<sup>52</sup>

#### 4.2.8 Detection of Dye Leakage from Supported Vesicles

A supported CF-DOPC vesicular layer was formed on a gold-coated sensor in order to investigate the propensity for the CMP NPs to disrupt lipid membranes.<sup>46, 48, 53</sup> After a stable baseline was achieved by rinsing the sensor with Buffer C, a 0.05 g/L CF-DOPC

vesicle suspension was flowed through the chamber for ca. 30 min. The CF-DOPC vesicles deposited on the gold surface to form a SVL.<sup>48, 53</sup> The CF dye outside the vesicles was removed by rinsing the SVL with Buffer C for at least 2 h. Following the rinsing stage, a NaCl solution (150 mM NaCl, phosphate buffer, pH 7.4) was introduced into the chamber to achieve a stable baseline. Next, a CMP NP suspension prepared in the same solution chemistry was introduced into the chamber for 40 min. At the end of each experiment, the vesicles were exposed to a 32 mM Triton X-100 solution, a membrane solubilizer,<sup>54</sup> to induce the complete rupture of the deposited vesicles. The fluorescence of the outflow was measured using a spectrofluorometer (Horiba Jobin Yvon, France) at an excitation wavelength of 490 nm and an emission wavelength of 517 nm.

### 4.3 Results and Discussion

#### 4.3.1 Electrokinetic Properties of CMP NPs

The EPMS of the CMP NPs are presented in Figure 4.1a as a function of NaCl concentration in phosphate buffer at pH 7.4. As shown in the figure, all four NPs carried negative charge in the presence of phosphate. The magnitude of the EPMS for all four NPs decreased with an increase in NaCl concentration due to the screening of surface charge.<sup>55</sup> In our previous work,<sup>7</sup> we have measured the pH of zero point of charge (pH<sub>ZPC</sub>) of *c*-SiO<sub>2</sub>, *f*-SiO<sub>2</sub>, CeO<sub>2</sub>, and Al<sub>2</sub>O<sub>3</sub> NPs in the absence of phosphate to be below 2, 2, 8, and 10, respectively. These values are consistent with the pH<sub>ZPC</sub> values of silica (ca. 2),<sup>52, 56</sup> CeO<sub>2</sub> (6.0–8.5), and  $\gamma$ -Al<sub>2</sub>O<sub>3</sub> (7.6–9.3)<sup>57, 58</sup> reported in the literature. The negative charge of SiO<sub>2</sub> NPs at pH 7.4 in the presence of phosphate is consistent with the pH<sub>ZPC</sub> of silica.

Interestingly, in the presence of phosphate, the  $\text{CeO}_2$  and  $\text{Al}_2\text{O}_3$  NPs carried considerable negative charge at pH 7.4.

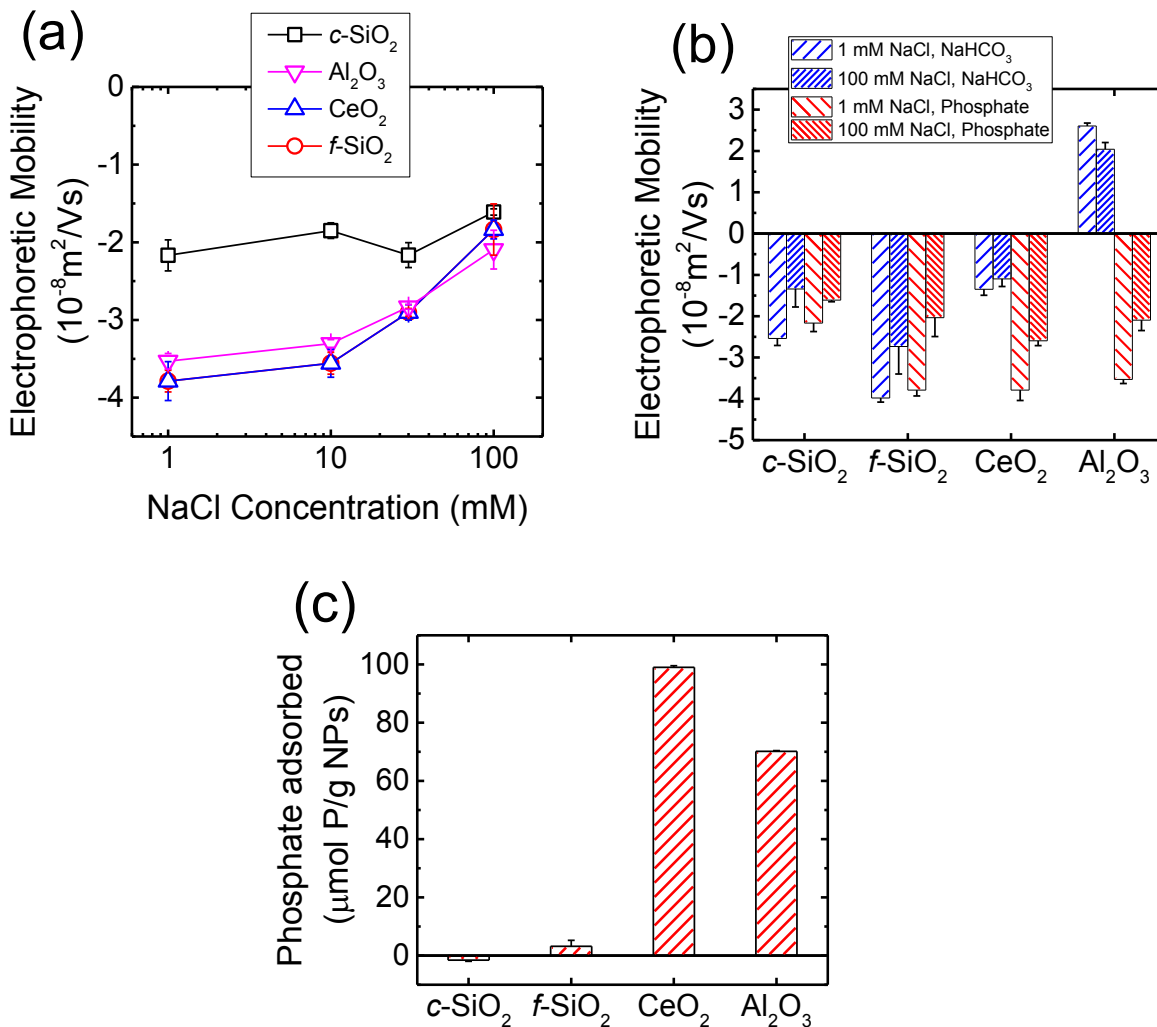


**Figure 4.1.** (a) EPMs of CMP NPs over a wide range of NaCl concentrations at pH 7.4 in phosphate buffer. (b) EPMs of CMP NPs at 1 and 100 mM NaCl and pH 7.4 in phosphate and bicarbonate buffer. The data in phosphate buffer was reproduced from Figure 1a for comparison. (c) Phosphate adsorption by CMP NPs within a time duration of 10 min. The adsorption experiments were conducted at an initial phosphate concentration of 100 μM, 1 g/L NPs, 1 mM NaCl, and pH 7.4. Error bars represent standard deviations.

The EPMS of the four CMP NPs were further measured in 1 and 100 mM NaCl in bicarbonate buffer (i.e., in the absence of phosphate) at pH 7.4 and the EPMS in the absence and presence of phosphate are compared in Figure 4.1b. In bicarbonate buffer, the *c*-SiO<sub>2</sub> and *f*-SiO<sub>2</sub> NPs were negatively charged, while the CeO<sub>2</sub> and Al<sub>2</sub>O<sub>3</sub> NPs carried slight negative charge and considerable positive charge, respectively. These results were consistent with the pHz<sub>P</sub>C values for SiO<sub>2</sub>, CeO<sub>2</sub>, and Al<sub>2</sub>O<sub>3</sub> that had been reported in the literature.<sup>52, 56-58</sup> For both *c*-SiO<sub>2</sub> and *f*-SiO<sub>2</sub> NPs, the EPMS in the two buffers at the same NaCl concentration was not statistically different (two tailed *t*-test, significant level of 0.05). In contrast, for CeO<sub>2</sub> and Al<sub>2</sub>O<sub>3</sub> NPs, their EPMS in the two buffers were significantly different. This discrepancy is likely due to the adsorption of the phosphate ions on the surface of CeO<sub>2</sub> and Al<sub>2</sub>O<sub>3</sub> NPs. In order to test this hypothesis, phosphate adsorption experiments were further conducted for the four NPs (Figure 4.1c). The amount of phosphate adsorbed on CeO<sub>2</sub> and Al<sub>2</sub>O<sub>3</sub> NPs over a time period of 10 min (expressed as μmol phosphate/g NPs) was one to two orders of magnitude higher than that on *f*-SiO<sub>2</sub> NPs (no adsorption detected on *c*-SiO<sub>2</sub> NPs). Since the densities of CeO<sub>2</sub> (ca. 7.3 g/cm<sup>3</sup>)<sup>59</sup> and Al<sub>2</sub>O<sub>3</sub> (ca. 3.9 g/cm<sup>3</sup>)<sup>60</sup> are both higher than that of amorphous SiO<sub>2</sub> (ca. 2.2 g/cm<sup>3</sup>)<sup>61</sup>, a more pronounced difference in phosphate adsorption on CeO<sub>2</sub> and Al<sub>2</sub>O<sub>3</sub> NPs versus SiO<sub>2</sub> NPs would be expected if the amount of adsorbed phosphate is expressed on a particle number basis. Therefore, the significant change in the EPMS of CeO<sub>2</sub> and Al<sub>2</sub>O<sub>3</sub> NPs was very likely due to the adsorption of phosphate on the NPs.

At pH 7.4, phosphate ( $pK_{a1} = 2.1$ ,  $pK_{a2} = 7.2$ ,  $pK_{a3} = 11.9$ ) mainly exists in the form of monovalent (H<sub>2</sub>PO<sub>4</sub><sup>-</sup>) and divalent (HPO<sub>4</sub><sup>2-</sup>) phosphate ions (calculated to be 39 and 61 %, respectively).<sup>52</sup> As shown in Figure 4.1b, the Al<sub>2</sub>O<sub>3</sub> NPs underwent charge reversal in the presence of phosphate. It has been shown through <sup>31</sup>P NMR measurements that phosphate

can adsorb to  $\gamma$ -Al<sub>2</sub>O<sub>3</sub> via both outer- and inner-sphere complexation.<sup>62</sup> Outer-sphere complexation occurs through the electrostatic attraction between the positively charged –AlOH<sub>2</sub><sup>+</sup> groups and negatively charged phosphate ions,<sup>62</sup> whereas inner-sphere complexation takes place through direct bond formation between the Al atom and the oxygen donor atoms in the phosphate ion.<sup>62, 63</sup> Hunter<sup>64</sup> reported that inner-spherically adsorbed ions have a higher propensity to reverse the sign of surface charge, whereas indifferent ions can only screen the surface charge. Therefore, inner-sphere complexation of phosphate is expected to be the primary mechanism for the reversal of surface charge of Al<sub>2</sub>O<sub>3</sub> NPs. For CeO<sub>2</sub> NPs which already carried a negative charge at pH 7.4 (Figure 4.1b), the enhancement of negative surface charge in the presence of phosphate, as observed elsewhere,<sup>65, 66</sup> was likely a result of the inner-sphere complexation between phosphate ions and the CeO<sub>2</sub> NPs.<sup>64</sup> For both SiO<sub>2</sub> NPs, the surface charges in the presence and absence of phosphate were not significantly different (Figure 4.1b), consistent with the negligible adsorption of phosphate on the SiO<sub>2</sub> NPs compared to that on CeO<sub>2</sub> and Al<sub>2</sub>O<sub>3</sub> NPs (Figure 4.1c).

#### 4.3.2 Stability of *c*-SiO<sub>2</sub> and *f*-SiO<sub>2</sub> NPs at pH 7.4

The aggregation profiles of the four CMP NPs at 150 mM NaCl and pH 7.4 in the presence and absence of phosphate are presented in Figure 4.2. This NaCl concentration was chosen because the ionic strength in physiological fluids is ca. 150 mM.<sup>19</sup> The hydrodynamic diameter of *c*-SiO<sub>2</sub> and *f*-SiO<sub>2</sub> NPs did not change significantly within a duration of 20 min, whereas CeO<sub>2</sub> and Al<sub>2</sub>O<sub>3</sub> NPs underwent appreciable aggregation. This observation shows that both SiO<sub>2</sub> NPs were considerably more stable than CeO<sub>2</sub> and Al<sub>2</sub>O<sub>3</sub> NPs at pH 7.4. Since phosphate ions do not adsorb favorably on both NPs, as discussed in

the previous section, they are not expected to be involved in the mechanisms for the elevated stability of the SiO<sub>2</sub> NPs.

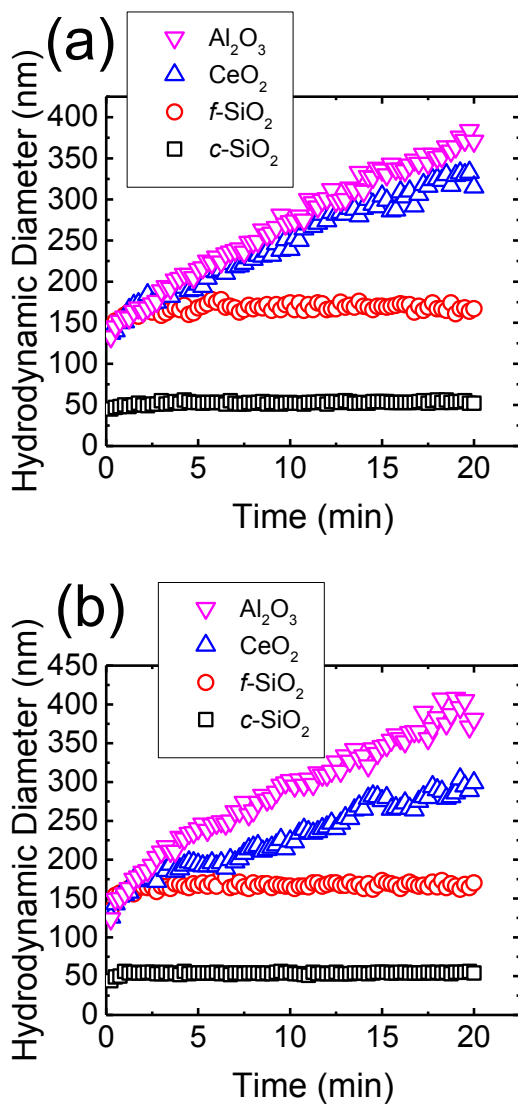


**Figure 4.2.** Aggregation profiles of four CMP NPs at 150 mM NaCl and pH 7.4 in (a) phosphate and (b) bicarbonate buffer.

In order to elucidate the mechanisms for the high stability of SiO<sub>2</sub> NPs at pH 7.4, aggregation experiments were further carried out at pH 2.0 (adjusted with 1 M HCl), which is the reported p*H*<sub>ZPC</sub> of SiO<sub>2</sub>.<sup>52, 56</sup> Thus, at pH 2.0, the electric double layer (EDL) repulsion



between the SiO<sub>2</sub> NPs was expected to be largely eliminated. As shown in Figure 4.3a, the *f*-SiO<sub>2</sub> NPs underwent considerable aggregation at pH 2.0 compared to at pH 7.4 (both in the presence and absence of phosphate). It can therefore be concluded that the elevated stability of *f*-SiO<sub>2</sub> NPs at pH 7.4 was due to the high surface charge that was not completely screened even at 150 mM NaCl.

In contrast to *f*-SiO<sub>2</sub> NPs, *c*-SiO<sub>2</sub> NPs were stable at pH 2.0 (Figure 4.3b). Additional aggregation experiments of *c*-SiO<sub>2</sub> NPs were carried out at pH 1.0 (data not shown) and no aggregation was observed, similar to at pH 2.0 and 7.4. The high stability of *c*-SiO<sub>2</sub> colloids at ca. pH 2 has been reported by different researchers.<sup>67-69</sup> The presence of a repulsive force between silica surfaces at short separation distances, in addition to EDL repulsion, has been detected through force measurements using atomic force microscopy and surface force apparatus.<sup>70, 71</sup> Israelachvili and co-workers<sup>71, 72</sup> proposed that a hairy layer of protruding silanol and silicic acid groups on silica surface was the origin of the repulsive force between SiO<sub>2</sub> colloids and also their stability in water. Borkovec and co-workers<sup>69</sup> reported that SiO<sub>2</sub> particles underwent fast aggregation at pH 12 which they attributed to the dissolution of the hairy layers at high pH conditions. The aggregation behavior of *c*-SiO<sub>2</sub> at pH 12 is presented in Figure 4.3c. In the absence of NaCl at pH 12, *c*-SiO<sub>2</sub> was stable, likely due to the EDL repulsion between the NPs. With the increase in NaCl concentration, the aggregation rates of the NPs increased and fast aggregation was achieved at 150 mM NaCl. This result supports the hypothesis that the presence of hairy layer on the surface of *c*-SiO<sub>2</sub>, which was dissolved at pH 12, contributed to the remarkable stability of the *c*-SiO<sub>2</sub> NPs at pH 7.4.

Zhang et al.<sup>14</sup> investigated the surface silanol densities of both *c*-SiO<sub>2</sub> and *f*-SiO<sub>2</sub> through Fourier transform infrared spectroscopy and found that *f*-SiO<sub>2</sub> had a lower total

silanol content (ca. 2.8 OH/nm<sup>2</sup>) than *c*-SiO<sub>2</sub> (ca. 4.5 OH/nm<sup>2</sup>). It is thus expected that the protruding hairy silanol and silicic acid groups were less abundant on *f*-SiO<sub>2</sub> NPs than on *c*-SiO<sub>2</sub> NPs. Therefore, the repulsive force caused by the hairy layers is likely to play a more important role in the stability of *c*-SiO<sub>2</sub> than that of *f*-SiO<sub>2</sub>. We do not, however, rule out the possibility of other mechanisms for the stability of *c*-SiO<sub>2</sub> NPs, such as hydration force resulting from the hydrogen bonding network between silanol groups.<sup>73</sup>

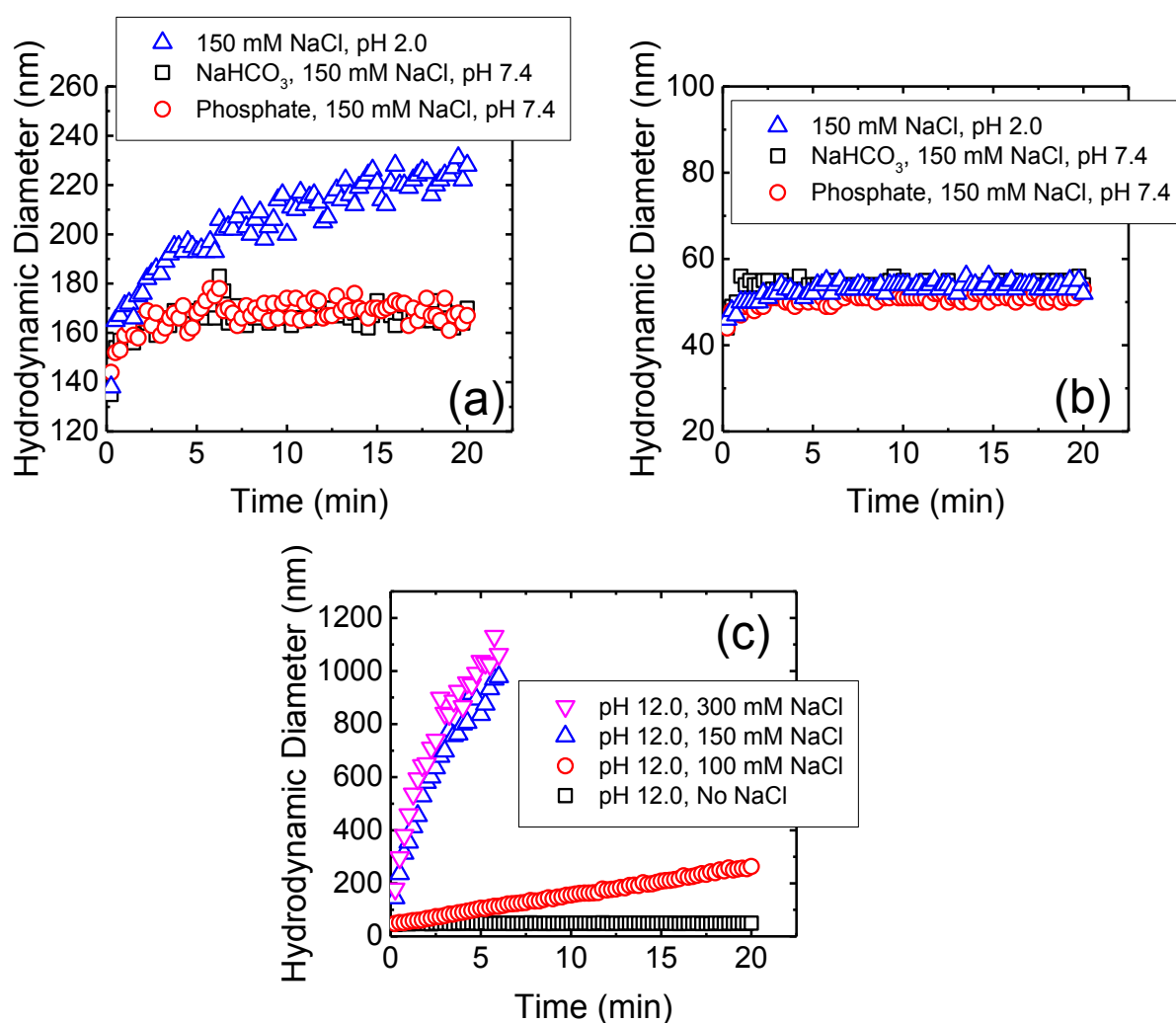


**Figure 4.3.** Aggregation profiles of (a) *f*-SiO<sub>2</sub> NPs at 150 mM NaCl at pH 7.4 (in phosphate and bicarbonate buffer) and pH 2.0 (pH adjusted with 1 M HCl), (b) *c*-SiO<sub>2</sub> NPs at 150 mM NaCl at pH 7.4 (in phosphate and bicarbonate buffer) and pH 2.0 (pH adjusted with 1 M HCl), and (c) *c*-SiO<sub>2</sub> NPs at pH 12 (pH adjusted with 1 M NaOH) at varying NaCl concentrations.

### 4.3.3 Phosphate Adsorption Enhanced the Stability of CeO<sub>2</sub> and Al<sub>2</sub>O<sub>3</sub> NPs

The aggregation kinetics of CeO<sub>2</sub> and Al<sub>2</sub>O<sub>3</sub> NPs were investigated over a wide range of NaCl concentrations in the presence of phosphate and the attachment efficiencies are presented in Figure 4.4. At NaCl concentrations of ca. 10–90 mM, the attachment efficiencies of both CeO<sub>2</sub> and Al<sub>2</sub>O<sub>3</sub> NPs increased with increasing NaCl concentrations (reaction-limited regime) as a result of the screening of their surface charge. At NaCl concentrations higher than 90 mM, a further increase in the salt concentration did not result in any substantial increase in the attachment efficiencies (diffusion-controlled regime) since the energy barrier to aggregation was eliminated due to charge screening under these conditions. The critical coagulation concentrations (CCCs) that demarcated the reaction- and diffusion-limited regimes were ca. 90 mM for both CeO<sub>2</sub> and Al<sub>2</sub>O<sub>3</sub> NPs in the presence of phosphate.

In addition, aggregation experiments were carried out at pH 7.4 in the absence of phosphate in order to elucidate the role of phosphate adsorption on the stability of CeO<sub>2</sub> and Al<sub>2</sub>O<sub>3</sub> NPs (Figure 4.4). Reaction- and diffusion-limited regimes were also observed for both CeO<sub>2</sub> and Al<sub>2</sub>O<sub>3</sub> NPs in bicarbonate buffer, indicating that the aggregation kinetics were controlled by electrostatic interactions in the absence of phosphate. The CCC values were determined to be ca. 2 mM for CeO<sub>2</sub> (Figure 4.4a) and 25 mM for Al<sub>2</sub>O<sub>3</sub> NPs (Figure 4.4b), both considerably lower than their respective CCCs in the presence of phosphate. This comparison implies that the stability of CeO<sub>2</sub> and Al<sub>2</sub>O<sub>3</sub> NPs was enhanced as a result of the adsorption of phosphate on the NP surface. As shown in Figure 4.1b, the adsorption of phosphate resulted in a significant increase in the magnitude of the surface charge of CeO<sub>2</sub> NPs, thereby increasing the energy barrier to NP aggregation. For Al<sub>2</sub>O<sub>3</sub> NPs, the surface

charge was reversed in the presence of phosphate and, additionally, the magnitude of the surface charge was increased (as shown in the increase in the magnitude of EPM in Figure 4.1b), thus raising the EDL repulsion between the NPs. Because the increase in the magnitude of surface charge due to the adsorption of phosphate was smaller for Al<sub>2</sub>O<sub>3</sub> than for CeO<sub>2</sub> (Figure 4.1b), the rise in CCC in the presence of phosphate was less pronounced for Al<sub>2</sub>O<sub>3</sub> than for CeO<sub>2</sub> NPs (Figure 4.4).

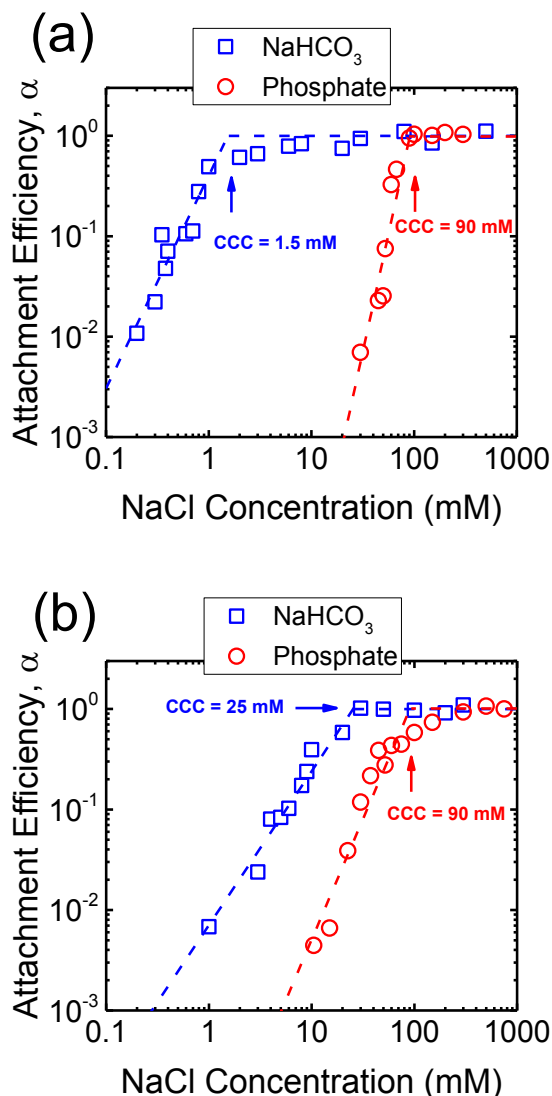


**Figure 4.4.** Aggregation attachment efficiencies of (a) CeO<sub>2</sub> and (b) Al<sub>2</sub>O<sub>3</sub> NPs as a function of NaCl concentration at pH 7.4 in phosphate and bicarbonate buffer. The dashed lines are extrapolated from the favorable and unfavorable aggregation regimes, and their intersections yield the CCCs.

#### 4.3.4 Deposition of CMP NPs on DOPC SLBs in the Presence of Phosphate

The deposition of the CMP NPs on DOPC SLBs was investigated in order to probe the propensity for CMP NPs to attach to lipid membranes. In our previous work, the DOPC bilayers were determined to be negatively charged at pH 7.<sup>23</sup> Figure 4.5 presents the rates of frequency shift during the deposition of CMP NPs on the SLBs in the presence of phosphate. When the NaCl concentration was raised from 1 to 30 mM, the deposition rates of *c*-SiO<sub>2</sub> and *f*-SiO<sub>2</sub> NPs on SLBs increased due to the reduction of the EDL repulsion between the NPs and SLBs. In contrast, no deposition of CeO<sub>2</sub> and Al<sub>2</sub>O<sub>3</sub> NPs on SLBs was detected over the NaCl concentration range of 1–100 mM.

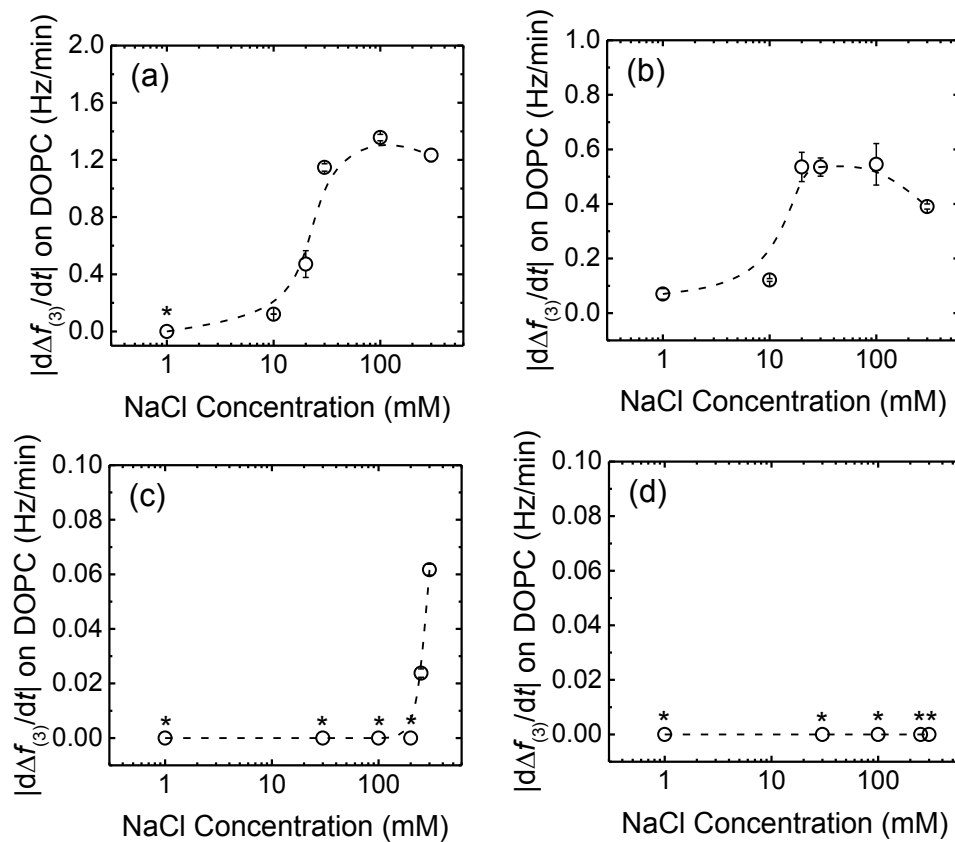


**Figure 4.5.** Deposition rates of (a) *c*-SiO<sub>2</sub>, (b) *f*-SiO<sub>2</sub>, (c) CeO<sub>2</sub>, and (d) Al<sub>2</sub>O<sub>3</sub> NPs on DOPC SLBs in phosphate buffer at pH 7.4. Error bars represent standard deviations and the lines are meant to guide the eye. Asterisks (\*) indicates that no frequency shift was detected.

By normalizing the deposition rates of CMP NPs on SLBs to the transport-limited deposition rates on PLL (presented in Figure 4.6), we obtained the deposition attachment efficiencies of the four NPs on SLBs, as presented in Figure 4.7. For the two SiO<sub>2</sub> NPs, the attachment efficiencies increased when the NaCl concentration was increased from 1 to 100 mM. At NaCl concentrations higher than 100 mM, the attachment efficiency did not increase with a further increase in NaCl concentration, most likely due to the complete screening of surface charges under these high ionic strength conditions. Interestingly, for both CeO<sub>2</sub> and Al<sub>2</sub>O<sub>3</sub> NPs, the attachment efficiency did not reach unity even at 300 mM NaCl.

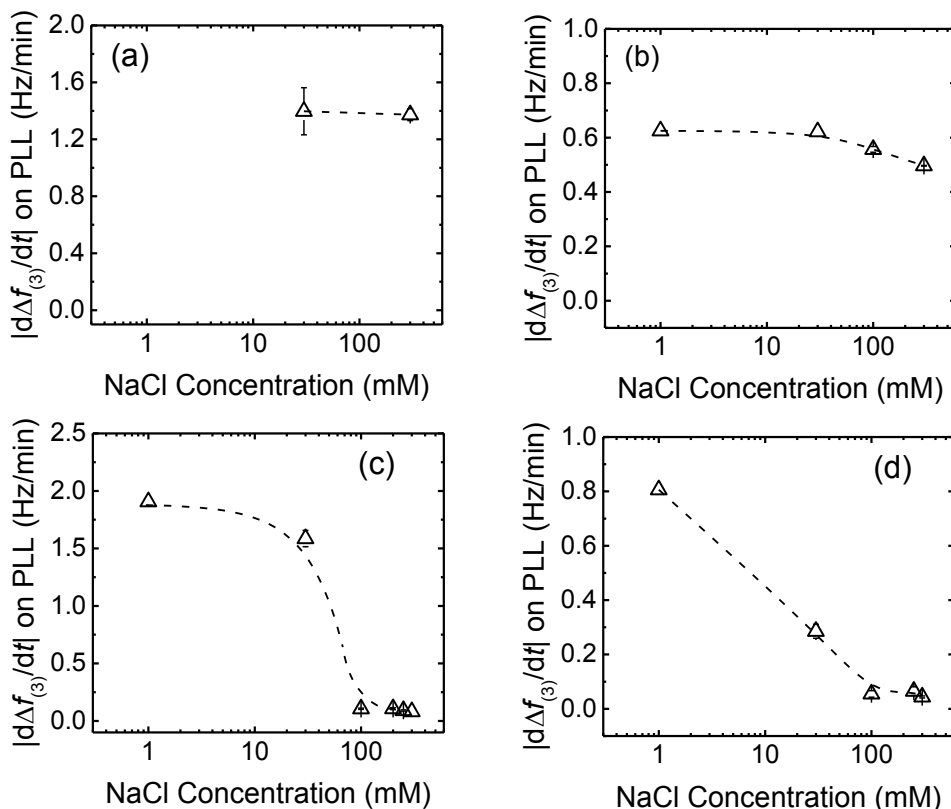


**Figure 4.6.** Deposition rates of (a) *c*-SiO<sub>2</sub>, (b) *f*-SiO<sub>2</sub>, (c) CeO<sub>2</sub>, and (d) Al<sub>2</sub>O<sub>3</sub> NPs on PLL-modified surfaces in phosphate buffer at pH 7.4. Error bars represent standard deviations and the lines are meant to guide the eye.

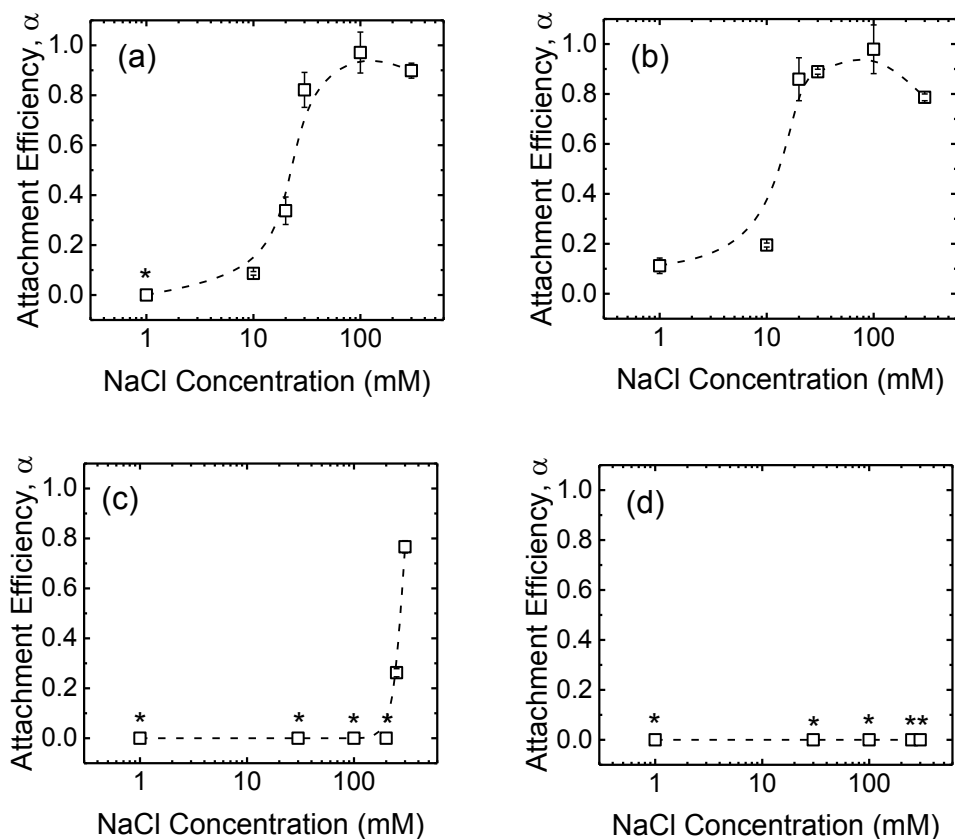


**Figure 4.7.** Deposition attachment efficiencies of (a) *c*-SiO<sub>2</sub>, (b) *f*-SiO<sub>2</sub>, (c) CeO<sub>2</sub>, and (d) Al<sub>2</sub>O<sub>3</sub> NPs on DOPC SLBs at pH 7.4 in phosphate buffer. Error bars represent standard deviations. The lines are meant to guide the eye. Asterisks (\*) indicate that no frequency shift was detected on SLBs.

#### 4.3.5 Comparing Deposition Kinetics of CMP NPs on DOPC SLBs in the Presence and Absence of Phosphate

In order to obtain further insights into the low propensity for CeO<sub>2</sub> and Al<sub>2</sub>O<sub>3</sub> NPs to deposit on SLBs in the presence of phosphate, additional deposition experiments on SLBs were performed in bicarbonate buffer. As shown in Figure 4.8a and b, both *c*-SiO<sub>2</sub> and *f*-SiO<sub>2</sub> NPs had similar propensities to attach to SLBs in phosphate and bicarbonate buffers, owing to their similar surface charge in the two buffers (Figure 4.1b).

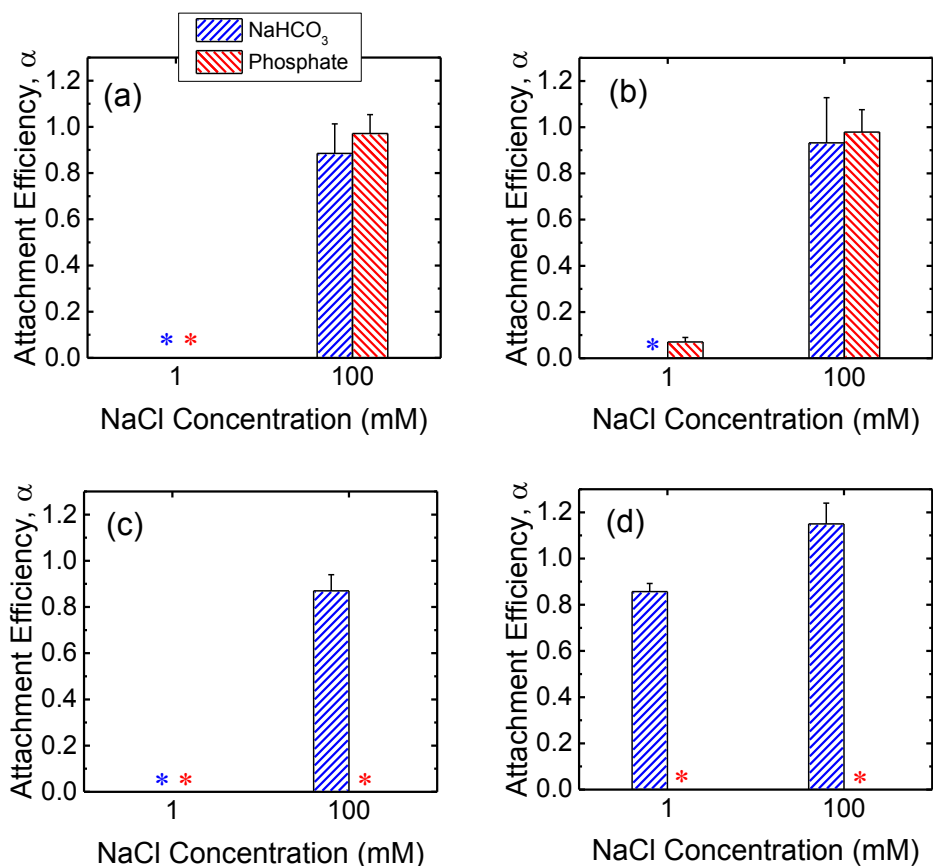


**Figure 4.8.** Deposition attachment efficiencies of (a) *c*-SiO<sub>2</sub>, (b) *f*-SiO<sub>2</sub>, (c) CeO<sub>2</sub>, and (d) Al<sub>2</sub>O<sub>3</sub> NPs on DOPC SLBs at pH 7.4 in phosphate and bicarbonate buffer. Error bars represent standard deviations. The data in phosphate buffer was reproduced from Figure 4.7 for comparison. Asterisks (\*) indicate that the attachment efficiencies were 0 (i.e., no frequency shift was detected on SLBs).

For the CeO<sub>2</sub> NPs, the deposition attachment efficiency in bicarbonate buffer increased from zero to close to unity when the NaCl concentration was raised from 1 to 100 mM (Figure 4.8c) due to the reduction in the EDL repulsion between the NPs and SLBs. In the presence of phosphate, however, the deposition attachment efficiencies of CeO<sub>2</sub> NPs on SLBs were zero at both 1 and 100 mM NaCl. According to the EPM measurements (Figure 4.1b), additional negative charge was imparted to the CeO<sub>2</sub> NPs through phosphate adsorption. Thus, the EDL repulsion between the CeO<sub>2</sub> NPs and SLBs may still be strong enough even at 100 mM NaCl to inhibit the deposition of the NPs.



For the deposition of Al<sub>2</sub>O<sub>3</sub> NPs on SLBs, a more pronounced contrast in attachment efficiency was observed in phosphate and bicarbonate buffers (Figure 4.8d). In bicarbonate buffer, Al<sub>2</sub>O<sub>3</sub> was positively charged at both 1 and 100 mM NaCl (Figure 4.1b). The attractive EDL and vdW interactions between Al<sub>2</sub>O<sub>3</sub> NPs and SLBs resulted in close-to-unity attachment efficiencies at both 1 and 100 mM NaCl in bicarbonate buffer. In the presence of phosphate, however, the attachment of Al<sub>2</sub>O<sub>3</sub> NPs on SLBs was not detected at both 1 and 100 mM NaCl due to the negative charge of Al<sub>2</sub>O<sub>3</sub> NPs imparted by phosphate adsorption (Figure 4.1b). The distinctly different deposition behaviors of both CeO<sub>2</sub> and Al<sub>2</sub>O<sub>3</sub> NPs on SLBs in the presence and absence of phosphate shows that it is imperative to account for the influence of phosphate adsorption in the assessment of NP association with cell membranes.

#### **4.3.6 No Disruption of Vesicles by CMP NPs Detected**

The attachment of NPs on cell membranes has been reported in some studies<sup>74, 75</sup> to result in the damage of the membranes and the leakage of intracellular contents. Dye leakage experiments have been employed in several studies on the disruption of cell membranes by silica,<sup>31</sup> gold,<sup>30</sup> TiO<sub>2</sub><sup>32</sup>, and graphene oxide<sup>53</sup> NPs. Herein, the disruption of the supported vesicles upon the attachment of CMP NPs was investigated by QCM-D coupled with fluorescence detection measurements. This technique enables us to simultaneously monitor the deposition of CMP NPs on the supported vesicles using QCM-D and detect the disruption of the vesicles by measuring the dye leakage from the vesicles.<sup>53</sup> These experiments were only performed in phosphate buffer in the context of cell membrane disruption in biological systems. Since no attachment of CeO<sub>2</sub> and Al<sub>2</sub>O<sub>3</sub> NPs on DOPC bilayers was expected to take place at 150 mM NaCl (i.e., ionic strength of physiological fluids), as shown in Figure 4.7c and d, these experiments were only conducted for both SiO<sub>2</sub> NPs.

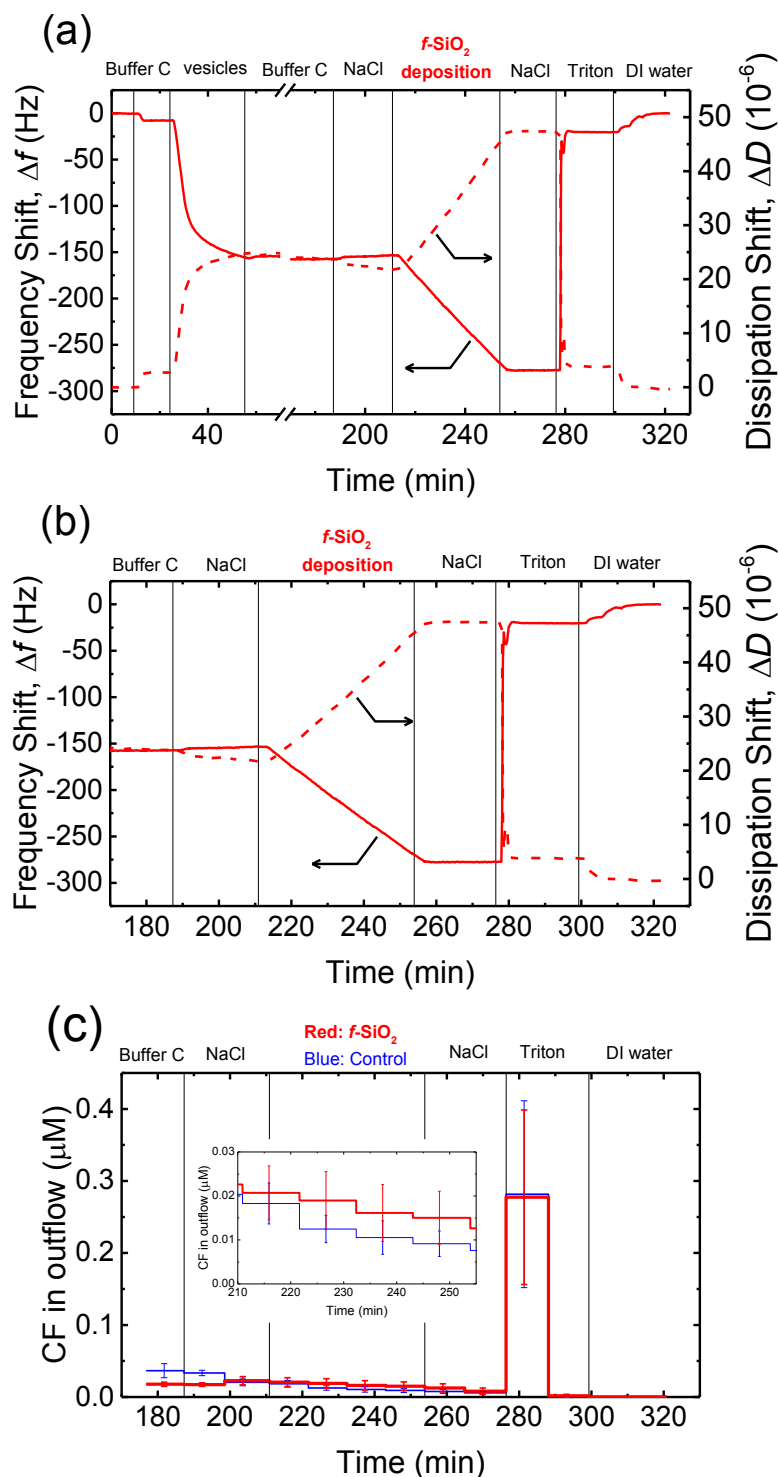


**Figure 4.9.** (a) Frequency and dissipation shifts during the formation of a SVL (26–57 min), the deposition of  $f$ -SiO<sub>2</sub> NPs on the SVL at 150 mM NaCl and pH 7.4 (213–257 min), and the rupture of the vesicles when they were exposed to 32 mM Triton X-100 (277–301 min). (b) Frequency and dissipation shifts when supported vesicles were exposed to  $f$ -SiO<sub>2</sub> NPs (in 150 mM NaCl), 150 mM NaCl, and 32 mM Triton X-100. (c) Release of CF dye from supported vesicles upon exposure to  $f$ -SiO<sub>2</sub> NPs (in 150 mM NaCl), 150 mM NaCl, and 32 mM Triton X-100. Insert: close-up of the release of dye in the  $f$ -SiO<sub>2</sub> NP deposition stage.

The frequency and dissipation shifts during the formation of a SVL and the deposition of *f*-SiO<sub>2</sub> NPs on the SVL are presented in Figure 4.9a. Figure 4.9b and c show the frequency and dissipation shifts and the dye concentration in the outflow of QCM-D, respectively, during the deposition of *f*-SiO<sub>2</sub> NPs on the SVL. The experimental protocol involves three stages: 1) deposition of dye-encapsulated vesicles on a gold-coated sensor to form a SVL (26–57 min, only in Figure 4.9a); 2) removal of unadsorbed vesicles with buffer rinse (57–190 min); and 3) deposition of NPs on the SVL at 150 mM NaCl (213–257 min). The fluorescence intensity of the outflow was monitored from close to the end of Stage 2 onwards (from 176 min). In a typical experiment, four QCM-D chambers were employed. In two of the chambers, deposition experiments were performed with a suspension of CMP NPs prepared in 150 mM NaCl. In the other two chambers, control experiments were conducted using the same procedure as the deposition experiments, except that a 150 mM NaCl solution was used in lieu of the NP suspension.

As shown in Figure 4.9a and b, *f*-SiO<sub>2</sub> NPs deposited on the SVL continuously without eliciting significant rupture of the vesicles as evidenced from the monotonic decrease in frequency and increase in dissipation shifts (213–257 min). At the same time, no significant difference in dye leakage concentration was observed between the deposition and control experiments (inset of Figure 4.9c, two-tailed *t* test, significance level of 0.05). As a positive control, the exposure of the vesicles to Triton (276 min) resulted in precipitous frequency and dissipation shifts (Figure 4.9b), as well as a dramatic increase in fluorescence intensity (Figure 4.9c), indicating that the vesicles had been ruptured by the surfactant. Hence, it can be inferred that the deposition of *f*-SiO<sub>2</sub> NPs on the SVL did not induce appreciable disruption of the lipid membrane. Similar experiments were performed for *c*-

SiO<sub>2</sub> NPs and no significant dye leakage was observed during the deposition of *c*-SiO<sub>2</sub> NPs on the vesicles (Figure 4.10). These results demonstrate that both of SiO<sub>2</sub> NPs have a low propensity to disrupt DOPC bilayers at 150 mM NaCl despite their high affinity to associate with the model membranes under these conditions.

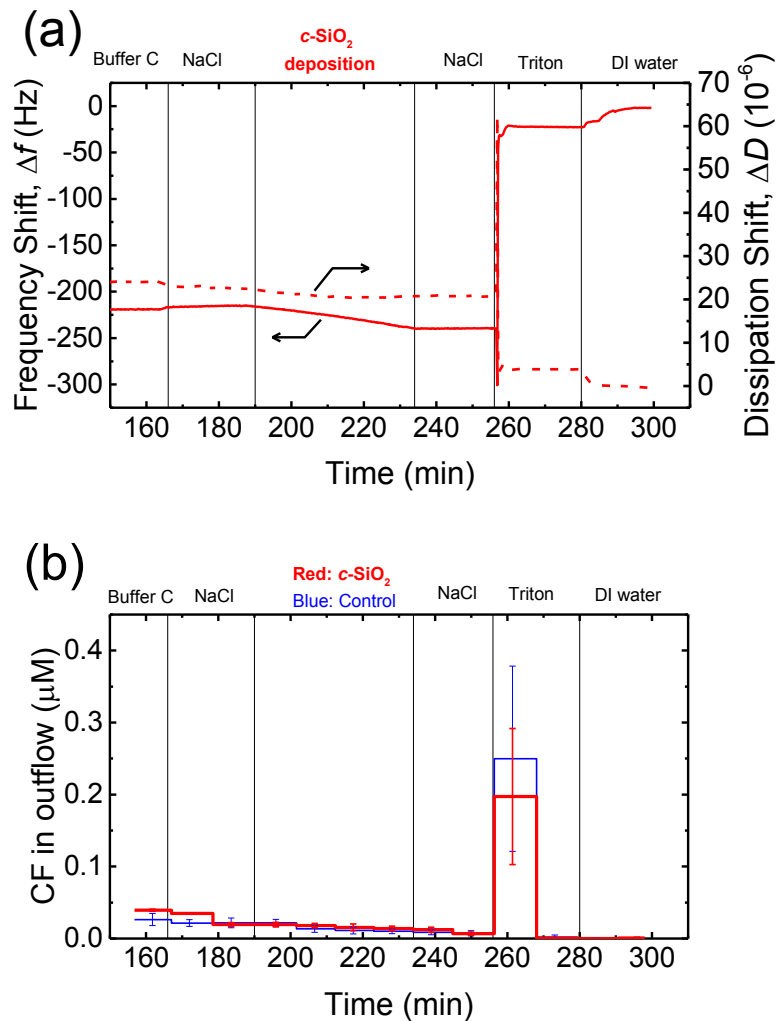


**Figure 4.10.** (a) Frequency and dissipation shifts when supported vesicles were exposed to *c*-SiO<sub>2</sub> NP suspension prepared at 150 mM NaCl (191–234 min), 150 mM NaCl solution (234–256 min), and 32 mM Triton X-100 solution (256–280 min). The solid and dash lines show the frequency and dissipation shifts, respectively. (b) Release of CF dye from supported vesicles when the vesicles were exposed to *c*-SiO<sub>2</sub> NP suspension prepared at 150 mM NaCl, 150 mM NaCl solution, and 32 mM Triton X-100 solution. The red and blue lines show the dye release profiles in the NP deposition and control experiments, respectively. Error bars represent standard deviations.

#### 4.4 Conclusions

In this study, the aggregation behavior of four CMP NPs and their interactions with model cell membranes at neutral pH conditions were investigated. One important aspect of this study is to examine the influence of phosphate, a key component of biological fluids, on the surface charge and colloidal stability of the NPs, as well as on the nanoparticle–membrane interactions. The surface charge of both *c*-SiO<sub>2</sub> and *f*-SiO<sub>2</sub> NPs was not appreciably altered by phosphate as phosphate did not adsorb favorably on the NP surface. As a result, both SiO<sub>2</sub> NPs had similar aggregation and deposition kinetics on SLBs in the presence and absence of phosphate. Conversely, the CeO<sub>2</sub> NPs became more negatively charged while the Al<sub>2</sub>O<sub>3</sub> NPs underwent charge reversal (positive to negative) in the presence of phosphate, both likely due to the adsorption of phosphate on the NPs through inner-sphere complexation. The enhancement of surface charge in the presence of phosphate led to an increase in the stability of CeO<sub>2</sub> and Al<sub>2</sub>O<sub>3</sub> NPs and decreased the NPs' propensity to attach to SLBs. These results imply that the nonspecific interactions between NPs and cell membranes and potentially the biological effects of NPs may be controlled by phosphate. Thus, the role of phosphate needs to be accounted for in the assessment of the stability and cellular interactions of NPs. Additionally, the deposition of both *c*-SiO<sub>2</sub> and *f*-SiO<sub>2</sub> NPs on supported vesicles did not result in detectable disruption of the vesicles. Future studies that include a systematic variation of membrane properties (e.g., lipid composition and incorporation of proteins in membranes) and CMP NP properties (e.g., sizes and shapes) will enable additional mechanistic insights into the interactions between the nanoparticles and cell membranes. The effects of other major constituents in biological fluids (e.g., proteins) should also be investigated.

## 4.5 References

1. Steigerwald, J. M.; Murarka, S. P.; Gutmann, R. J., *Chemical mechanical planarization of microelectronic materials*. John Wiley & Sons: 2008.
2. Krishnan, M.; Nalaskowski, J. W.; Cook, L. M., Chemical Mechanical Planarization: Slurry Chemistry, Materials, and Mechanisms. *Chem. Rev. (Washington, DC, U. S.)* **2010**, *110*, (1), 178-204.
3. Lai, C. L.; Lin, S. H., Treatment of chemical mechanical polishing wastewater by electrocoagulation: system performances and sludge settling characteristics. *Chemosphere* **2004**, *54*, (3), 235-242.
4. Lin, S. H.; Yang, C. R., Chemical and physical treatments of chemical mechanical polishing wastewater from semiconductor fabrication. *J. Hazard. Mater.* **2004**, *108*, (1-2), 103-109.
5. Den, W.; Huang, C. P., Electrocoagulation for removal of silica nano-particles from chemical-mechanical-planarization wastewater. *Colloid Surface A* **2005**, *254*, (1-3), 81-89.
6. Li, Y., *Microelectronic applications of chemical mechanical planarization*. John Wiley & Sons: 2007.
7. Speed, D.; Westerhoff, P.; Sierra-Alvarez, R.; Draper, R.; Pantano, P.; Aravamudhan, S.; Chen, K. L.; Hristovski, K.; Herckes, P.; Bi, X. Y.; Yang, Y.; Zeng, C.; Otero-Gonzalez, L.; Mikoryak, C.; Wilson, B. A.; Kosaraju, K.; Tarannum, M.; Crawford, S.; Yi, P.; Liu, X. T.; Babu, S. V.; Moinpour, M.; Ranville, J.; Montano, M.; Corredor, C.; Posner, J.; Shadman, F., Physical, chemical, and in vitro toxicological characterization of nanoparticles in chemical mechanical planarization suspensions used in the semiconductor industry: towards environmental health and safety assessments. *Environ-Sci Nano* **2015**, *2*, (3), 227-244.
8. Limbach, L. K.; Bereiter, R.; Mueller, E.; Krebs, R.; Gaelli, R.; Stark, W. J., Removal of oxide nanoparticles in a model wastewater treatment plant: Influence of agglomeration and surfactants on clearing efficiency. *Environ. Sci. Technol.* **2008**, *42*, (15), 5828-5833.
9. Shepard, M. N.; Brenner, S., An Occupational Exposure Assessment for Engineered Nanoparticles Used in Semiconductor Fabrication. *Annals of Occupational Hygiene* **2014**, *58*, (2), 251-265.
10. Brenner, S. A.; Neu-Baker, N. M., Occupational exposure to nanomaterials: Assessing the potential for cutaneous exposure to metal oxide nanoparticles in a semiconductor facility. *Journal of Chemical Health and Safety* **2014**, *22*, (4), 10-19.
11. Bergna, H. E.; Roberts, W. O., *Colloidal silica: fundamentals and applications*. CRC Press: 2005; Vol. 131.
12. Pratsinis, S. E., Flame aerosol synthesis of ceramic powders. *Progr. Energy Combust. Sci.* **1998**, *24*, (3), 197-219.
13. Zantye, P. B.; Kumar, A.; Sikder, A. K., Chemical mechanical planarization for microelectronics applications. *Materials Science & Engineering R-Reports* **2004**, *45*, (3-6), 89-220.
14. Zhang, H. Y.; Dunphy, D. R.; Jiang, X. M.; Meng, H.; Sun, B. B.; Tarn, D.; Xue, M.; Wang, X.; Lin, S. J.; Ji, Z. X.; Li, R. B.; Garcia, F. L.; Yang, J.; Kirk, M. L.; Xia, T.; Zink, J. I.; Nel, A.; Brinker, C. J., Processing Pathway Dependence of Amorphous Silica Nanoparticle Toxicity: Colloidal vs Pyrolytic. *J. Am. Chem. Soc.* **2012**, *134*, (38), 15790-15804.

15. Lin, W. S.; Huang, Y. W.; Zhou, X. D.; Ma, Y. F., Toxicity of cerium oxide nanoparticles in human lung cancer cells. *International Journal of Toxicology* **2006**, *25*, (6), 451-457.
16. Song, M. G.; Lee, J. H.; Lee, Y. G.; Koo, J. H., Stabilization of gamma alumina slurry for chemical-mechanical polishing of copper. *J. Colloid Interface Sci.* **2006**, *300*, (2), 603-611.
17. Otero-Gonzalez, L.; Sierra-Alvarez, R.; Boitano, S.; Field, J. A., Application and Validation of an Impedance-Based Real Time Cell Analyzer to Measure the Toxicity of Nanoparticles Impacting Human Bronchial Epithelial Cells. *Environ. Sci. Technol.* **2012**, *46*, (18), 10271-10278.
18. Vinardell, M. P.; Sorde, A.; Diaz, J.; Baccarin, T.; Mitjans, M., Comparative effects of macro-sized aluminum oxide and aluminum oxide nanoparticles on erythrocyte hemolysis: influence of cell source, temperature, and size. *J Nanopart Res* **2015**, *17*, (2).
19. Nel, A. E.; Madler, L.; Velegol, D.; Xia, T.; Hoek, E. M. V.; Somasundaran, P.; Klaessig, F.; Castranova, V.; Thompson, M., Understanding biophysicochemical interactions at the nano-bio interface. *Nat. Mater.* **2009**, *8*, (7), 543-557.
20. Chen, K. L.; Bothun, G. D., Nanoparticles Meet Cell Membranes: Probing Nonspecific Interactions. using Model Membranes. *Environ. Sci. Technol.* **2014**, *48*, (2), 873-880.
21. Yang, K.; Ma, Y. Q., Computer simulation of the translocation of nanoparticles with different shapes across a lipid bilayer. *Nat. Nanotechnol.* **2010**, *5*, (8), 579-583.
22. Troiano, J. M.; Olenick, L. L.; Kuech, T. R.; Melby, E. S.; Hu, D. H.; Lohse, S. E.; Mensch, A. C.; Dogangun, M.; Vartanian, A. M.; Torelli, M. D.; Ehimighe, E.; Walter, S. R.; Fu, L.; Anderton, C. R.; Zhu, Z. H.; Wang, H. F.; Orr, G.; Murphy, C. J.; Hamers, R. J.; Pedersen, J. A.; Geiger, F. M., Direct Probes of 4 nm Diameter Gold Nanoparticles Interacting with Supported Lipid Bilayers. *J. Phys. Chem. C* **2015**, *119*, (1), 534-546.
23. Yi, P.; Chen, K. L., Interaction of multiwalled carbon nanotubes with supported lipid bilayers and vesicles as model biological membranes. *Environ Sci Technol* **2013**, *47*, (11), 5711-9.
24. Zhang, X. F.; Yang, S. H., Nonspecific Adsorption of Charged Quantum Dots on Supported Zwitterionic Lipid Bilayers: Real-Time Monitoring by Quartz Crystal Microbalance with Dissipation. *Langmuir* **2011**, *27*, (6), 2528-2535.
25. Jing, B.; Zhu, Y., Disruption of supported lipid bilayers by semihydrophobic nanoparticles. *J. Am. Chem. Soc.* **2011**, *133*, (28), 10983-9.
26. Frost, R.; Jonsson, G. E.; Chakarov, D.; Svedhem, S.; Kasemo, B., Graphene Oxide and Lipid Membranes: Interactions and Nanocomposite Structures. *Nano Lett.* **2012**, *12*, (7), 3356-3362.
27. Jacobson, K. H.; Gunsolus, I. L.; Kuech, T. R.; Troiano, J. M.; Melby, E. S.; Lohse, S. E.; Hu, D.; Chrisler, W. B.; Murphy, C. J.; Orr, G.; Geiger, F. M.; Haynes, C. L.; Pedersen, J. A., Lipopolysaccharide density and structure governs the extent and distance of nanoparticle interaction with actual and model bacterial outer membranes. *Environ. Sci. Technol.* **2015**, *49*, (17), 10642-10650.
28. Leroueil, P. R.; Berry, S. A.; Duthie, K.; Han, G.; Rotello, V. M.; McNerny, D. Q.; Baker, J. R.; Orr, B. G.; Holl, M. M. B., Wide varieties of cationic nanoparticles induce defects in supported lipid bilayers. *Nano Lett.* **2008**, *8*, (2), 420-424.

29. Lesniak, A.; Salvati, A.; Santos-Martinez, M. J.; Radomski, M. W.; Dawson, K. A.; Aberg, C., Nanoparticle adhesion to the cell membrane and its effect on nanoparticle uptake efficiency. *J. Am. Chem. Soc.* **2013**, *135*, (4), 1438-44.
30. Goodman, C. M.; McCusker, C. D.; Yilmaz, T.; Rotello, V. M., Toxicity of gold nanoparticles functionalized with cationic and anionic side chains. *Bioconjugate Chem.* **2004**, *15*, (4), 897-900.
31. Pera, H.; Kleijn, J. M.; Leermakers, F. A. M., Interaction of Silica Nanoparticles with Phospholipid Membranes. *Chem. Lett.* **2012**, *41*, (10), 1322-1324.
32. Moghadam, B. Y.; Hou, W. C.; Corredor, C.; Westerhoff, P.; Posner, J. D., Role of nanoparticle surface functionality in the disruption of model cell membranes. *Langmuir* **2012**, *28*, (47), 16318-26.
33. Tobey, S. L.; Anslyn, E. V., Determination of inorganic phosphate in serum and saliva using a synthetic receptor. *Org. Lett.* **2003**, *5*, (12), 2029-2031.
34. Albanese, A.; Chan, W. C. W., Effect of Gold Nanoparticle Aggregation on Cell Uptake and Toxicity. *ACS Nano* **2011**, *5*, (7), 5478-5489.
35. Liu, X. S.; Chen, Y. J.; Li, H.; Huang, N.; Jin, Q.; Ren, K. F.; Ji, J., Enhanced Retention and Cellular Uptake of Nanoparticles in Tumors by Controlling Their Aggregation Behavior. *ACS Nano* **2013**, *7*, (7), 6244-6257.
36. Masui, T.; Fujiwara, K.; Machida, K.; Adachi, G.; Sakata, T.; Mori, H., Characterization of Cerium(IV) oxide ultrafine particles prepared using reversed micelles. *Chem. Mater.* **1997**, *9*, (10), 2197-2204.
37. Parida, K. M.; Pradhan, A. C.; Das, J.; Sahu, N., Synthesis and characterization of nano-sized porous gamma-alumina by control precipitation method. *Mater. Chem. Phys.* **2009**, *113*, (1), 244-248.
38. Murphy, J.; Riley, J. P., A modified single solution method for the determination of phosphate in natural waters. *Anal. Chim. Acta* **1962**, *27*, 31-36.
39. Chen, K. L.; Mylon, S. E.; Elimelech, M., Aggregation kinetics of alginate-coated hematite nanoparticles in monovalent and divalent electrolytes. *Environ. Sci. Technol.* **2006**, *40*, (5), 1516-1523.
40. Chen, K. L.; Elimelech, M., Aggregation and deposition kinetics of fullerene (C-60) nanoparticles. *Langmuir* **2006**, *22*, (26), 10994-11001.
41. Hoekstra, L. L.; Vreeker, R.; Agterof, W. G. M., Aggregation of Colloidal Nickel Hydroxycarbonate Studied by Light-Scattering. *J. Colloid Interface Sci.* **1992**, *151*, (1), 17-25.
42. Saleh, N. B.; Pfefferle, L. D.; Elimelech, M., Aggregation Kinetics of Multiwalled Carbon Nanotubes in Aquatic Systems: Measurements and Environmental Implications. *Environ. Sci. Technol.* **2008**, *42*, (21), 7963-7969.
43. Chowdhury, I.; Duch, M. C.; Mansukhani, N. D.; Hersam, M. C.; Bouchard, D., Colloidal properties and stability of graphene oxide nanomaterials in the aquatic environment. *Environ. Sci. Technol.* **2013**, *47*, (12), 6288-96.
44. Holthoff, H.; Egelhaaf, S. U.; Borkovec, M.; Schurtenberger, P.; Sticher, H., Coagulation rate measurements of colloidal particles by simultaneous static and dynamic light scattering. *Langmuir* **1996**, *12*, (23), 5541-5549.
45. Cho, N. J.; Frank, C. W.; Kasemo, B.; Hook, F., Quartz crystal microbalance with dissipation monitoring of supported lipid bilayers on various substrates. *Nat. Protoc.* **2010**, *5*, (6), 1096-106.



46. Yi, P.; Chen, K. L., Interaction of Multiwalled Carbon Nanotubes with Supported Lipid Bilayers and Vesicles as Model Biological Membranes. *Environ. Sci. Technol.* **2013**, *47*, (11), 5711-5719.
47. Qu, X. L.; Alvarez, P. J. J.; Li, Q. L., Impact of Sunlight and Humic Acid on the Deposition Kinetics of Aqueous Fullerene Nanoparticles (nC(60)). *Environ. Sci. Technol.* **2012**, *46*, (24), 13455-13462.
48. Keller, C. A.; Kasemo, B., Surface specific kinetics of lipid vesicle adsorption measured with a quartz crystal microbalance. *Biophys. J.* **1998**, *75*, (3), 1397-1402.
49. Chen, K. L.; Elimelech, M., Interaction of Fullerene (C-60) Nanoparticles with Humic Acid and Alginate Coated Silica Surfaces: Measurements, Mechanisms, and Environmental Implications. *Environ. Sci. Technol.* **2008**, *42*, (20), 7607-7614.
50. Yi, P.; Chen, K. L., Influence of surface oxidation on the aggregation and deposition kinetics of multiwalled carbon nanotubes in monovalent and divalent electrolytes. *Langmuir* **2011**, *27*, (7), 3588-99.
51. de Kerchove, A. J.; Elimelech, M., Structural growth and viscoelastic properties of adsorbed alginate layers in monovalent and divalent salts. *Macromolecules* **2006**, *39*, (19), 6558-6564.
52. Stumm, W.; Morgan, J. J., *Aquatic chemistry: an introduction emphasizing chemical equilibria in natural waters*. John Wiley: 1981.
53. Liu, X.; Chen, K. L., Interactions of Graphene Oxide with Model Cell Membranes: Probing Nanoparticle Attachment and Lipid Bilayer Disruption. *Langmuir* **2015**, *31*, (44), 12076-86.
54. Schnaitm.Ca, Solubilization of Cytoplasmic Membrane of Escherichia-Coli by Triton X-100. *J. Bacteriol.* **1971**, *108*, (1), 545-552.
55. Elimelech, M. G., J.; Jia, X.; Williams, R. A., *Particle Deposition and Aggregation: Measurement, Modelling and Simulation*. Butterworth-Heinemann: Oxford: England, 1995.
56. Hiemstra, T.; Venema, P.; VanRiemsdijk, W. H., Intrinsic proton affinity of reactive surface groups of metal (hydr)oxides: The bond valence principle. *J. Colloid Interface Sci.* **1996**, *184*, (2), 680-692.
57. Kosmulski, M., The pH-dependent surface charging and the points of zero charge. *J. Colloid Interface Sci.* **2002**, *253*, (1), 77-87.
58. Kosmulski, M., The pH-dependent surface charging and points of zero charge V. Update. *J. Colloid Interface Sci.* **2011**, *353*, (1), 1-15.
59. Tsunekawa, S.; Fukuda, T.; Kasuya, A., Blue shift in ultraviolet absorption spectra of monodisperse CeO<sub>2-x</sub> nanoparticles. *J. Appl. Phys.* **2000**, *87*, (3), 1318-1321.
60. Zhang, G. J.; Yang, J. F.; Ohji, T., Fabrication of porous ceramics with unidirectionally aligned continuous pores. *J. Am. Ceram. Soc.* **2001**, *84*, (6), 1395-1397.
61. Wang, S. W.; Di Ventura, M.; Kim, S. G.; Pantelides, S. T., Atomic-scale dynamics of the formation and dissolution of carbon clusters in SiO<sub>2</sub>. *Phys. Rev. Lett.* **2001**, *86*, (26), 5946-5949.
62. Johnson, B. B.; Ivanov, A. V.; Antzutkin, O. N.; Forsling, W., P-31 nuclear magnetic resonance study of the adsorption of phosphate and phenyl phosphates on gamma-Al<sub>2</sub>O<sub>3</sub>. *Langmuir* **2002**, *18*, (4), 1104-1111.
63. Laiti, E.; Persson, P.; Ohman, L. O., Surface complexation and precipitation at the H<sup>+</sup>-orthophosphate-aged gamma-Al<sub>2</sub>O<sub>3</sub>/water interface. *Langmuir* **1996**, *12*, (12), 2969-2975.

64. Hunter, R. J., *Zeta potential in colloid science: principles and applications*. Academic press: 2013; Vol. 2.
65. Van Hoecke, K.; Quik, J. T. K.; Mankiewicz-Boczek, J.; De Schamphelaere, K. A. C.; Elsaesser, A.; Van der Meeren, P.; Barnes, C.; McKerr, G.; Howard, C. V.; Van De Meent, D.; Rydzynski, K.; Dawson, K. A.; Salvati, A.; Lesniak, A.; Lynch, I.; Silversmit, G.; De Samber, B.; Vincze, L.; Janssen, C. R., Fate and Effects of CeO<sub>2</sub> Nanoparticles in Aquatic Ecotoxicity Tests. *Environ. Sci. Technol.* **2009**, *43*, (12), 4537-4546.
66. Cornelis, G.; Ryan, B.; McLaughlin, M. J.; Kirby, J. K.; Beak, D.; Chittleborough, D., Solubility and Batch Retention of CeO<sub>2</sub> Nanoparticles in Soils. *Environ. Sci. Technol.* **2011**, *45*, (7), 2777-2782.
67. Higashitani, K.; Kondo, M.; Hatade, S., Effect of Particle-Size on Coagulation Rate of Ultrafine Colloidal Particles. *J. Colloid Interface Sci.* **1991**, *142*, (1), 204-213.
68. Depasse, J., Simple experiments to emphasize the main characteristics of the coagulation of silica hydrosols by alkaline cations: Application to the analysis of the model of Colic et al. *J. Colloid Interface Sci.* **1999**, *220*, (1), 174-176.
69. Kobayashi, M.; Juillerat, F.; Galletto, P.; Bowen, P.; Borkovec, M., Aggregation and charging of colloidal silica particles: Effect of particle size. *Langmuir* **2005**, *21*, (13), 5761-5769.
70. Ducker, W. A.; Senden, T. J.; Pashley, R. M., Direct Measurement of Colloidal Forces Using an Atomic Force Microscope. *Nature* **1991**, *353*, (6341), 239-241.
71. Vigil, G.; Xu, Z. H.; Steinberg, S.; Israelachvili, J., Interactions of Silica Surfaces. *J. Colloid Interface Sci.* **1994**, *165*, (2), 367-385.
72. Israelachvili, J.; Wennerstrom, H., Role of hydration and water structure in biological and colloidal interactions. *Nature* **1996**, *379*, (6562), 219-225.
73. Chapel, J. P., Electrolyte Species-Dependent Hydration Forces between Silica Surfaces. *Langmuir* **1994**, *10*, (11), 4237-4243.
74. Lin, Y. S.; Haynes, C. L., Impacts of Mesoporous Silica Nanoparticle Size, Pore Ordering, and Pore Integrity on Hemolytic Activity. *J. Am. Chem. Soc.* **2010**, *132*, (13), 4834-4842.
75. Yu, T.; Malugin, A.; Ghandehari, H., Impact of Silica Nanoparticle Design on Cellular Toxicity and Hemolytic Activity. *ACS Nano* **2011**, *5*, (7), 5717-5728.

**Chapter 5. Silver Nanoparticles Formed *In Situ* on  
AFM Tips for Force Measurements with Model  
Cell Membranes: Influence of Protein Coronas<sup>1</sup>**

---

<sup>1</sup> This chapter will be submitted for publication in a peer-reviewed journal. Co-author Kai Loon Chen helped with data interpretation and manuscript editing.

## 5.1 Introduction

With the extensive use of silver nanoparticles (AgNPs) in consumer products,<sup>1</sup> the potential exposure of humans to the nanoparticles poses a risk to human health.<sup>2,3</sup> AgNPs have been shown to cause damage to DNA and mitochondria in human cells.<sup>4</sup> Currently, the mechanisms for the cytotoxicity of AgNPs are still under investigation.

A better understanding of how AgNPs interact with cell membranes is necessary for the elucidation of the underlying mechanisms for the reported cytotoxicity of AgNPs. For example, AgNPs have been shown to induce damage to the membranes of red blood cells which leads to the leakage of hemoglobin.<sup>5,6</sup> AgNPs have been reported to be internalized into human epithelial A549 cells and further undergo dissolution to release toxic Ag<sup>+</sup> ions in the cytosol.<sup>7</sup> Previous studies have demonstrated that the internalization of nanoparticles by cells depend on the propensity for nanoparticles to attach to cell membranes as well as the nanoparticle-cell membrane adhesion strength.<sup>8,9</sup> To date, studies on AgNP-cell membrane interactions have involved the use of both human cells<sup>10</sup> and artificial (or model) cell membranes.<sup>11</sup> The use of artificial cell membranes enables a precise control over the compositions and properties of the membranes, thereby allowing for the elucidation of nanoparticle-membrane interactions at a molecular level.<sup>12</sup>

Since the attachment of nanoparticles to cell membranes is expected to be heavily influenced by nanoparticle-membrane interaction forces, a method that allows for the direct measurements of the interaction forces of AgNPs with cell membranes is highly desirable. Atomic force microscopy (AFM) has been used for force measurements between cell membranes and tips modified with a cluster of nanoparticles.<sup>13</sup> This method, however, requires the use of a micromanipulator which may not be readily available. Our strategy to

modify AFM tips with AgNPs involves the coating of AFM tips by polydopamine (PDA)<sup>14, 15</sup> and the *in situ* reduction of silver ions by the catechol groups in the PDA.<sup>14</sup> We show for the first time that successive exposure of AFM probes to polydopamine and silver nitrate solutions resulted in the formation of AgNPs on the apex of the tips. The AgNP-modified tips enable the measurements of the interaction forces between a silver nanoparticle and a lipid bilayer formed on mica as a model cell membrane. Due to the abundance of human serum albumin (HSA) proteins in human bloodstream and saliva,<sup>16</sup> the influence of HSA on the interactions with the AgNP-modified tips and model cell membranes was also investigated.

## 5.2 Materials and Methods

### 5.2.1 Preparation and Characterization of AgNP-Modified AFM Probes

AFM probes (SNL-10, Bruker) with silicon tips at the end of silicon nitride cantilevers were modified with AgNPs. The functionalization of AFM tips by AgNPs was achieved through the formation of a PDA film on the tip and the subsequent reduction of silver ions by PDA to form AgNPs.<sup>15</sup> Dopamine hydrochloride powder (0.2 g; Sigma-Aldrich) was dissolved in a 15 mM Trizma hydrochloride buffer at pH 8.5 (Sigma-Aldrich). Under constant agitation, the solution gradually turned darker, indicating that dopamine underwent polymerization to form PDA.<sup>14</sup> An AFM probe was immersed in the PDA solution for 45 min to allow for the formation of a PDA film on the probe.<sup>15</sup> Next, the probe was gently placed in a Petri dish containing de-ionized (DI) water (18 M $\Omega$ -cm, Milli-Q system, Millipore, MA) to remove unadsorbed PDA and subsequently placed in a Petri dish containing a freshly prepared 500 mM AgNO<sub>3</sub> solution. The petri dish was covered with

aluminum foil to avoid light exposure. After 16 hours, the AFM probe was gently placed in a Petri dish containing DI water to remove the AgNO<sub>3</sub> solution attached to the probe. Finally, the probe was placed in a vacuum desiccator at room temperature until use.

The morphology and surface composition of unmodified silicon tips, tips exposed to PDA only, and tips exposed to both PDA and AgNO<sub>3</sub> solutions (to be referred to as Si, PDA, and Ag-PDA tips, respectively) were examined with an EOL JSM-6700F field emission scanning electron microscope (FE-SEM, JEOL) coupled with an energy dispersive spectrometer (EDS).

### **5.2.2 Preparation of Lipid Vesicles**

Small unilamellar vesicles comprised of zwitterionic 1,2-dioleoyl-*sn*-glycero-3-phosphocholine (DOPC) were prepared using the extrusion method.<sup>17</sup> The procedure involved the drying of a DOPC solution in chloroform to form a DOPC film on the bottom of an Erlenmeyer flask, the hydration of the film with a HEPES buffer solution (10 mM HEPES, 150 mM NaCl, 2 mM CaCl<sub>2</sub>, pH 7.4), and the extrusion of the DOPC solution using a mini-extruder (Avanti Polar Lipids Inc.) through a polycarbonate membrane with a pore size of 50 nm (Whatman) to obtain unilamellar DOPC vesicles.

### **5.2.3 Formation and AFM Imaging of Lipid Bilayers on Mica**

DOPC SLBs were formed on mica through vesicle fusion.<sup>18</sup> A freshly cleaved mica (Grade V-1 Muscovite, 2SPI Supplies) was mounted onto the AFM (Multimode NanoScope IIIId, Bruker Nano Inc) scanner. An AFM probe with unmodified silicon tips (SNL-10, Bruker) was secured in a glass fluid cell, which was then mounted on the AFM stage. Next, a 50 mg/L DOPC suspension (diluted in HEPES buffer) was slowly injected into the fluid

cell with a syringe. After waiting for 10 min to allow for the adsorption of DOPC vesicles and the rupture of the vesicles on mica, tapping-mode AFM imaging was performed to observe the SLBs formed on mica. Cantilevers with a nominal spring constant of 0.24 N/m were oscillated at a resonance frequency of ca. 18.5 kHz with a root-mean-square amplitude of 0.5 V.

#### **5.2.4 AFM Force Measurements**

After the formation of SLBs on mica, the fluid cell was rinsed with vesicle-free electrolyte solutions to remove unadsorbed vesicles. Force measurements were thereafter taken on the SLBs at 1 or 150 mM NaCl and pH 7 (buffered with 0.4 mM NaHCO<sub>3</sub>). In order to investigate the influence of HSA on the interactions between AFM tips and SLBs, force measurements were further conducted in the presence of HSA. A 500 mg/L HSA solution at pH 7 in the presence of 1 or 150 mM NaCl was injected into the fluid cell. The system was equilibrated for 20 min before the force measurements were taken. All force measurements were taken within 2 h after the AFM tips were mounted in the fluid cell.

During each force measurement, both approach and retract force curves were recorded by the AFM. A scan rate of 0.498 Hz and ramp size of 0.5  $\mu\text{m}$  were employed, leading to a tip approaching and retracting velocity of 0.498  $\mu\text{m/s}$ . The spring constants of the cantilevers were calibrated using the thermal noise method.<sup>19</sup> The cantilever deflection versus sample displacement data was converted to force versus separation data using the method reported by Ducker et al.<sup>20</sup>

## 5.3 Results and Discussion

### 5.3.1 Formation of AgNPs on AFM Tips

Figure 5.1a illustrates the procedures for the modification of the AFM tips with AgNPs. The surface morphology of a tip that was exposed sequentially to PDA and AgNO<sub>3</sub> solutions (Ag-PDA tip) was observed with secondary electron (SE) SEM imaging (Figure 5.1b). Nanoparticles with diameters of ca. 50 nm were observed on the apex of the Ag-PDA tip.

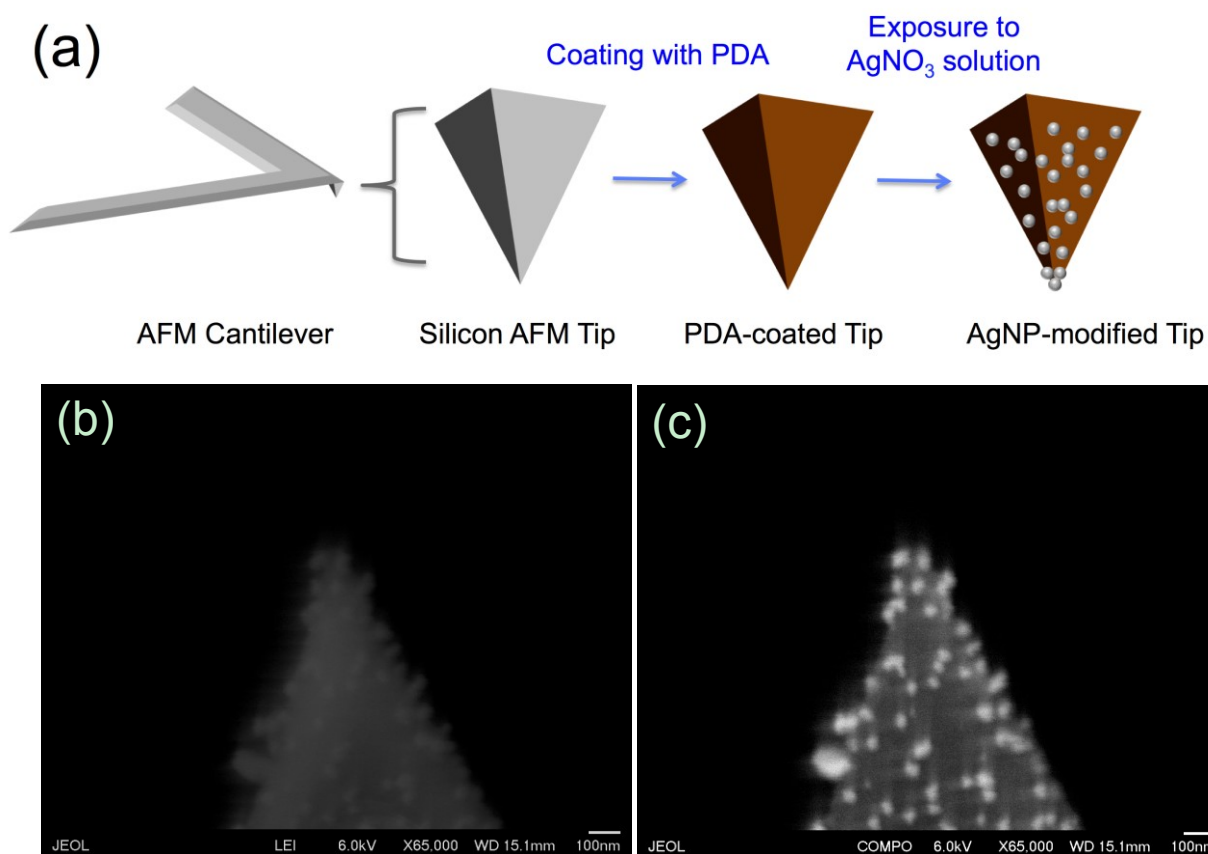


**Figure 5.1.** (a) Schematic of the modification of AFM probes with AgNPs on the apex. (b) Secondary electron image of the AgNP-modified tip. (c) Backscattered electron image of the same AgNP-modified tip showing the contrast in chemical composition on the tip.



In order to confirm that the nanoparticles formed on the tip apex were AgNPs, we collected the backscattered electron (BE) images of Ag-PDA tips (Figure 5.1c and 5.2a) as well as that of Si and PDA tips (Figure 5.2b and c). Since heavier elements (i.e., elements with higher atomic number) have a stronger ability to backscatter electrons than lighter elements, and thus appear brighter in the BE images, BE imaging can be used to reveal the contrast of regions with different surface compositions.<sup>21</sup> The BE images of both Si and PDA tips show featureless surfaces, indicating that the surface compositions of these two tips were uniform (Figure 5.2b and c). In contrast, bright spots were observed on the Ag-PDA tips (Figure 5.1c and 5.2a). Since silver has higher atomic number than the composing elements of the Si tip and PDA (C, N, and O), the presence of the bright spots on the tip likely suggest that AgNPs were formed on the tip.

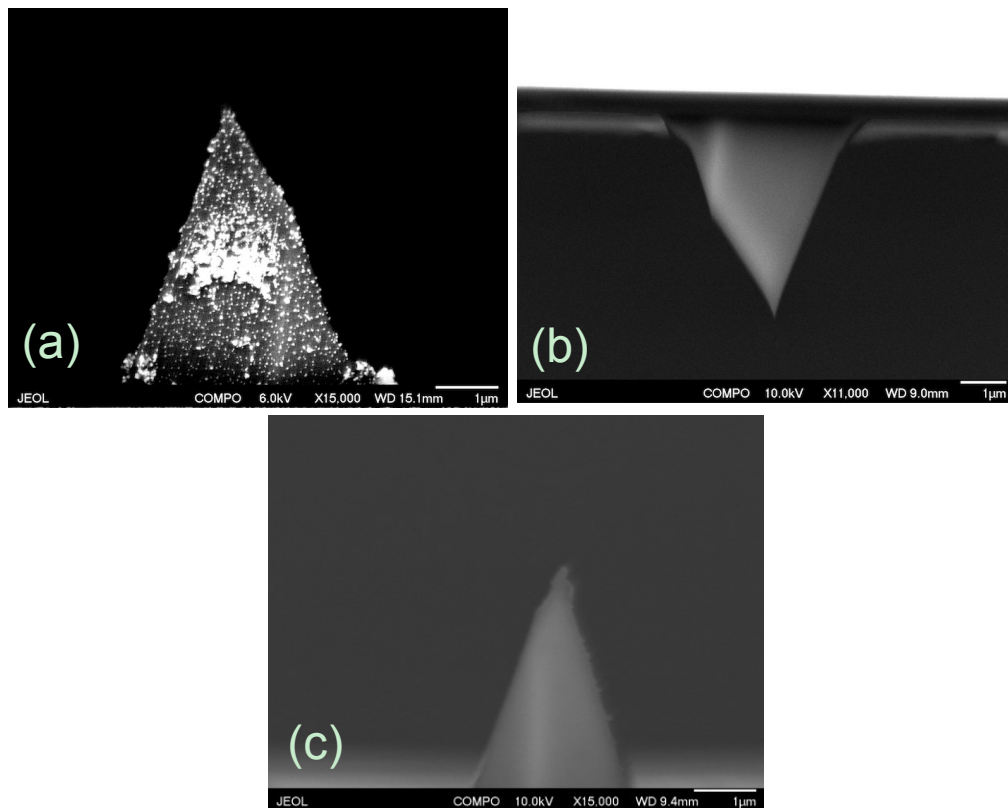


**Figure 5.2.** Backscattered electron imaging of (a) Ag-PDA (b) Si and (c) PDA tips.

Energy-dispersive X-ray spectroscopic (EDS) analysis on the tip (Figure 5.3) shows the presence of silver within those bright spots. Additional EDS analysis was performed on a PDA tip and silver was not detected (Figure 5.4). Therefore, the bright spots on the BE images of Ag-PDA tip correspond to AgNPs formed on the tip. These tips were hence referred to as AgNP tips. The formation of AgNPs on PDA film can be attributed to the binding and reduction of  $\text{Ag}^+$  ions by the catechol groups in PDA.<sup>14</sup>

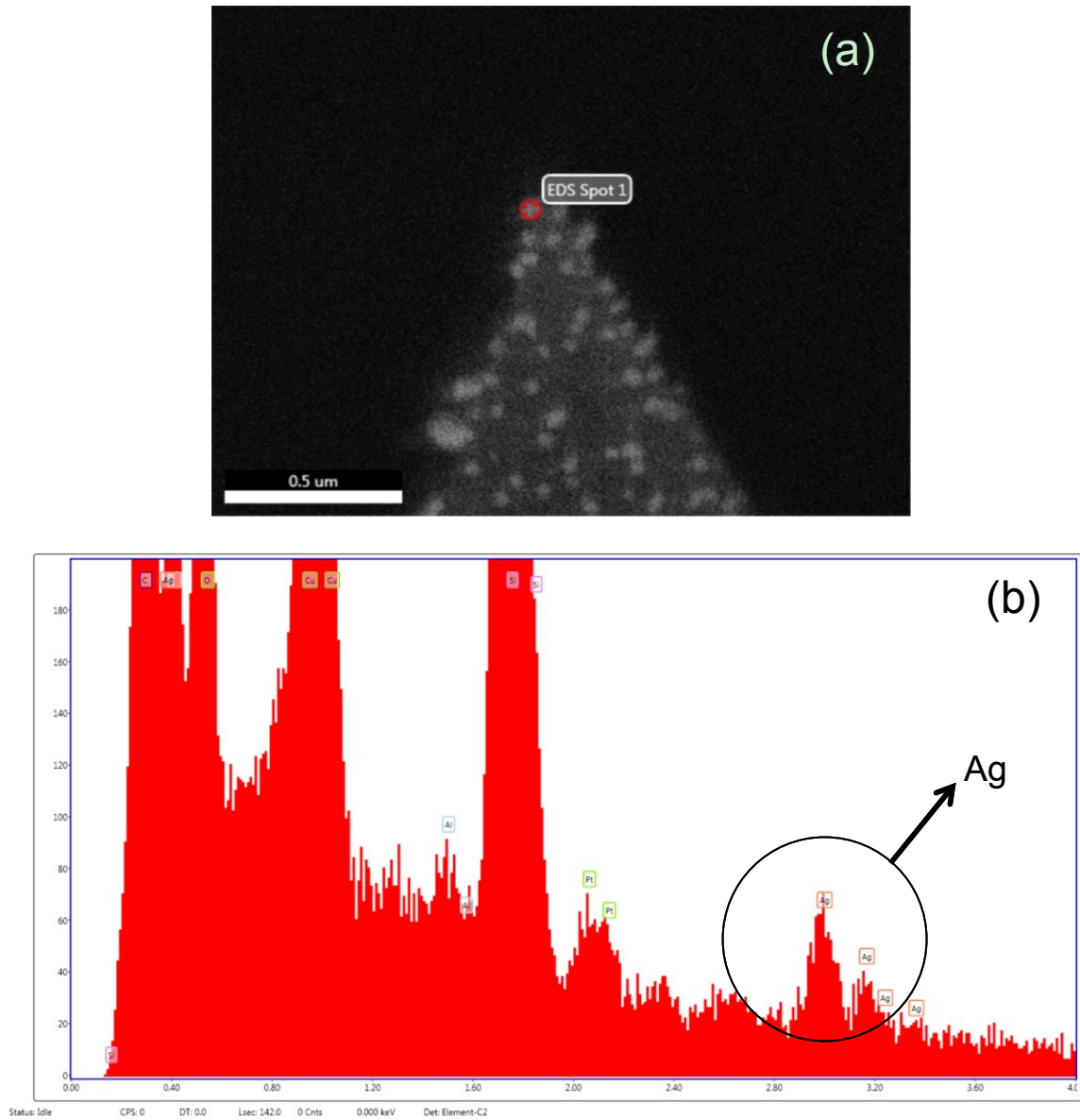


**Figure 5.3.** Backscattered electron imaging of an Ag-PDA tip (a) and the corresponding EDS analysis at a bright spot on the tip (b).

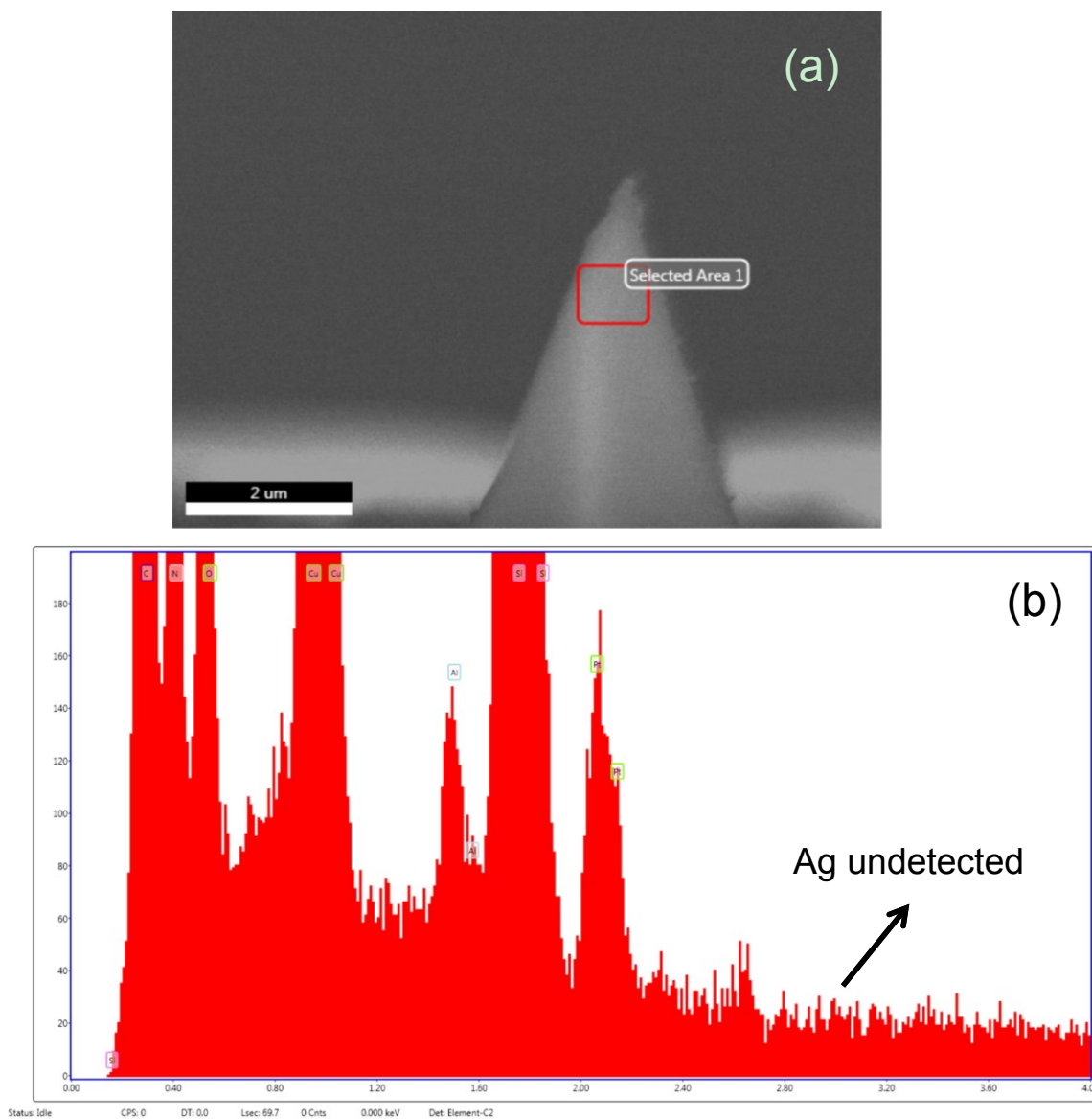


**Figure 5.4.** Backscattered electron imaging of a PDA tip (a) and the corresponding EDS analysis in a selected area on the tip (b).

In order to test the robustness of this approach to functionalizing AFM tips with AgNPs, we additionally performed SE and BE imaging on three different tips that were sequentially exposed to PDA and AgNO<sub>3</sub> (Figure 5.5). Silver nanoparticles were observed on the apex of all three tips. It is worth noting that the AgNPs formed on the tip apex were

present either as individual nanoparticles (Figure 5.1b) or as a cluster of nanoparticles (Figure 5.5a and b).

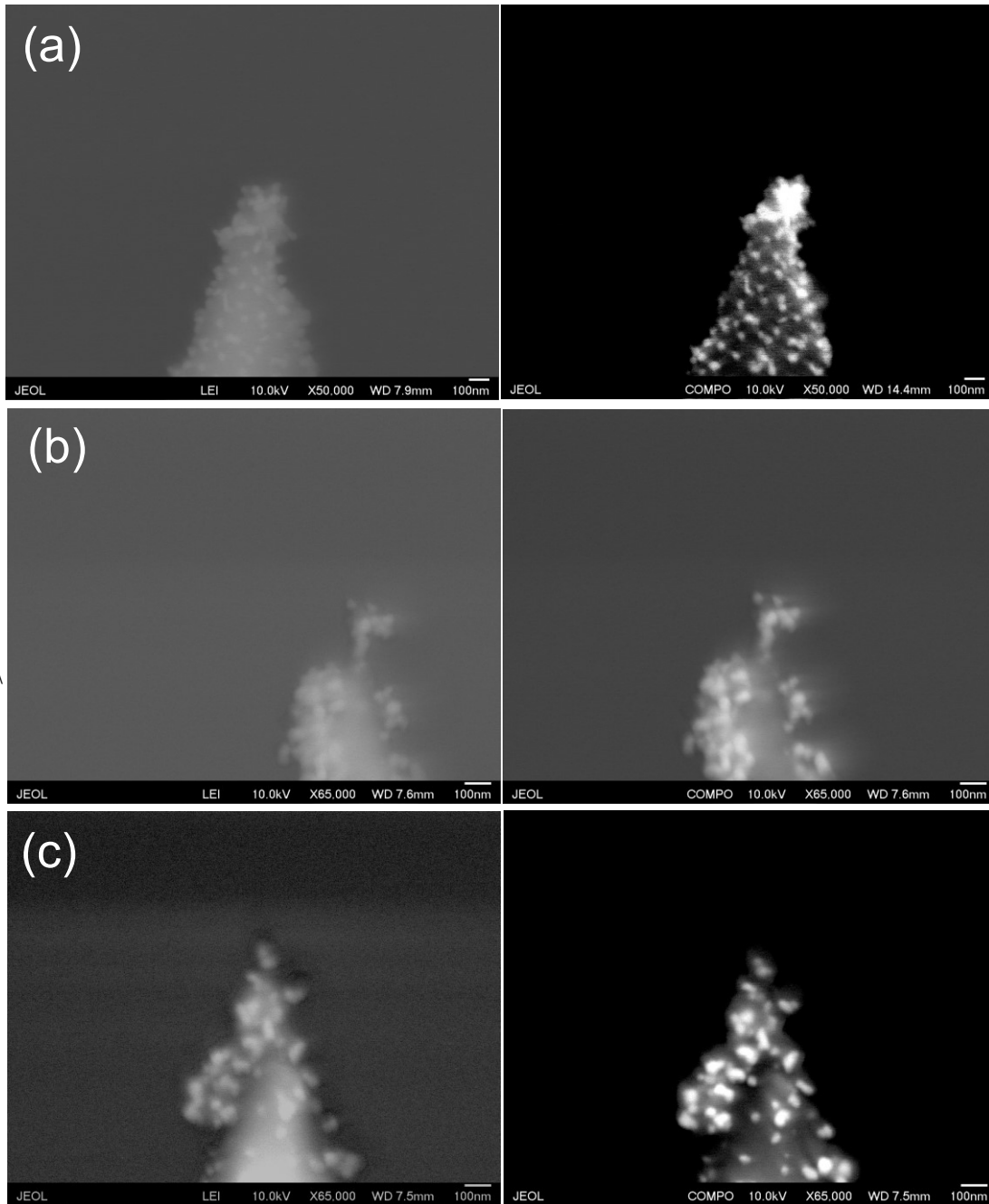


**Figure 5.5.** SEM images of three different Ag-PDA tips. The left and right panels show the secondary and backscattered electron imaging, respectively.

To further prove that the AgNPs were protruding from the PDA surface, we performed force measurements using both PDA and AgNP tips on two different surfaces (i.e., mica and SLB) at 1 mM NaCl and pH 7 (Figure 5.6 and 5.7). The work of adhesion, which is defined as the work required to pull the tips off from the surface after contact, was calculated from the retraction force curves using the trapezoidal rule.<sup>22-24</sup> On both surfaces, the work of adhesion measured using PDA and AgNP tips differ significantly (unpaired two-tailed *t*-test,  $p < 0.01$ ), thereby suggesting that the AgNPs formed on the tips were protruding from the PDA surface instead of being embedded in the PDA film.

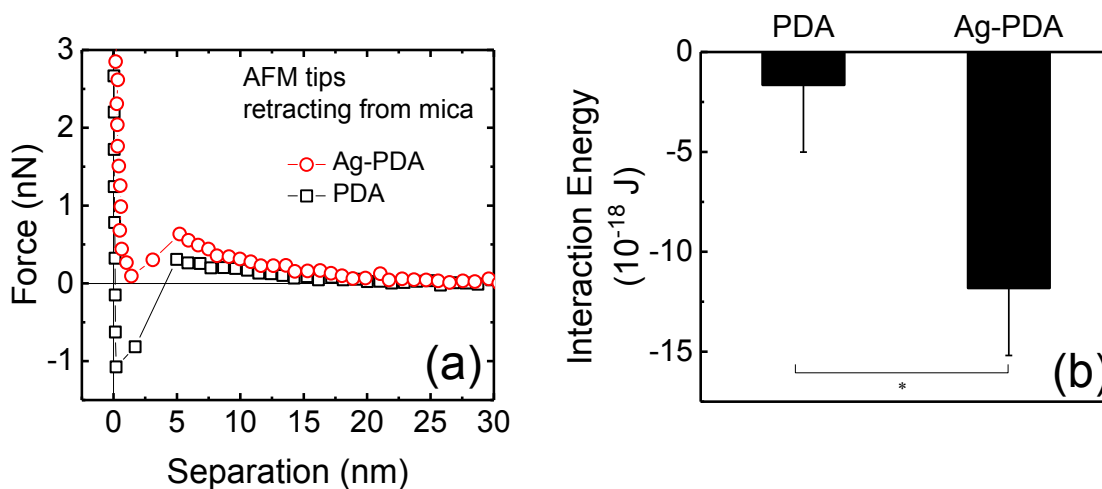


**Figure 5.6.** (a) Representative force profiles during retraction of PDA and AgNP tips from mica at 1 mM NaCl. (b) Work of adhesion for PDA and AgNP tips during retraction from mica. Positive and negative values indicate attractive and repulsive interactions, respectively. Error bars represent standard deviations ( $n = 30$ ). Asterisks (\*) indicate significant difference ( $p < 0.01$ ) between PDA and AgNP tips.

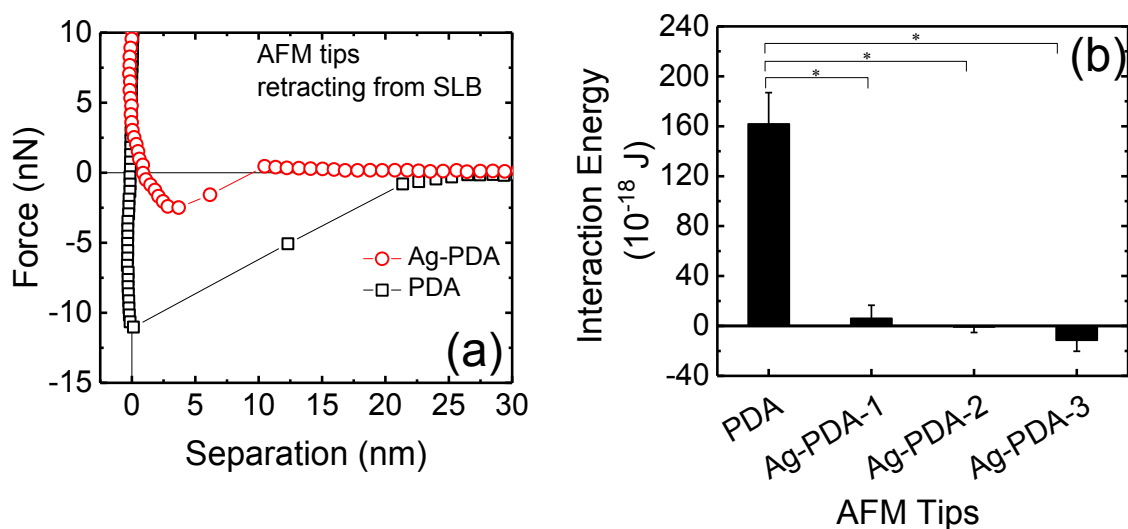


**Figure 5.7.** (a) Representative force profiles during retraction of PDA and AgNP tips from DOPC SLBs at 1 mM NaCl. (b) Work of adhesion for PDA and three different AgNP tips during retraction from SLBs. Positive and negative values indicate attractive and repulsive interactions, respectively. Error bars represent standard deviations ( $n = 30$ ). Asterisks (\*) indicate significant difference ( $p < 0.01$ ) between PDA and AgNP tips.

The AgNP-modified AFM tips are expected to hold promise in a variety of applications. For example, these tips may find application in tip-enhanced Raman spectroscopy, where AFM and surface enhanced Raman scattering are combined, to probe the chemical composition at specific sites on biological membranes.<sup>25</sup> In addition, these AgNP-modified tips can be used in the force measurements between AgNPs and environmentally relevant surfaces to gain fundamental insights into the propensity for the AgNPs to deposit on and to release from these surfaces.

### 5.3.2 Lipid Bilayers Formed on Mica for AFM Force Measurements

Through AFM imaging, the thickness of the lipid bilayer formed on mica was measured to be ca. 4 nm (Figure 5.8a and b), which is close to the reported thickness of DOPC bilayer on mica (ca. 5 nm).<sup>26</sup> A representative force curve during the approaching of

an AgNP tip toward an SLB is shown in Figure 5.8c. Herein the separation is defined as the distance between the tip and the mica substrate. When the tip was brought to a separation distance smaller than ca. 4 nm, the tip experienced increasing repulsive force most likely due to the indentation of the lipid bilayer by the tip.<sup>27</sup> A jump in the force plot was observed when the applied force exceeded a threshold, indicating that the tip penetrated through the SLBs and came into contact with the mica substrate. This sudden jump during the approaching of an AFM tip toward SLBs has been observed in previous studies.<sup>27-30</sup> In this paper, the focus will be placed on the approach force curves which can provide information about the interactions of the AgNPs with an intact (undamaged) lipid bilayer. The retraction curve, which did not display a breakthrough (Figure 5.8c), involves both AgNP-mica and AgNP-lipid interactions and thus would not reflect the true scenario of the interactions between AgNPs and cell membranes.

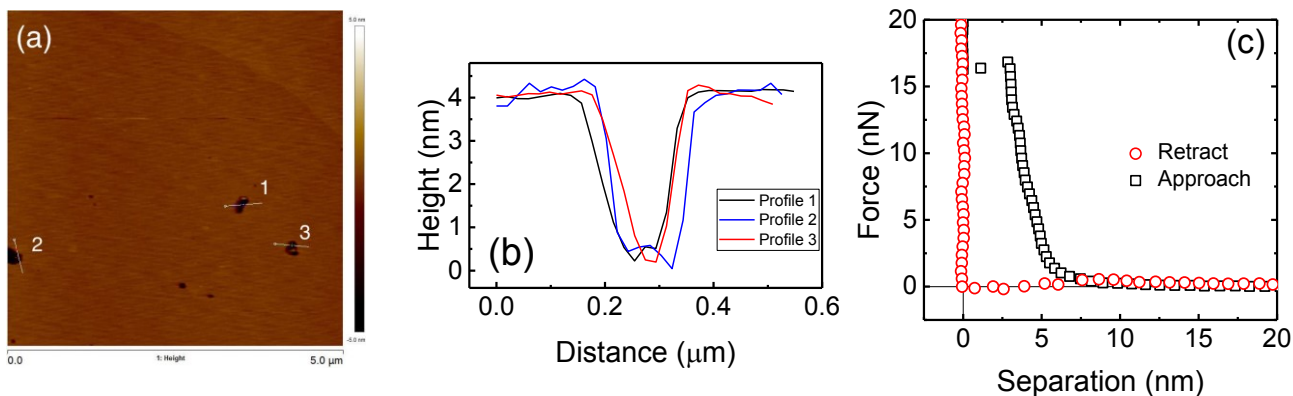


**Figure 5.8.** (a) AFM image of a mica surface covered with a DOPC lipid bilayer. (b) Height profiles of the holes within the bilayer. (c) Representative force curves during the approaching of an AgNP tip toward an SLB and the retraction of the tip from the SLB. Force measurements were conducted at 1 mM NaCl.

### 5.3.3 Presence of HSA Enhanced the Repulsion between AgNPs and Lipid Bilayers

We first examined the interaction forces between AgNPs and lipid bilayers before contact. The approach interaction forces between AgNPs and the bilayer as a function of their separation distance ( $D$ ) are presented in Figure 5.9. This separation  $D$  was calculated by subtracting the thickness of the bilayer, as determined through AFM imaging, from the separation between the tip and the mica substrate.

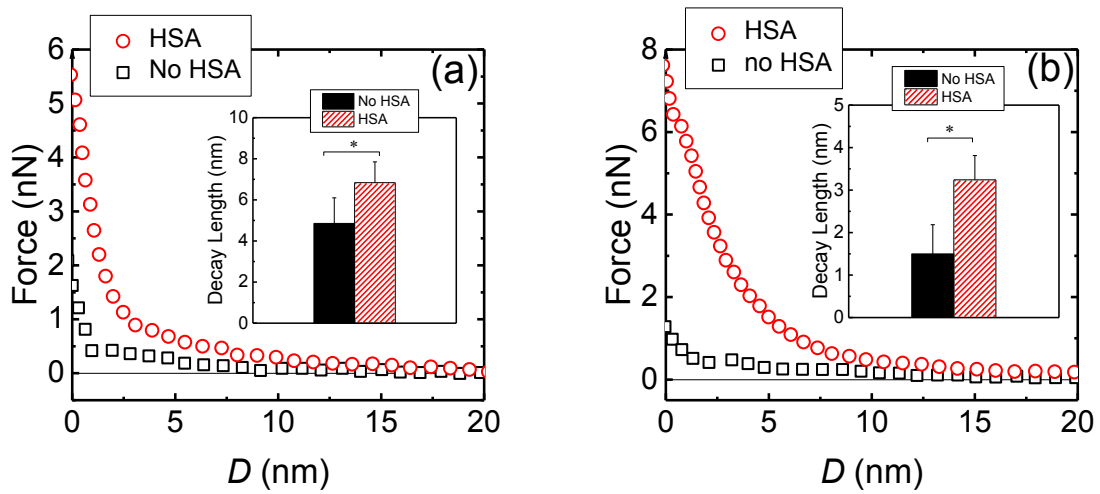


**Figure 5.9.** Representative approach force curves between AgNP tips and DOPC SLBs at (a) 1 mM NaCl and (b) 150 mM NaCl. The  $D$  in x-axis represents the distance between the tips and the surface of the lipid bilayers. Inserts show fitted decay lengths at (b) 1 mM NaCl (d) 150 mM NaCl. Error bars represent standard deviations,  $n = 30$ . Asterisks (\*) indicate significant difference ( $p < 0.01$ ) between fitted decay lengths in absence and presence of HSA.

In the absence of HSA, AgNPs experience repulsive forces during approaching to the SLB at both 1 and 150 mM. Since both AgNPs and DOPC SLBs are negatively charged at pH 7,<sup>31,32</sup> this repulsive force can be ascribed, at least in part, to electrical double layer (EDL) repulsion. We further fit the interaction force curves in absence of HSA to eq 5.1:<sup>33</sup>

$$F = Ae^{-D/\lambda} \quad (5.1)$$



where  $F$  is the interaction force in approach curve,  $A$  is a pre-exponential constant, and  $\lambda$  is the decay length. The force curves at 1 and 150 mM were fit up to separation  $D$  of 20 and 1–2 nm, respectively (Figure 5.10, in consideration of the respective long and short ranges for EDL interactions).<sup>34, 35</sup> The fitted decay length at 1 mM (ca. 4.9 nm) was larger than that at 150 mM NaCl (ca. 1.5 nm), consistent with the presence of EDL repulsion between AgNPs and SLBs.

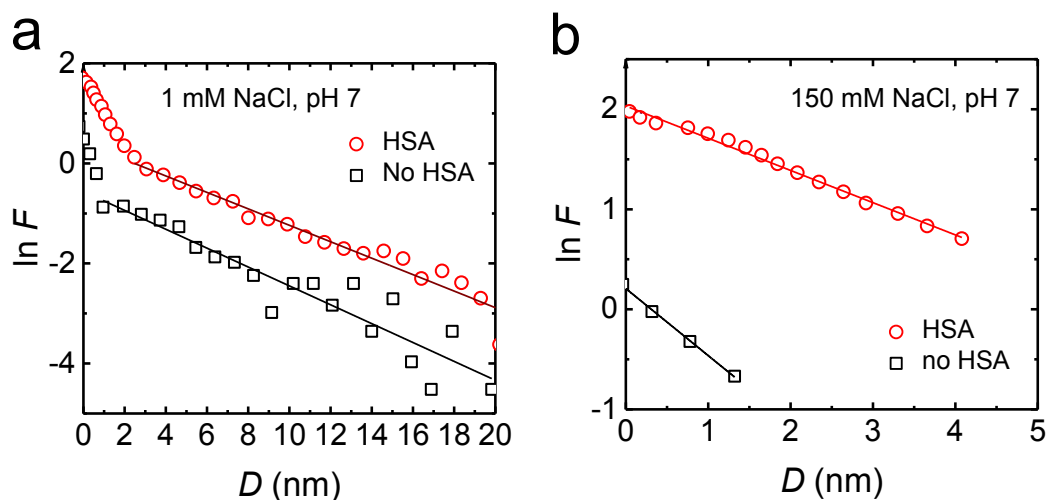


**Figure 5.10.** Semi-log plots of representative approach force curves between AgNP tips and DOPC SLBs in absence and presence of HSA at (a) 1 mM NaCl (b) 150 mM NaCl.  $D$  represents the separation between the tips and the lipid bilayer surface.

In the presence of HSA, the magnitude of the repulsive force between AgNPs and SLBs was increased at both 1 and 150 mM (Figure 5.9). The interaction force curves in presence of HSA were also fitted to eq 5.1 (Figure 5.10). The fitted decay length was significantly higher ( $p < 0.01$ ) in the presence of HSA at both 1 and 150 mM (Figure 5.9 inserts).

HSA can adsorb on the surface of AgNPs via hydrophobic interaction to form coronas.<sup>36</sup> The adsorbed HSA layer can influence the interactions between AgNPs and lipid

bilayer through two mechanisms. First, the adsorbed HSA may alter the surface charge of AgNPs thereby impacting the EDL repulsion between AgNPs and SLBs. The change in surface charge can alter the magnitude of EDL repulsion but would not result in a change in the decay length of the interaction forces.<sup>34</sup> Second, before the HSA-coated AgNPs come into contact with SLB, the chains of adsorbed HSA molecules will be compressed, which is entropically unfavorable and would give rise to a repulsive steric or electro-steric force.<sup>34</sup> The increase in the decay length in the presence of HSA provides evidence that steric (or electro-steric) repulsion was present between HSA-coated AgNPs and SLB. In their study on the interactions between silica and quartz, Borkovec and co-workers<sup>22</sup> also observed an increase in decay length in the presence of poly(ethylene imine) which they attribute to electro-steric repulsions.

The HSA molecule can be approximated as an equilateral triangular prism with a dimension of  $8 \times 8 \times 3$  nm.<sup>37,38</sup> HSA proteins can adsorb on AgNPs to form “hard” and “soft” coronas, which refer to proteins strongly bound to and loosely associated with nanoparticles, respectively.<sup>39</sup> Gebauer et al.<sup>40</sup> reported that the hard coronas formed on AgNPs consist of monolayer HSA molecules, which are expected to have a thickness of 3–8 nm. The measured decay lengths in the presence of HSA (Figure 5.9) were similar to the expected thickness of hard corona. It is thus speculated that the hard coronas formed on HSA contributed to the observed steric repulsion between AgNPs and SLBs. We do not, however, rule out the possibility that soft coronas also contributed to steric forces especially at large separation ( $> 8$  nm).

### 5.3.4 Protein Coronas Raised the Forces for AgNPs to Penetrate Lipid Bilayers

Upon contact with AFM tips, SLBs were penetrated when the force applied on the tips exceeded a threshold. This threshold, known as breakthrough force, can be understood as the maximum force the SLBs can withstand before being penetrated by the tip (Figure 5.11a).<sup>41</sup> Figure 5.11b presents the breakthrough force measured during the approaching of AgNP-tips toward SLBs in the absence and presence of HSA. A notable observation is that the presence of HSA increased the breakthrough forces at both 1 and 150 mM NaCl (Figure 5.11b). Angle et al.<sup>42</sup> have shown that the breakthrough forces on an SLB depend on the geometry of the tip when other conditions remain the same. Lower breakthrough forces were measured using sharper tips (i.e., tips with smaller radius of curvature) because higher local pressure will be exerted on the SLB by sharper tips under the same applied forces.<sup>42</sup>

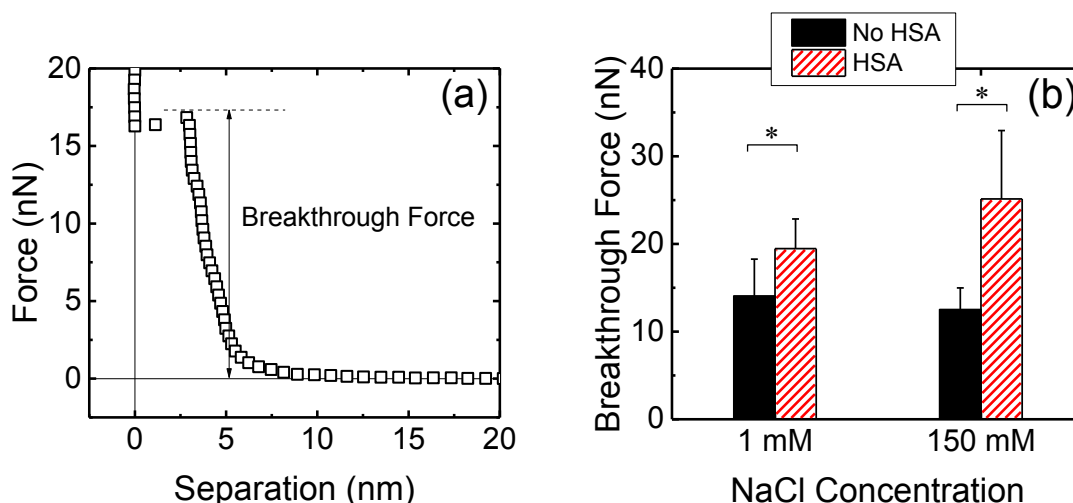


**Figure 5.11.** (A) Representative approach force curves between an Ag-NP tip and an SLB at 1 mM NaCl. The separation represents the distance between the tip and the mica substrate. (b) Forces required for AgNP tips to penetrate DOPC SLBs in absence and presence of HSA. Error bars represent standard deviations ( $n = 30$ ). Asterisks (\*) indicate significant difference ( $p < 0.01$ ) between penetration forces in absence and presence of HSA measured using the same tip.

In their study of the interactions of HSA with AgNPs, Chen et al.<sup>36</sup> observed through transmission electron microscopy that protein coronas were formed around the AgNPs after the nanoparticles were incubated with a ca. 480 mg/L HSA solution overnight. They reported that the diameter of the AgNPs increased from ca. 30 to 80 nm after HSA adsorption.<sup>36</sup> Since the HSA concentration used in this study (500 mg/L) is close to that used by Chen et al., it is likely that the diameters of AgNPs on the AFM tips were increased upon the formation of protein coronas, thereby resulting in a higher breakthrough force during the approach to the SLBs.

### 5.3.5 Implications

In summary, we have developed a facile approach to modifying AFM tips *in situ* with AgNPs. This method can potentially be used to functionalize AFM tips with other metal (e.g., copper and gold) nanoparticles through the binding and reduction of metal ions by polydopamine.<sup>14,43</sup> Our force measurements show that the presence of protein coronas give rise to steric repulsion between AgNPs and SLBs. This observation possibly implies that the hemolytic activity of AgNPs<sup>6</sup> may be reduced upon formation of protein coronas which inhibit the direct contact between AgNPs and cell membranes. We also demonstrate that the forces required for AgNPs to penetrate lipid bilayers were increased in the presence of proteins. This finding suggests that the cellular uptake of AgNPs via membrane penetration may be hindered by protein coronas formed on the nanoparticles.

## 5.4 References

1. Echegoyen, Y.; Nerin, C., Nanoparticle release from nano-silver antimicrobial food containers. *Food Chem. Toxicol.* **2013**, *62*, 16-22.

2. Frohlich, E.; Roblegg, E., Models for oral uptake of nanoparticles in consumer products. *Toxicology* **2012**, *291*, (1-3), 10-17.
3. Wilkinson, L. J.; White, R. J.; Chipman, J. K., Silver and nanoparticles of silver in wound dressings: a review of efficacy and safety. *Journal of Wound Care* **2011**, *20*, (11), 543-549.
4. AshaRani, P. V.; Mun, G. L. K.; Hande, M. P.; Valiyaveetil, S., Cytotoxicity and Genotoxicity of Silver Nanoparticles in Human Cells. *ACS Nano* **2009**, *3*, (2), 279-290.
5. Choi, J.; Reipa, V.; Hitchins, V. M.; Goering, P. L.; Malinauskas, R. A., Physicochemical Characterization and In Vitro Hemolysis Evaluation of Silver Nanoparticles. *Toxicol. Sci.* **2011**, *123*, (1), 133-143.
6. Asharani, P. V.; Sethu, S.; Vadukumpully, S.; Zhong, S. P.; Lim, C. T.; Hande, M. P.; Valiyaveetil, S., Investigations on the Structural Damage in Human Erythrocytes Exposed to Silver, Gold, and Platinum Nanoparticles. *Adv. Funct. Mater.* **2010**, *20*, (8), 1233-1242.
7. De Matteis, V.; Malvindi, M. A.; Galeone, A.; Brunetti, V.; De Luca, E.; Kote, S.; Kshirsagar, P.; Sabella, S.; Bardi, G.; Pompa, P. P., Negligible particle-specific toxicity mechanism of silver nanoparticles: The role of Ag<sup>+</sup> ion release in the cytosol. *Nanomed-Nanotechnol* **2015**, *11*, (3), 731-739.
8. Lesniak, A.; Salvati, A.; Santos-Martinez, M. J.; Radomski, M. W.; Dawson, K. A.; Aberg, C., Nanoparticle adhesion to the cell membrane and its effect on nanoparticle uptake efficiency. *J. Am. Chem. Soc.* **2013**, *135*, (4), 1438-44.
9. Yuan, H. Y.; Li, J.; Bao, G.; Zhang, S. L., Variable Nanoparticle-Cell Adhesion Strength Regulates Cellular Uptake. *Phys. Rev. Lett.* **2010**, *105*, (13).
10. Piao, M. J.; Kang, K. A.; Lee, I. K.; Kim, H. S.; Kim, S.; Choi, J. Y.; Choi, J.; Hyun, J. W., Silver nanoparticles induce oxidative cell damage in human liver cells through inhibition of reduced glutathione and induction of mitochondria-involved apoptosis. *Toxicol. Lett.* **2011**, *201*, (1), 92-100.
11. Wang, Q. Y.; Lim, M. H.; Liu, X. T.; Wang, Z. W.; Chen, K. L., Influence of Solution Chemistry and Soft Protein Coronas on the Interactions of Silver Nanoparticles with Model Biological Membranes. *Environ. Sci. Technol.* **2016**, *50*, (5), 2301-2309.
12. Chen, K. L.; Bothun, G. D., Nanoparticles Meet Cell Membranes: Probing Nonspecific Interactions. using Model Membranes. *Environ. Sci. Technol.* **2014**, *48*, (2), 873-880.
13. Pyrgiotakis, G.; Blattmann, C. O.; Demokritou, P., Real-Time Nanoparticle-Cell Interactions in Physiological Media by Atomic Force Microscopy. *ACS Sustainable Chem. Eng.* **2014**, *2*, (7), 1681-1690.
14. Lee, H.; Dellatore, S. M.; Miller, W. M.; Messersmith, P. B., Mussel-inspired surface chemistry for multifunctional coatings. *Science* **2007**, *318*, (5849), 426-430.
15. Romero-Vargas Castrillón, S.; Perreault, F.; de Faria, A. F.; Elimelech, M., Interaction of Graphene Oxide with Bacterial Cell Membranes: Insights from Force Spectroscopy. *Environ. Sci. Technol. Lett.* **2015**, *2*, (4), 112-117.
16. Wang, R. S. E.; Tian, L.; Chang, Y. H., A homogeneous fluorescent sensor for human serum albumin. *J. Pharm. Biomed. Anal.* **2012**, *63*, 165-169.
17. Mayer, L. D.; Hope, M. J.; Cullis, P. R., Vesicles of Variable Sizes Produced by a Rapid Extrusion Procedure. *Biochim. Biophys. Acta* **1986**, *858*, (1), 161-168.
18. Richter, R. P.; Berat, R.; Brisson, A. R., Formation of solid-supported lipid bilayers: An integrated view. *Langmuir* **2006**, *22*, (8), 3497-3505.

19. Hutter, J. L.; Bechhoefer, J., Calibration of Atomic-Force Microscope Tips. *Rev. Sci. Instrum.* **1993**, *64*, (7), 1868-1873.
20. Ducker, W. A.; Senden, T. J.; Pashley, R. M., Measurement of Forces in Liquids Using a Force Microscope. *Langmuir* **1992**, *8*, (7), 1831-1836.
21. Goldstein, J.; Newbury, D. E.; Echlin, P.; Joy, D. C.; Romig Jr, A. D.; Lyman, C. E.; Fiori, C.; Lifshin, E., *Scanning electron microscopy and X-ray microanalysis: a text for biologists, materials scientists, and geologists*. Springer Science & Business Media: 2012.
22. Pericet-Camara, R.; Papastavrou, G.; Behrens, S. H.; Helm, C. A.; Borkovec, M., Interaction forces and molecular adhesion between pre-adsorbed poly(ethylene imine) layers. *J. Colloid Interface Sci.* **2006**, *296*, (2), 496-506.
23. Chen, K. L.; Mylon, S. E.; Elimelech, M., Enhanced aggregation of alginate-coated iron oxide (hematite) nanoparticles in the presence of calcium, strontium, and barium cations. *Langmuir* **2007**, *23*, (11), 5920-5928.
24. Tang, L.; Gu, W. Y.; Yi, P.; Bitter, J. L.; Hong, J. Y.; Fairbrother, D. H.; Chen, K. L., Bacterial anti-adhesive properties of polysulfone membranes modified with polyelectrolyte multilayers. *J. Membr. Sci.* **2013**, *446*, 201-211.
25. Neugebauer, U.; Rosch, P.; Schmitt, M.; Popp, J.; Julien, C.; Rasmussen, A.; Budich, C.; Deckert, V., On the way to nanometer-sized information of the bacterial surface by tip-enhanced Raman spectroscopy. *ChemPhysChem* **2006**, *7*, (7), 1428-1430.
26. Lei, H. Z.; Zhou, X. J.; Wu, H. X.; Song, Y.; Hu, J.; Guo, S. W.; Zhang, Y., Morphology Change and Detachment of Lipid Bilayers from the Mica Substrate Driven by Graphene Oxide Sheets. *Langmuir* **2014**, *30*, (16), 4678-4683.
27. Li, J. K.; Sullan, R. M. A.; Zou, S., Atomic Force Microscopy Force Mapping in the Study of Supported Lipid Bilayers. *Langmuir* **2011**, *27*, (4), 1308-1313.
28. Garcia-Manyes, S.; Oncins, G.; Sanz, F., Effect of temperature on the nanomechanics of lipid bilayers studied by force spectroscopy. *Biophys. J.* **2005**, *89*, (6), 4261-4274.
29. Franz, V.; Loi, S.; Muller, H.; Bamberg, E.; Butt, H. H., Tip penetration through lipid bilayers in atomic force microscopy. *Colloid Surface B* **2002**, *23*, (2-3), 191-200.
30. Garcia-Manyes, S.; Redondo-Morata, L.; Oncins, G.; Sanz, F., Nanomechanics of Lipid Bilayers: Heads or Tails? *J. Am. Chem. Soc.* **2010**, *132*, (37), 12874-12886.
31. El Badawy, A. M.; Luxton, T. P.; Silva, R. G.; Scheckel, K. G.; Suidan, M. T.; Tolaymat, T. M., Impact of Environmental Conditions (pH, Ionic Strength, and Electrolyte Type) on the Surface Charge and Aggregation of Silver Nanoparticles Suspensions. *Environ. Sci. Technol.* **2010**, *44*, (4), 1260-1266.
32. Yi, P.; Chen, K. L., Interaction of Multiwalled Carbon Nanotubes with Supported Lipid Bilayers and Vesicles as Model Biological Membranes. *Environ. Sci. Technol.* **2013**, *47*, (11), 5711-5719.
33. Butt, H. J.; Kappl, M.; Mueller, H.; Raiteri, R.; Meyer, W.; Ruhe, J., Steric forces measured with the atomic force microscope at various temperatures. *Langmuir* **1999**, *15*, (7), 2559-2565.
34. Israelachvili, J. N., *Intermolecular and surface forces: revised third edition*. Academic press: 2011.
35. Elimelech, M. G., J.; Jia, X.; Williams, R. A., *Particle Deposition and Aggregation: Measurement, Modelling and Simulation*. Butterworth-Heinemann: Oxford: England, 1995.

36. Chen, R.; Choudhary, P.; Schurr, R. N.; Bhattacharya, P.; Brown, J. M.; Ke, P. C., Interaction of lipid vesicle with silver nanoparticle-serum albumin protein corona. *Appl. Phys. Lett.* **2012**, *100*, (1).
37. Rocker, C.; Potzl, M.; Zhang, F.; Parak, W. J.; Nienhaus, G. U., A quantitative fluorescence study of protein monolayer formation on colloidal nanoparticles. *Nat. Nanotechnol.* **2009**, *4*, (9), 577-580.
38. Sugio, S.; Kashima, A.; Mochizuki, S.; Noda, M.; Kobayashi, K., Crystal structure of human serum albumin at 2.5 angstrom resolution. *Protein Eng.* **1999**, *12*, (6), 439-446.
39. Lundqvist, M.; Stigler, J.; Elia, G.; Lynch, I.; Cedervall, T.; Dawson, K. A., Nanoparticle size and surface properties determine the protein corona with possible implications for biological impacts. *Proc. Natl. Acad. Sci. U. S. A.* **2008**, *105*, (38), 14265-14270.
40. Gebauer, J. S.; Malissek, M.; Simon, S.; Knauer, S. K.; Maskos, M.; Stauber, R. H.; Peukert, W.; Treuel, L., Impact of the Nanoparticle-Protein Corona on Colloidal Stability and Protein Structure. *Langmuir* **2012**, *28*, (25), 9673-9679.
41. Garcia-Manyes, S.; Oncins, G.; Sanz, F., Effect of ion-binding and chemical phospholipid structure on the nanomechanics of lipid bilayers studied by force spectroscopy. *Biophys. J.* **2005**, *89*, (3), 1812-1826.
42. Angle, M. R.; Wang, A.; Thomas, A.; Schaefer, A. T.; Melosh, N. A., Penetration of Cell Membranes and Synthetic Lipid Bilayers by Nanoprobes. *Biophys. J.* **2014**, *107*, (9), 2091-2100.
43. Zeng, T.; Zhang, X. L.; Niu, H. Y.; Ma, Y. R.; Li, W. H.; Cai, Y. Q., In situ growth of gold nanoparticles onto polydopamine-encapsulated magnetic microspheres for catalytic reduction of nitrobenzene. *Applied Catalysis B-Environmental* **2013**, *134*, 26-33.

**Chapter 6. Conclusions, Engineering Significance,  
and Future Work**



## 6.1 Conclusions

In this dissertation, the influence of solution chemistry and presence of protein coronas on the interactions of GO with model cell membranes was examined in Chapters 2 and 3. Chapter 4 focuses on the effect of phosphate adsorption on the aggregation and interactions of CMP nanoparticles with model cell membranes. In Chapter 5, a facial approach to functionalizing AFM tips with AgNPs was developed, and the interaction forces between AgNPs and lipid bilayers were measured.

In Chapter 2, the propensity for GO to attach to and disrupt model cell membranes was examined using SLBs and SVLs. The deposition kinetics of GO on DOPC SLBs at neutral pH were observed to increase with increasing electrolyte (NaCl and CaCl<sub>2</sub>) concentrations, demonstrating the critical role of electrostatic interactions in controlling GO attachment. The deposition kinetics of GO on negatively charged DOPC SLBs and positively charged DOPC-DOEPC SLBs at elevated electrolyte concentrations were both lower than mass-transfer-limited kinetics, likely due to the presence of hydration forces between GO and SLBs. Upon favorable GO deposition to DOPC SLBs at 1.1 mM CaCl<sub>2</sub> at pH 7, no GO release was observed when the deposited GO was rinsed with DI water at the same pH, implying that the deposition of GO was largely irreversible. Upon the attachment of GO to supported vesicles that were encapsulated with a fluorescent dye, dye leakage was detected, thus indicating that the lipid vesicles were disrupted by GO. When the exposure of the SVL to the GO suspension was terminated, the leakage of dye dropped precipitously, demonstrating that the pores formed on the lipid bilayers have a self-repairing ability. This self-healing of pores was attributed to the decrease in membrane tension due to the release of

fluid and the further dominance of line tension (excess free energy per unit length of the pore edge) which drives pore closure. No dye leakage was observed upon exposure of the supported vesicles to GO suspension when the deposition of GO to SLBs was unfavorable (1 mM NaCl and pH 7), thereby providing direct evidence that the attachment of GO was a crucial step for the disruption of the vesicles.

In Chapter 3, the adsorption of HSA on GO was examined and the influence of HSA adsorption on GO attachment to DOPC SLBs was explored. QCM-D sensors were coated by GO layers through sequentially exposing the sensors to a PLL solution and a GO suspension. The absolute (dry) mass of HSA adsorption was studied through batch adsorption experiments, and the wet mass of HSA layer on GO was estimated from QCM-D measurements based on Sauerbrey model. The absolute mass of HSA adsorption increased with raising ionic strength at neutral pH. The adsorbed HSA layer was more rigid at higher ionic strength conditions, likely due to the decrease in magnitude of the net charge of HSA and more favorable lateral interactions between adsorbed HSA. Calcium ions increased HSA adsorption on GO which is likely attributed to the binding of calcium to the carboxyl groups of GO and HSA to result in charge neutralization. At physiological ionic strength (150 mM), the dry mass of HSA adsorption reaches maximum value at the IEP of HSA. Under this condition, the adsorbed HSA layer was the most compact likely owing to the favorable interactions between adsorbed HSA. Under acidic conditions (pH 2.0), the adsorbed HSA layer was highly fluid due to the extended conformations of HSA under this condition. Finally, the attachment of GO to DOPC SLBs was inhibited by HSA adsorption, and the degree of inhibition was higher when the HSA layer was more fluid.

In chapter 4, the adsorption of phosphate ions, a key constituent in human serum and saliva, on four CMP nanoparticles was investigated. Phosphate adsorbed on ceria and alumina nanoparticles appreciably, resulting in an enhancement in the negative charge of ceria and a reversal of the charge of alumina from positive to negative. The colloidal stability of both ceria and alumina nanoparticles was enhanced in the presence of phosphate ions at neutral pH. The attachment kinetics of ceria and alumina to DOPC SLBs was greatly reduced in the presence of phosphate due to the elevation in the electrostatic repulsion between the nanoparticles and SLBs. The deposition of ceria and alumina nanoparticles on SLBs was not detected at neutral pH and NaCl concentrations lower than 200 mM in the presence of phosphate. The adsorption of phosphate on both colloidal and fumed silica nanoparticles was found to be negligible, and, consequently, the colloidal stability of the silica nanoparticles and their attachment to SLBs were not significantly influenced by the presence of phosphate ions. The colloidal and fumed silica nanoparticles were found to be remarkably stable at neutral pH conditions both in the presence and absence of phosphate, likely due to the presence of a hairy layer of protruding silanol and silicic acid groups on the nanoparticle surface which give rise to steric repulsion between nanoparticles. The attachment efficiencies of both silica nanoparticles on SLBs increased to one when the NaCl concentration was raised to 100 mM in the presence of phosphate. Furthermore, the attachment of colloidal and fumed silica nanoparticles to fluorescent-dye-encapsulated DOPC SVLs did not result in detectable leakage of dye, indicating that the nanoparticles did not cause significant disruption of the vesicles.

In Chapter 5, the interactions between AgNPs and SLBs were probed using AFM force measurements. A facile approach to modifying AFM tips with AgNPs was developed

based on the reduction of silver ions by the catechol groups in PDA. By successively exposing the AFM tips to a 2 g/L PDA solution for 45 min and a 500 mM silver nitrate solution for 16 h, AgNPs were formed on the apex of the tips as confirmed through secondary and backscattered electron SEM imaging. Control force measurements on mica and SLB surface using both PDA-modified and AgNP-modified tips suggest that the AgNPs were protruding from the surface of the PDA layer. During the approaching of AgNP-modified tips toward SLBs at pH 7, the AgNPs experience predominantly repulsive forces at both 1 and 150 mM NaCl likely owing to electrostatic interactions. The presence of HSA increased the magnitude of this repulsive force between AgNPs and SLBs. By fitting the force-separation curves to an exponential decay equation, the decay length of the repulsive forces at both 1 and 150 mM NaCl was found to be larger in the presence of HSA. This observation suggests that the adsorption of HSA to AgNPs likely gives rise to steric or electrosteric repulsion between AgNPs and SLBs. Furthermore, the forces required for the AgNPs to penetrate SLBs were higher in the presence of HSA at both 1 and 150 mM NaCl, probably stemming from the increased size of the AgNPs as a result of HSA adsorption.

## **6.2 Key Contributions and Engineering Significance**

In this dissertation work, the physicochemical interactions between engineered nanoparticles and model cell membranes were investigated in terms of nanoparticle attachment, lipid membrane disruption, and nanoparticle-membrane force interactions. Specific emphasis has been placed on the influence of human serum albumin and phosphate ions, which are key constituents in human serum and saliva, on these nanoparticle-membrane

interactions. New insights have been provided into the disruption of lipid membranes by nanoparticles. The specific contributions of this dissertation are described below:

- **Demonstrated for the first time that the disruption of lipid membranes caused by GO can be self-healed.** GO nanosheets were shown to cause the formation of pores on lipid membranes when the conditions for GO attachment were favorable. When the exposure of lipid vesicles to GO was terminated, the pores were self-healed. This result provides new insights into the cytotoxicity of GO toward mammalian and bacterial cells. During the design of GO based antibacterial materials and the evaluation of the cytotoxicity of GO toward human cell lines, this potential reversibility of lipid membrane disruption should be taken into consideration.
- **Provided evidence that the attachment of GO to lipid bilayers can be inhibited by the presence of protein coronas on GO and the degree of inhibition is dependent on the conformation of coronas.** HSA proteins can adsorb on GO to form protein coronas. The amount of HSA adsorbed and the conformation of HSA layers have been shown to be dependent on solution chemistry. The attachment of GO to lipid bilayers was reduced in the presence of HSA proteins due to the formation of protein coronas on GO. The degree of reduction in attachment was influenced by the fluidity of the hard protein coronas around GO. When GO is transported between different biological compartments, the change in solution chemistry can result in an alteration in the conformation of the protein coronas on GO. To evaluate the biological impacts of GO-based drug delivery agents, the

adsorption of proteins on GO must be accounted for to enable better understanding of the interactions of GO with human cell membranes.

- **Demonstrated for the first time that the adsorption of phosphate can significantly reduce the attachment of nanoparticles to lipid bilayers.** Phosphate ions were shown to adsorb appreciably on ceria and alumina nanoparticles and impart additional negative charge to the nanoparticles. As a result, the attachment of the nanoparticles to negatively charged lipid bilayers was substantially reduced. The presence of phosphate did not significantly influence the attachment of silica nanoparticles, on which the adsorption of phosphate was negligible, to lipid bilayers. This finding identified the key role of an inorganic constituent of biological fluids in determining the surface properties of and the cellular responses to inorganic nanomaterials. Depending on the affinity between phosphate ions and the nanoparticles, the nanoparticles may either retain their original surface charge or become more negatively charged. The change in surface charge properties of nanoparticles would result in alterations in the interactions of the nanoparticles with biological components and may subsequently influence the cytotoxicity of the nanoparticles.
- **Developed a facile approach to modifying AFM tips *in situ* with AgNPs.** AFM tips were functionalized with AgNPs by successively exposing the tips to PDA and silver nitrate solutions. This approach may also be used to modify AFM tips with a variety of metal nanoparticles (e.g., gold and copper) through the reduction of metal ions by polydopamine. The AgNP-modified AFM tips may potentially be employed to probe the interactions of AgNPs with a wide range of environmentally relevant

surfaces, such as silica and biofilm, to mechanistically understand the propensity for AgNPs to deposit on these surfaces, thereby enabling better prediction of the fate and transport of AgNPs in the environment.

- **Delineated the interaction forces between AgNPs and lipid bilayers in the absence and presence of protein coronas.** The interactions between AgNPs and negatively charged DOPC lipid bilayers were measured to be predominantly repulsive at neutral pH conditions. The presence of protein coronas imparts additional steric (or electrosteric) repulsive forces between the AgNPs and lipid bilayers. Therefore, the role of protein adsorption in determining nanoparticle-membrane interactions must be accounted for during the assessment of the negative impacts of AgNPs on human health.

The list of publications and expected publications from this dissertation work is presented below:

- 1) Liu, X. T. and Chen, K. L., Interactions of Graphene Oxide with Model Cell Membranes: Probing Nanoparticle Attachment and Lipid Bilayer Disruption, *Langmuir*, 2015, 31, 12076–12086. (Chapter 2)
- 2) Liu, X. T. and Chen, K. L., Aggregation and Interactions of Chemical Mechanical Planarization Nanoparticles with Model Biological Membranes: Role of Phosphate Adsorption, *Environmental Science: Nano*, 2016, 3, 146–156. (Chapter 4)
- 3) Liu, X. T., Yan, C. X., and Chen, K. L., Adsorption of Human Serum Albumin on Graphene Oxide: Implications for Protein Corona Formation and Conformation (in preparation). (Chapter 3)

4) Liu, X. T. and Chen, K. L., Silver Nanoparticles Formed *In Situ* on AFM Tips for Force Measurements with Model Cell Membranes: Influence of Protein Coronas (in preparation). (Chapter 5)

### **6.3 Future Work**

The model cell membranes employed in this study consist of single or binary phospholipids and thus are oversimplified models for cell membranes which contain a variety of phospholipids, sphingolipids, cholesterol, and membrane proteins. It is of considerable interest to build models that have similar composition to biological membranes. In addition, different from the SLBs employed in this research which are laterally homogeneous in terms of lipid packing, cell membranes are laterally organized and contain lipid rafts, which are segregated microdomains enriched in sphingolipids and cholesterol. The roles of sphingolipids, cholesterol, membrane proteins, and the presence of lipid rafts in determining nanoparticle-membrane interactions warrant further investigation.

In this research, some efforts have been devoted to understanding the influence of inorganic and organic constituents of biological fluids on nanoparticle-membrane interactions. Real biological fluids are often highly complex, containing a variety of components including mono- and multi-valent electrolytes, lipids, and proteins. These components can adsorb on nanoparticles, thereby resulting in a change in the surface properties of the nanoparticles. In addition, nanoparticles may undergo a wide range of transformations in biological fluids including dissolution, aggregation, oxidation, and reduction. Further studies that involve the use of more realistic biological media and the monitoring of change in the physicochemical properties of nanoparticles over time will



enable holistic understanding of the interactions between the nanoparticles and cell membranes.

Although the physical damage to cell membranes has been proposed as an important pathway for the cytotoxicity of a range of nanoparticles, other pathways (e.g., oxidative stress) are often operative simultaneously, further impeding the elucidation of the underlying mechanisms for nanoparticle cytotoxicity. Comparison of the cytotoxicity studies that involve the use of different human cell lines is often complicated by the diversity of toxicity testing protocols used across different studies. Model cell membranes can provide mechanistic insights into nanoparticle-membrane interactions at a molecular level. One promising, but currently underexplored, area is to establish the correlation between the nanoparticle-membrane interactions obtained using model membranes and the cytotoxicity studies based on the use of human cell lines. This type of research is expected to expedite the elucidation of the underlying mechanisms for the adverse impacts of nanoparticles on biological systems.

## CURRICULUM VITAE

### Xitong Liu

[xtliu@jhu.edu](mailto:xtliu@jhu.edu) 410-227-9238

Department of Environmental Health and Engineering, Johns Hopkins University  
Ames Hall 313, 3400 North Charles Street, Baltimore, MD 21218

### Education

*Johns Hopkins University, Department of Environmental Health and Engineering*

Ph.D. student, 2013–2017

Advisor: Professor Kai Loon Chen

Dissertation title: “Physicochemical Interactions of Engineered Nanomaterials with Model Biological Membranes”

*Nanjing University, Department of Environmental Engineering*

Master of Engineering, 2010–2013

Advisors: Professors Shujuan Zhang and Bingcai Pan

Dissertation title: “Diketone-activated Photodegradation of Organic Dyes in Aqueous Solutions: Behaviors and Mechanisms”

*Nanjing University, Department of Environmental Engineering*

Bachelor of Engineering, 2006–2010

Advisor: Professor Bingcai Pan

Dissertation title: “Mechanical Properties of Polymer-supported Hydrated Ferric Oxide (HFO) Nanocomposites: Effect of HFO Loadings”

### Professional Experience

- Graduate Research Assistant, Department of Environmental Health and Engineering, Johns Hopkins University, August 2013–present
- Graduate Teaching Assistant, Department of Environmental Health and Engineering, 2015 Fall Semester (570.301 Environmental Engineering Fundamental class, *taught two lectures on Reactor Design, with 21 students*)
- Graduate Teaching Assistant, Department of Environmental Health and Engineering, Johns Hopkins University, 2014 Spring Semester (570.304 Undergraduate *Environmental Engineering Laboratory class with 20 students*)
- Graduate Research Assistant, Department of Environmental Engineering, Nanjing University, August 2010–June 2013

### Honors and Awards

- ACS C. Ellen Gontter Environmental Chemistry Award, 2017

- Johns Hopkins Graduate Representatives Organization (GRO) Travel Grant, 2016
- Outstanding Student Presentation Award in the ACS Division of Environmental Chemistry Symposium on Environmental Transformation of Nanoparticles, August 21, 2015, Boston, Massachusetts
- ACS Graduate Student Award in Environmental Chemistry, 2015
- Sustainable Nanotechnology Organization Student Award, Boston, 2014
- Outstanding Graduates of Nanjing University, Nanjing University, 2010
- Outstanding Leaders of School Student Union, Nanjing University, 2008
- People's Scholarship for Outstanding Students, Nanjing University, 2007–2009

## Journal Publications

1. Feng, Y. P.; **Liu, X. T.**; Huynh, K. A.; McCaffery, J. M.; Mao, L.; Gao, S. X.; Chen, K. L., Heteroaggregation of Graphene Oxide with Nanometer- and Micrometer-Sized Hematite Colloids: Influence on Nanohybrid Aggregation and Microparticle Sedimentation. *Environmental Science and Technology*, 2017, In Press (**Co-first author**)
2. Wang, Q. Y.; Lim, M.; **Liu, X. T.**; Wang, Z. W.; Chen, K. L., Influence of Solution Chemistry and Soft Protein Coronas on the Interactions of Silver Nanoparticles with Model Biological Membranes, *Environmental Science and Technology*, 2016, 50, 2301-2309.
3. **Liu, X. T.** and Chen, K. L., Aggregation and Interactions of Chemical Mechanical Planarization Nanoparticles with Model Biological Membranes: Role of Phosphate Adsorption, *Environmental Science: Nano*, 2016, 3, 146–156.
4. **Liu, X. T.** and Chen, K. L., Interactions of Graphene Oxide with Model Cell Membranes: Probing Nanoparticle Attachment and Lipid Bilayer Disruption, *Langmuir*, 2015, 31, 12076–12086.
5. Speed, D.; Westerhoff, P.; Sierra-Alvarez, R.; Draper, R.; Pantano, P.; Aravamudhan, S.; Chen, K. L.; Hristovski, K.; Herckes, P.; Bi, X. Y.; Yang, Y.; Zeng, C.; Otero-Gonzalez, L.; Mikoryak, C.; Wilson, B. A.; Kosaraju, K.; Tarannum, M.; Crawford, S.; Yi, P.; **Liu, X. T.**; Babu, S. V.; Moinpour, M.; Ranville, J.; Montano, M.; Corredor, C.; Posner, J.; Shadman, F., Physical, chemical, and in vitro toxicological characterization of nanoparticles in chemical mechanical planarization suspensions used in the semiconductor industry: towards environmental health and safety assessments. *Environmental Science: Nano*, 2015, 2, 227-244.
6. Wu, B. D.; Zhang, S. J.; Li, X. C.; **Liu, X. T.**; Pan, B. C., Iron in non-hydroxyl radical mediated photochemical processes for dye degradation: Catalyst or inhibitor? *Chemosphere*, 2015, 131,55-62.
7. **Liu, X. T.**; Song, X. J.; Zhang, S. J.; Wang, M. S.; Pan, B. C., Non-Hydroxyl Radical Mediated Photochemical Processes for Dye Degradation. *Physical Chemistry Chemical Physics*, 2014, 16, 7571-7577.
8. Zhang, S. J.; **Liu, X. T.**; Wang, M. S.; Wu, B. D.; Pan, B. C.; Yang, H.; Yu, H. Q., Diketone-Mediated Photochemical Processes for Target-Selective Degradation of Dye Pollutants. *Environmental Science and Technology Letters*, 2014, 1 (2), 167-171.
9. Zhang, S. J.; **Liu, X. T.**; Karanfil, T., Applicability of the Linear Solvation Energy Relationships in the Prediction for Adsorption of Aromatic Compounds on Activated Carbons from Aqueous Solutions. *Separation and Purification Technology*, 2013, 117, 111-117.
10. **Liu, X. T.**; Wang, M. S.; Zhang, S. J.; Pan, B. C., Application Potential of Carbon Nanotubes

- in Water Treatment: A review. *Journal of Environmental Sciences*, 2013, 25, (7), 1263-1280.
11. Zhang, S. J.; Peng, Y.; Jiang, W.; Liu, X. T.; Song, X. J.; Pan, B. C.; Yu, H. Q., Light-triggered Reversible Sorption of Azo Dyes on Titanium Xerogels with Photo-switchable Acetylacetonate Anchors. *Chemical Communications*, 2014, 50, 1086-1088.
  12. Wang, M. S.; Liu, X. T.; Pan, B. C.; Zhang, S. J., Photodegradation of Acid Orange 7 in a UV/acetylacetone Process. *Chemosphere* 2013, 93, (11), 2877-2882.
  13. Pan, B. C.; Xu, J. S.; Wu, B.; Li, Z. G.; Liu, X. T., Enhanced Removal of Fluoride by Polystyrene Anion Exchanger Supported Hydrous Zirconium Oxide Nanoparticles. *Environmental Science and Technology*, 2013, 47, (16), 9347-9354.

## Presentations

(Underlined names indicate presenting authors)

1. Liu, X., Livi, K., Chen, K. L. “Probing the Force Interactions between Silver Nanoparticles and Protein-modified Surfaces using Atomic Force Microscopy”, *American Chemical Society 252nd National Meeting*, Oral Presentation, August 21–25, 2016, Philadelphia, Pennsylvania.
2. Chen, K. L., Liu, X., Yan, C., “Interactions between graphene oxide and human serum albumin proteins: Implications for nanoparticle–membrane interactions”, *American Chemical Society 252nd National Meeting*, Oral Presentation, August 21–25, 2016, Philadelphia, Pennsylvania.
3. Yan, C., Liu, X., Chen, K. L., “Adsorption of human serum albumin proteins on graphene oxide”, *American Chemical Society 252nd National Meeting*, Oral Presentation, August 21–25, 2016, Philadelphia, Pennsylvania.
4. Yi, P., Gu, W., Liu, X., Chen, K. L., “Interactions of cerium oxide nanoparticles with model cell membranes: QCM-D measurements and theoretical analysis”, *American Chemical Society 252nd National Meeting*, Oral Presentation, August 21–25, 2016, Philadelphia, Pennsylvania.
5. Liu, X., Chen, K. L. “Aggregation and Interactions of Chemical Mechanical Planarization Nanoparticles with Model Biological Membranes”, *American Chemical Society 250<sup>th</sup> National Meeting*, Oral Presentation, August 16–20, 2015, Boston, Massachusetts.
6. Chen, K. L., Feng, Y., Liu, X. “Heteroaggregation of Graphene Oxide with Nanometer- and Micrometer-sized Hematite Colloids: Rates and Conformation”, *American Chemical Society 250<sup>th</sup> National Meeting*, Oral Presentation, August 16–20, 2015, Boston, Massachusetts.
7. Chen, K. L., Liu, X. “Interactions of Chemical Mechanical Planarization Nanoparticles with Model Biological Membranes”, *Gordon Research Conference, Environmental Nanotechnology*, Poster Presentation, June 21–26, 2015, West Dover, Vermont.
8. Liu, X., Chen, K. L. “Interaction of Chemical Mechanical Planarization Nanoparticles with Model Cell Membranes”, *Sustainable Nanotechnology Organization 3<sup>rd</sup> Conference*, Poster Presentation. November 2–4, 2014, Boston, Massachusetts.
9. Chen, K. L., Liu, X. “Interactions of Graphene Oxide with Model Cell Membranes”, *American Chemical Society 248<sup>th</sup> National Meeting*, Oral Presentation, August 10–14, 2014, San Francisco, California.
10. Liu, X.; Chen, K. L. “Probing the Interactions of Graphene Oxide Nanomaterials with Model Cell Membranes Using QCM-D”, *88<sup>th</sup> ACS Colloid and Surface Science Symposium*, Oral Presentation. June 22–25, 2014, Philadelphia, Pennsylvania.
11. Chen, K. L.; Liu, X. “Interaction of Graphene Oxide with Model Cell Membranes”, *Gordon Research Conference, Environmental Science: Water*, Poster Presentation. June 22–27, 2014,

Holderness, New Hampshire.

12. Chen, K. L.; Liu, X. “Interactions of Chemical Mechanical Planarization Nanoparticles with Model Cell Membranes: Implications for Nanoparticle Toxicity”, *SRC GRC Engineering Research Center for Environmentally Benign Semiconductor Manufacturing Annual Review Meeting*, Poster Presentation. March 26–27, 2014, Tucson, Arizona.

## Reviewer for Scholarly Journals

- Environmental Science and Technology
- Langmuir
- Soft Matter

## Students Mentored

- Chenxu Yan (MS student at Johns Hopkins University)
- Jeongjae Kim (Undergrad student at Johns Hopkins University)
- Jingsheng Xu (MS student at Nanjing University)

## Professional Affiliations

- American Chemical Society (ACS)
- Association of Environmental Engineering and Science Professors (AEESP)
- American Water Works Association (AWWA)